Multiplex Biomaterial Matrix Cues Regulate Redox Status and Stemness in  Human Mesenchymal Stem Cells

By

Spencer William Crowder


Dissertation

Submitted to the Faculty of the

Graduate School of Vanderbilt University

in partial fulfillment of the requirements

for the degree of


DOCTOR OF PHILOSOPHY

in


Biomedical Engineering


May, 2014


Nashville, Tennessee


Approved:

Hak-Joon Sung, Ph.D.

Craig L. Duvall, Ph.D.

David M. Bader, Ph.D.

Todd Giorgio, Ph.D.

Ann Richmond, Ph.D.

# ACKNOWLEDGEMENTS

TABLE OF CONTENTS

# LIST OF TABLES

# LIST OF FIGURES

# LIST OF ABBREVIATIONS

| | |
|---|---|
| ALCAM | Activated leukocyte cell adhesion molecule |
| Ang1 | Angiopoietin-1 |
| Ang2 | Angiopoietin-2 |
| BrdU | 5-bromo-2'-deoxyuridine |
| BSA | Bovine serum albumin |
| CDM | Chemically-defined media |
| cDNA | Complimentary DNA |
| CM-$H_2$DCFDA | 5-chloromethyl-2',7'-dichlorodihydrofluorescein diacetate |
| cPCL | Carboxylated-PCL |
| CSC | Cancer stem cell |
| DCFDA | Dichlorofluorescein diacetate |
| DCM | Dichloromethane |
| DHE | Dihydroethidium |
| DMA | Dynamic mechanical analysis |
| DSC | Differential scanning calorimetry |
| E | Young's modulus |
| EC | Endothelial cell |
| FBS | Fetal bovine serum |
| FCM | Flow cytometry |
| GAPDH | Glyceraldehyde 3-phosphate dehydrogenase |
| $H_2O_2$ | Hydrogen Peroxide |
| HIF | Hypoxia-inducible factor |
| hMSC | Human mesenchymal stem cell |
| HUVEC | Human umbilical vein endothelial cell |

| | |
|---|---|
| ID1 | DNA-binding protein inhibitor 1 |
| ID2 | DNA-binding protein inhibitor 2 |
| ITGA2 | Integrin $\alpha_2$ |
| ITGA6 | Integrin $\alpha_6$ |
| ITGB1 | Integrin $\beta_1$ |
| LC-MS/MS | Liquid chromatography-mass spectrometry/mass spectrometry |
| LDA | Lithium diisopropylamide |
| MMP | Matrix metalloproteinase |
| mRNA | Messenger RNA |
| NG2 | Neuron-glial antigen 2 |
| Ni | Nickel |
| NiSO$_4$ | Nickel sulfate |
| NMR | Nuclear magnetic resonance |
| $O_2^{\cdot-}$ | Superoxide |
| OCT | Optical coherence tomography |
| PAI1 | Plasminogen activator inhibitor-1 |
| PBS | Phosphate buffered saline |
| PCL | Poly($\varepsilon$-caprolactone) |
| PDGFR$\beta$ | Platelet-derived growth factor-$\beta$ |
| PECAM | Platelet-endothelial cell adhesion molecule |
| PEG | Poly(ethylene glycol) |
| PFA | Paraformaldehyde |
| PLGA | Poly(lactic-co-glycolic acid) |
| PLLA | Poly(L-lactic acid) |
| QCM-D | Quartz crystal microbalance with dissipation |
| Ra | Average deviation from the arithmetic mean |

| | |
|---|---|
| ROS | Reactive oxygen species |
| RT-PCR | Real-time polymerase chain reaction |
| SEM | Scanning electron microscope |
| TCPS | Tissue culture polystyrene |
| $T_g$ | Glass transition temperature |
| TGA | Thermogravimetric analysis |
| TGF-β | Transforming growth factor-β |
| THF | Tetrahydrofuran |
| TI | Transformation induction |
| Tie1 | Tyrosine kinase with immunoglobulin-like and EGF-like domains 1 |
| Tie2 | TEK tyrosine kinase |
| $T_m$ | Melting temperature |
| VEGF | Vascular endothelial growth factor |
| vWF | von Willebrand factor |
| αMEM | Alpha minimum essential medium |
| αSMA | Alpha smooth muscle actin |
| ΔH | Change in enthalpy |
| $\sigma_u$ | Ultimate tensile strength |

CHAPTER 1

Introduction and Motivation

Human bone marrow-derived mesenchymal stem cells (**hMSCs**) are a promising cell source for regenerative medicine due to their autologous availability, immunomodulatory effects, self-renewal capacity, and multi-lineage differentiation potential[1]. hMSCs classically demonstrate osteogenic, chondrogenic, and adipogenic differentiation capacity[1], and have been used extensively in the field of tissue engineering for regenerating lost or damaged tissue. Furthermore, hMSCs are currently undergoing a number of clinical trials in the United States to evaluate their therapeutic efficacy for a range of applications[2], including attenuation of graft-versus-host disease[3], Crohn's disease, repair of cardiac tissue following heart attack[4], and protection of tissue in type 1 diabetics or patients with chronic obstructive pulmonary disease (many of these are from Osiris Therapeutics, Inc.). However, the number of hMSCs available in the bone marrow is staggeringly low (~0.1%), indicating a requirement for *ex vivo* expansion in order to achieve a relevant number of cells for clinical applications[5]. Unfortunately, when expanded *in vitro*, hMSCs acquire senescence-associated abnormalities, including alterations in morphology, differentiation potential, gene and protein expression patterns, and arrested proliferation[5-8], all of which severely limit their therapeutic efficacy. Specifically, cell cycle regulation and DNA damage repair are significantly impaired with increasing passage (**Figure 1.1**). Furthermore, accumulation of superoxide
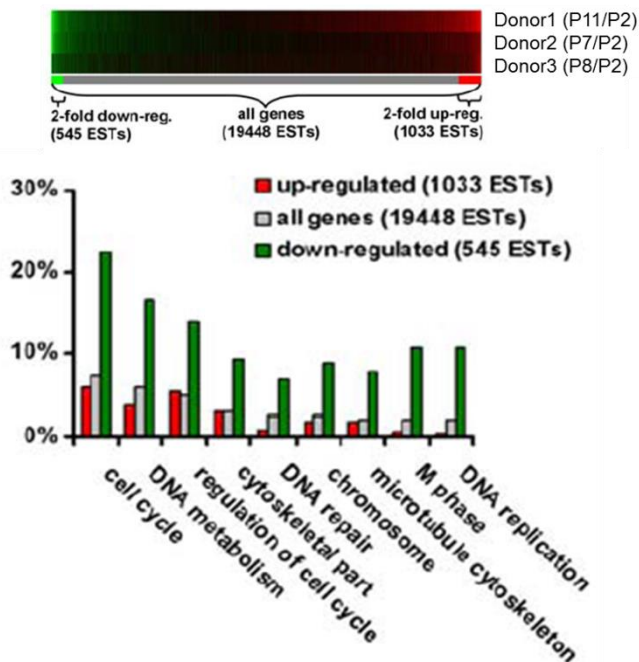


**Figure 1.1:** Serial *in vitro* passaging of hMSCs leads to drastic changes in gene expression profiles. hMSCs from three different donors were expanded *ex vivo* and microarray data were compared against their early passage counterparts. Interestingly, three of the classes of genes that were significantly downregulated are also involved in the onset and progression of cancer, such as cell cycle, regulation of cell cycle, and DNA repair. Adapted from W. Wagner *et al. PLoS ONE* **3**(5) 2008.

1

($O_2^{\cdot-}$), a short-lived type of reactive oxygen species (**ROS**), is a hallmark of hMSC senescence due in part to downregulated redox mechanisms[6, 9]. In parallel, the number of viable hMSCs in the bone marrow, as well as their differentiation capacity, decline with increasing donor age, while oxidative damage and ROS tend to accumulate[10]. Because many of the characteristics of *in vitro* senescence are also observed in hMSCs isolated from aging patients, it is possible that *in vivo* aging and *in vitro* cell senescence share inherent similarities[10, 11], and that *in vitro* studies that aim to approximate the *in vivo* status of hMSC regenerative potential and/or cancer susceptibility can be best recapitulated with higher passage hMSCs.

*The Role of hMSCs in Cancer*

In spite of extensive clinical results supporting their safety and efficacy for therapeutic purposes[12], hMSCs are known to play a causative role in cancer by both promoting and inhibiting tumor growth and metastasis, depending upon factors that remain undefined[13, 14]. Although studies of
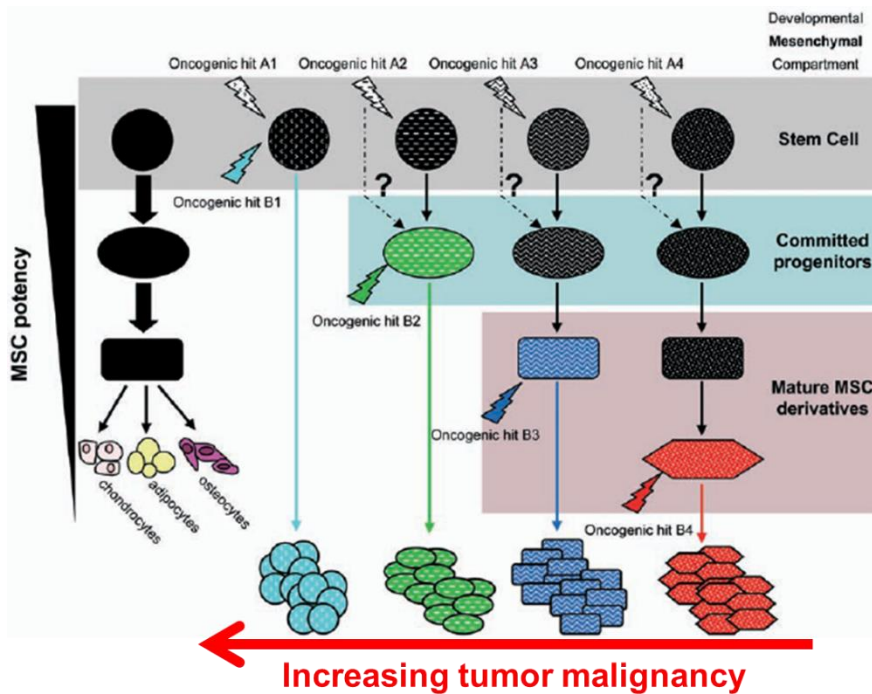


**Figure 1.2:** The degree of malignancy of a sarcoma is directly proportional to the stage in the mesenchymal development program at which the cell of origin was transformed. Tumors with the highest degree of malignancy arise from the transformation of naïve hMSCs, whereas more benign tumors arise from terminally differentiated cells. Adapted from R. Rodriguez *et al. Cell Res* 2011.

spontaneous hMSC transformation in culture have been refuted[15-17], hMSCs have been implicated as the tumor-initiating cell-of-origin in certain types of sarcomas and may represent the elusive cancer stem cell (CSC) in these diseases[18]. Interestingly, sarcomas of increasing malignancy are thought to be derived from earlier progenitor cells that display less lineage commitment, indicating that "naïve" hMSCs are responsible for the formation of tumors with the highest degree of malignancy (**Figure 1.2**)[18]. Malignant transformation of hMSCs has been induced by oncogenic insults, such as retroviral transfection with human oncogenes, resulting in *in vivo* tumor formation[19-21]. However, this transfection approach is non-

physiological and complicates a clear interpretation of how these events affect the contribution of hMSCs to tumor formation under physiological conditions. It is therefore of great importance to develop a physiologically-relevant *in vitro* model of cancerous transformation that can be used to elucidate the mechanisms that differentially regulate pathological changes in hMSCs, and to identify alterations in hMSC behavior that lead to enhanced susceptibility to transformation.

*Biomaterial Matrix Cues Governing Stem Cell Fate*

Synthetic biomaterial matrices have been designed and employed to guide the fate of stem cells for both basic science and clinically-translatable purposes[22, 23]. Biomaterial-based strategies for modulating cell behavior have investigated several extracellular cues, such as matrix stiffness[24], spacing and density of extracellular adhesion proteins[25], surface chemistry[26, 27], electrical conductivity (SW Crowder *et al*[28])[29, 30], three-dimensional biomimetic scaffolding[31, 32], and nanotopography[33]. Intrinsic biomaterial intrinsic properties can be generally classified as physical (i.e. stiffness), chemical (i.e. surface energy), and topographical (i.e. surface pattern and roughness), each of which can fundamentally alter the behavior of cells cultured upon/within the scaffold. These properties tend to be "coupled" together, where changing one material property immediately and directly affects another, related property.
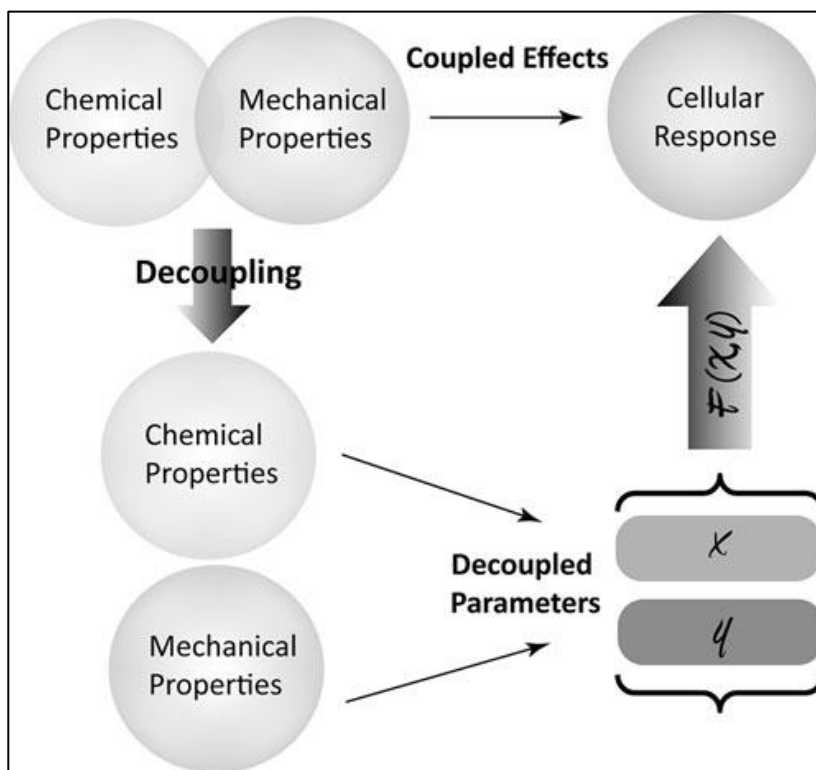


**Figure 1.3:** Coupling and decoupling of polymer chemical and mechanical properties determines the cellular response. Adapted from X. Wang *et al*. *Tissue Eng B* (2012).

"De-coupling" of material properties in order to understand the effect of each individual parameter on the resulting cell behavior remains a critical challenge in the field of biomaterials, and was the topic of a recent review paper from the Sung laboratory[34]. For example, the chemical composition of a polymer largely determines the other resulting material characteristics, including crystallinity, hydrophilicity/hydrophobicity and degradation. Improved crystallinity inherently correlates with enhanced polymer chain packing, thereby resisting water penetration and hydrolytic degradation. Also, tightly packed polymer chains usually result in increased material stiffness. These facts indicate that the resulting cellular behavior is actually in response to the coupled material properties rather than individual ones. Therefore, there is an unmet need to decouple the material properties so that the effect of individual material properties on cellular functions can be clearly understood and exploited for enhanced, precise regulation of cell behavior (**Figure 1.3**).

*Combinatorial Polymers for Decoupling Physicochemical Biomaterial Properties (adapted from Wang et al. 2012[34])*

Altering the polymer composition is considered to be an important strategy to modulate matrix stiffness. However, a significant challenge still remains as changing the polymer composition often results in simultaneous changes to hydrophobicity, crystallinity and water uptake. For example, varying the blending ratio of poly(lactic-co-glycolic acid) (PLGA) and poly(L-lactic acid) (PLLA) created a mechanical gradient to determine a "threshold stiffness" for optimal cell organization, myotubule formation, and myoblast differentiation[35]. The two polymers, however, have inherently different chemical properties which change simultaneously with the blending ratio, indicating coupling between chemical and mechanical properties. Similarly, PCL was blended with poly(ether sulfone) (PES) to study the influence of polymer stiffness on the differentiation of embryonic mesenchymal progenitor cells. Stiffer PES-PCL scaffold (modulus = 30.6 MPa) promoted osteogenesis, while the softer, pure PCL scaffold (modulus = 7.1 MPa) promoted chondrogenesis[36]. However, the change in chemical composition via altering the blending ratio was coupled with stiffness and should also be considered.

Although copolymerizing and blending different monomers or polymers often lead to simultaneous change in other properties, these techniques can be used to decouple the chemical and mechanical properties by creating a combinatorial library of polymers and selecting compositions that display similar mechanical properties. Our recent study demonstrated that the wet elastic moduli of polymeric nanofibrous scaffolds were maintained within a tight range while altering the chemical compositions of co- or ter-polymers through combinatorial synthesis and electrospinning techniques[37]. This unique approach enabled the synthesis of six polymer formulations with unique chemical characteristics but similar wet moduli. When cultured with murine embryonic stem cell, they induced

different levels of expression of intracellular hydrogen peroxide and cardiomyocyte markers, suggesting the effect of polymer composition on cell behavior since the mechanical strength was maintained constant and decoupled. Additionally, the copolymerization of PCL with other polyesters, such as polyglycolic acid (PGA) and polylactic acid (PLA), have been shown to alter degradation, hydrophobicity, and crystallinity, while maintaining the elasticity exhibited by the pure PCL scaffold[38-41]. These examples demonstrate that the combinatorial synthesis of polymers is a promising approach for decoupling scaffold properties. The scale of combinatorial library can be expanded to further tune a particular type of material property while minimizing changes of other properties. A library of combinatorial polymers with 112 different compositions was produced from copolymerizing 14 different tyrosine-derived diphenols and eight aliphatic diacid monomers[42]. Changes in their chemical compositions were found to affect modulus, glass transition temperature ($T_g$) and contact angle. Polymers with similar property (e.g., stiffness or $T_g$) could be grouped to study the cell response affected by chemical composition, demonstrating effective decoupling of these properties[42]. Similarly, a library of poly(β-amino esters) (PBAEs) provided tunable mechanical, degradation, and adhesion properties. Degradation and mechanical properties were decoupled by varying Mw and branching structure[43, 44]. Selected PBAE macromers were also cross-linked during electrospinning to improve the tunability of mechanical and degradation properties [45]. Such an approach was used to elucidate polymer structure-function relationships, thereby improving the safety and efficacy of their applications for gene delivery [46, 47]. Similar approaches have been adapted to fine-tune cellular responses to PCL acrylates [48] and methacrylate terpolymers[49]. An excellent review of combinatorial polymer synthesis techniques, high-throughput assessment of material properties and material-cell interactions are thoroughly covered elsewhere[50].

These combinatorial synthesis techniques offer distinct advantages over traditional synthesis used for "one-measurement for one-sample" in terms of time, resources, and information to be obtained. However, there are still drawbacks and challenges associated with these methodologies, including preservation of sample purity, data handling, and availability of such resources[51]. It is more challenging to use high-throughput schemes for sophisticated syntheses that require purification, and in many cases it is more worthwhile to test discrete polymer ratios to obtain data by a potentially more reliable method. Polymer blends can be used to circumvent such issues with synthesis, for instance, by observing cellular responses to gradient changes of polymer properties in a two-dimensional combinatorial library (e.g. temperature and polymer composition). For example, Sung *et al.* reported that a large library of PCL/PLGA blends with different stiffness, surface roughness and/or crystallinity have been generated by varying PCL to PLGA ratio and the annealing temperature, which provides an applicable approach for decoupling by selecting a group of blends similarly in one property (e.g., stiffness) while differing in another (e.g., chemical composition). This study further demonstrated that a mid-to-high relative

composition of PCL in a PCL/PLGA blend was ideal for smooth muscle cell adhesion, proliferation, and protein production[52]. Similarly, biomaterial microarrays can be used to decouple stiffness, cross-linking density, and crystallinity[53] and examine other chemical and topographical influences on various cell functions[54-57]. These combinatorial approaches offer much promise in elucidating the distinct mechanisms that govern cell-material interaction to further advance biomaterials and tissue engineering technologies.

*Objectives and Specific Aims*

The behavior of hMSCs to changing material properties has been evaluated in a number of engineering systems, but investigations of late passage, serially-expanded hMSCs as a model for *in vivo* aging has been overlooked. Furthermore, the majority of studies have focused on directed differentiation, guiding hMSCs toward specific lineage commitments, as opposed to the maintenance of an undifferentiated phenotype, which would be most relevant for clinical applications. The mechanisms and biological relevance of hMSC differentiation have been clearly described, but the cascade of events that *prevent* lineage specification remain unknown. Through the work described in this dissertation project, the following Specific Aims will be addressed:

*Specific Aim #1:* To determine the passage-dependent susceptibility of hMSCs to a harsh environment of carcinogenic hypoxia as an *in vitro* model for early cancerous transformation events.

*Specific Aim #2*: To synthesize a new class of copolymer substrates, thoroughly characterize the physicochemical and surface properties, and apply these materials as synthetic culture substrates for late passage hMSCs in order to evaluate the extracellular matrix-mediated regulation of redox and stemness.

*Specific Aim #3*: To systematically identify the biological relevance of hMSCs cultured with increased expression of "stemness" genes *in vitro* and *in vivo*, and to determine the structure-function relationship at the cell-biomaterial interface that is driving the observed event.

In each Aim, additional background information is provided that will guide the reader through the relevant points of each topic. At the end of this dissertation, a summary of the findings and a description of the ongoing work are provided, concluding the story presented here and illustrating the impact and novelty of the project.

CHAPTER 2


Specific Aim #1: hMSC passage-dependent response to carcinogenic hypoxia.


The following Chapter is adapted from **SW Crowder** *et al. FASEB J* (2013)[58].


**Introduction**


Hypoxia is a fundamental microenvironmental cue in both the healthy hMSC niche and malignant tumors.  The bone marrow niche where hMSCs reside experiences hypoxic conditions of 1-7% $O_2$[59] whereas tumor hypoxia can be more extreme (less than 1% $O_2$), including micro-regions of anoxia[60]. When cultured under hypoxic conditions, hMSCs exhibit increased proliferation[61], expression of prosurvival and proangiogenic factors[62], and maintenance of an undifferentiated state that bypasses replicative senescence[63-65].  The expression of hypoxia-related genes is controlled by hypoxia inducible factor 1 (**HIF1**), a transcription factor implicated in several cancers and whose activities include regulation of angiogenesis, cell survival, and apoptosis[66].  The activities of the tumor suppressor protein p53, whose role in the DNA damage response and apoptosis is dysregulated in virtually all human cancers[67], are directly attenuated by HIF1[68, 69].  The metal carcinogen nickel (**Ni**) also stimulates accumulation of HIF1, further reducing the expression of p53-regulated genes[70-72].  In the United States, the average person consumes roughly 150 μg of Ni per day through food, water, and inhalation[73], illustrating the relevance to study Ni as a prevalent environmental carcinogen.  A common oncogenic transcription factor, c-myc, regulates proliferation-associated genes[74] and accumulates in immortalized, Ni-treated human cells[75], but the role of c-myc in response to Ni has not been investigated in primary or pre-neoplastic cells.  Because Ni is highly prevalent and has been shown to effectively transform human cells, studying its effects on hMSC transformation in the presence of hypoxia provides a novel and physiologically-relevant paradigm for how an environmental carcinogen dysregulates stem cell functions. Therefore, in Specific Aim #1, an environmentally-relevant model of carcinogenic hypoxia has been developed, and the passage-dependent sensitivity of declining redox mechanisms has been determined in terms of early transformation events.

**Materials and Methods**

*Cell Culture*

hMSCs (Lonza, Walkersville, MD) were maintained in α Modified Eagle's Medium (αMEM, Gibco Cell Culture, Carlsbad, CA, USA) with 20% fetal bovine serum (FBS, Gibco) with 1% penicillin-streptomycin (P/S, Gibco) at 37°C and 5% $CO_2$. For all experiments, cells were seeded at a density of 5,000 cells / $cm^2$. Treatment conditions included sterile-filtered nickel sulfate (100 μM, Sigma Aldrich, St. Louis, MO, USA) and/or hypoxia (0.5% $O_2$, 5% $CO_2$, 94.5% $N_2$) in a hypoxia incubator chamber (STEMCELL Technologies, Vancouver, B.C., Canada). Cells were cultured for three days before endpoint evaluations. The two passage groups, passage 7-9 (P7-9) and passage 12+ (P12+), were selected to represent "early" and "advanced" stages of abnormality acquisition and senescence, respectively[9].

*Western Blot*

Western blot analysis was done according to standard protocols[76]. Primary antibodies (1:1000) include: mouse anti-human p53 (recognizes both mutant and wild-type forms of p53, Abcam, Cambridge, MA, USA), mouse anti-human HIF1A (Abcam), rabbit anti-human c-MYC (generously provided by Dr. Steve Hann, Vanderbilt University Medical Center), and mouse anti-human β-actin (Santa Cruz Biotechnology, Santa Cruz, CA, USA). Horseradish peroxidase (HRP)-conjugated secondary antibodies (1:1000, Santa Cruz Biotechnology) were used; relative protein expression against β-actin was quantified via densitometric analysis using ImageJ software (NIH, Bethesda, MD, USA) (n ≥ 3 independent experiments).

*Cell Proliferation*

Cells were incubated with 5-bromo-2'-deoxyuridine (BrdU, Sigma) at 20 μM for 16 hours, fixed in 4% paraformaldehyde (PFA, Sigma), and blocked with 1% bovine serum albumin (BSA, Sigma). DNA was denatured with HCl (2N for 12 minutes on ice, 1N for 20 minutes at 37°C) and neutralized with borate buffer (pH 9.0). Incorporated BrdU in proliferating cells was detected by rat anti-BrdU antibody overnight at 4°C (1:100, Abcam), followed by secondary DyLight594-conjugated goat anti-rat antibody for 2 hrs at room temperature in the dark (1:50, Jackson Immunoresearch, West Grove, PA, USA). Nuclei were counterstained with Hoechst (5 μg/mL, Sigma) and cells were imaged under a Nikon Eclipse Ti inverted fluorescence microscope (Nikon Instruments Inc, Melville, NY, USA). Cell proliferation was represented by the percent of BrdU-positive cells relative to the total number of cells per image (n ≥ 6 images).

*ROS Activities*

To measure intracellular hydrogen peroxide ($H_2O_2$) or $O_2^{\cdot-}$, hMSCs were incubated with dichlorofluorescein diacetate (DCFDA, Molecular Probes, Carlsbad, CA, USA) or dihydroethidium (DHE, Molecular Probes), respectively, for 30 minutes at 5 µg/mL at 37°C. Cell nuclei were counterstained with Hoechst. Fluorescence intensity was measured on a plate reader (Tecan Group Ltd., Männedorf, Switzerland) and normalized to the corresponding cell number (excitation/emission: DCFDA 490/540nm, DHE 340/535nm, Hoechst 360/488nm). To visualize and quantify mitochondrial superoxide (mROS), cells were incubated with MitoTracker Red (CM-$H_2$XROS, Invitrogen) for 30 min at 2.5 µg/mL. The average fluorescence intensity for individual cells was calculated using ImageJ. Reduction potential was quantified by measuring the reduction of the resazurin sodium salt (Sigma) to resofurin, following the manufacturer's instructions. Cells were incubated with resazurin at 5µM for 2 hours at 37°C. Reduction activity was measured on a plate reader (Tecan, 535/595nm excitation/emission) and normalized to cell number. For all experiments, n ≥ 3 replicates.

*Caspase-3 Activity*

Caspase-3 activity was quantified with a colorimetric assay kit (BioVision, Mountain View, CA, USA) according to the manufacturer's protocol. Experiments were conducted in triplicate and the average normalized optical density was reported.

*β-galactosidase Staining*

Staining was performed with the senescence β-galactosidase staining kit from Cell Signaling Inc. (Danvers, MA, USA) according to the manufacturer's protocol.

*Flow Cytometry*

Cells were fixed with 4% PFA, blocked with 1% BSA, and incubated with fluorophore-conjugated primary antibodies in 1%BSA for 2 hrs (1:10, eBiosciences, San Diego, CA, USA). Antibodies included FITC-conjugated CD90 and PE-conjugated CD105. Tests were performed using a FACScalibur flow cytometer (Becton Dickson, Franklin Lakes, NJ, USA) with an unstained hMSC population containing both passage groups as a control. Data were analyzed with FlowJo (Tree Star, Ashland, OR, USA) and reported percentages were calculated by gating the desired cell population on the forward/side scatter plot and setting a fluorescence exclusion for >99% of the control population.

*Reverse transcriptase polymerase chain reaction (RT-PCR)*

RNA was harvested with QIAshredder (Qiagen, Valencia, CA, USA) and RNeasy column (Qiagen) following the manufacturer's protocol. cDNA was synthesized with the iScript cDNA synthesis kit (Bio-Rad, Hercules, CA, USA) and RT-PCR was performed using the iQ SYBR Green supermix (Bio-

Rad) on a Bio-Rad CFX Real Time Instrument for: glyceraldehyde 3-phosphate dehydrogenase (*GAPDH*), vascular endothelial growth factor (*VEGF*), *HIF1A*, *c-MYC*, matrix metalloproteinase-2 (*MMP-2*), membrane type I MMP (*MMP-14*), and tissue inhibitor of metalloproteinase-2 (*TIMP-2*). β-actin was used as a reference gene. MMP sequences were obtained from a previous study[77]. Primer sequences were used as follows: *GAPDH*: 5'-GCCTCAAGATCATCAGCAATG-3' (sense) and 5' CTTCCACGATACCAAAGTTGTC-3' (anti-sense), *VEGF*: 5'- CAGAAGGAGGAGGGCAGAATC-3' (sense) and 5'- CACACAGGATGGCTTGAAGATG-3' (anti-sense), *p53* 5'-GCGTGTGGAGTATTTGGATGAC -3' (sense) and 5'- AGTGTGATGATGGTGAGGATGG -3' (anti-sense), *c-MYC*: 5'-CGTCCTCGGATTCTCTGCTCTC-3' (sense) and 5'-CCTCATCTTCTTGTTCCTCCTCAG-3' (anti-sense), *HIF1A*: 5'-TACCCTAACTAGCCGAGGAAGAAC-3' (sense) and 5'- ATCAGCACCAAGCAGGTCATAG-3' (anti-sense), β-actin: 5'-ATCATGTTTGAGACCTTCAA-3' (sense) and 5'-CATCTCTTGCTCGAAGTCCA-3' (anti-sense). Data were analyzed with CFX Manager software (Bio-Rad) and results are presented as ΔΔC(t) expression normalized to β-actin.

*Osteogenic and Adipogenic Induction*

Osteogenic and adipogenic induction media were purchased from Lonza. For adipogenesis, hMSCs were cycled between adipogenic induction and maintenance media ± the NADPH oxidase inhibitor, diphenyleneiodinium chloride (DPI, 4 μM, Sigma) for a total of 15 days (3 days induction, 1 day maintenance, 3 days induction ± DPI, 3 days maintenance, 3 days induction ± DPI, and 2 days maintenance). Osteogenic induction media was changed every 3-4 days for a total of 15 days, during which time DPI treatment occurred for a total of six days. To verify differentiation, alkaline phosphatase (ALP) activity and Nile red staining were performed for osteogenic and adipogenic differentiation, respectively. ALP activity was quantified using the p-nitrophenyl phosphate liquid substrate system according to the manufacturer's instructions (Sigma, n=3). For Nile red staining, cells were fixed with 4%PFA and incubated with 100 ng/ml Nile red in 150mM NaCl for 10 min. Cells were then washed, counterstained with Hoechst, and imaged using a Nikon Ti inverted microscope. The green fluorescence channel is shown due to improved specificity[78].

*SDS-PAGE Gelatin Zymography*

The proenzyme and active forms of MMP-2 and MMP-9 were detected using SDS-PAGE gelatin zymography in the presence of SDS in 10% polyacrylamide gels containing 0.1% (w/v) gelatin[79]. Media samples were collected from cells incubated in serum-free DMEM media 24 hours prior to collection. Total protein concentrations were determined by Bradford assay, and the samples were diluted 1:1 in sample buffer containing 0.14M Tris-HCl (pH6.8), 20% (v/v) glycerol, 4.5% (w/v) SDS, and 0.003%

Bromphenol blue. Twenty μg of protein was loaded into each well. Electrophoresis was performed in non-reducing conditions in a BioRad Mini Protean 3 system. Proteins were renatured by washing the gels in four 10-minute incubations in 2.5% Triton X-100. For gelatinolytic activity, the gels were incubated at 37°C for 18 hours in 50 mM Tris-HCl (pH 7.3, Sigma) containing 1.47g/L $CaCl_2$ (Sigma) and 0.05% Brij-35 (Fisher Scientific, Pittsburgh, PA, USA). The proteins were fixed for 2 hours with gentle agitation in 30% methanol and 10% acetic acid at room temperature, followed by staining for 18 hours with 0.1% (w/v) Brilliant Blue R-250, 0.64M ammonium sulfate (Sigma) and 25% methanol. The gels were destained in 25% methanol for 2 hours.

*In Vivo Experiments and Immunohistochemistry*

Animal housing and experimentation were performed according to the Vanderbilt Institutional Animal Care and Use Committee guidelines under an approved protocol. For experiments, $8x10^5$ hMSCs from each group were injected subcutaneously with 200μL Matrigel (BD Biosciences, San Jose, CA, USA) into the scapular region of athymic $Foxn1^{nu/nu}$ female mice (4-6 weeks of age, n = 3 mice / group, 12 mice total, Harlan Laboratories, Indianapolis, IN, USA) and allowed to grow for one month. Each week, animals were anesthetized with 2.5% isoflurane under steady flow, weighed, and tumor nodules were measured with electronic calipers. After one month, animals were sacrificed by cervical dislocation under anesthesia and tumor samples were placed in 4%PFA for 24 hours before being submitted for embedding, sectioning, and immunohistochemistry (IHC). All IHC was performed by the Translational Pathology Shared Resource Core at Vanderbilt University Medical Center. Slides were deparaffinized and antigen retrieval was performed using standard methods. Slides were stained for 30-60 minutes with primary antibodies against murine F4/80 (1:1000 dilution, Novus Biologicals, Littleton, CO, USA), Ki67 (1:100, Abcam), CD31 (1:100, Dianova, Hamburg, Germany), and human S100 (1:900, Dako, Carpinteria, CA, USA) followed by appropriate HRP-conjugated secondary antibodies and detection with 3,3'-diaminobenzidine (DAB) substrate according to standard protocols. IHC slides were imaged under a Nikon stereoscope.

*Statistical Analysis*

In all experiments, results are presented as mean ± standard error of the mean (SEM). Results from each experiment were initially analyzed using single factor analysis of variance (ANOVA) and comparisons between individual test groups were then performed using an unpaired Student's t-test. $p < 0.05$ was considered statistically significant.

## Results

*Passage-independent effects of Ni and hypoxia*

In order to establish which conditions best mimic a cancerous environment, the effects of hypoxia with or without $NiSO_4$ treatment were first investigated (**Figure 2.1**).  hMSCs of passage 5-15 were used
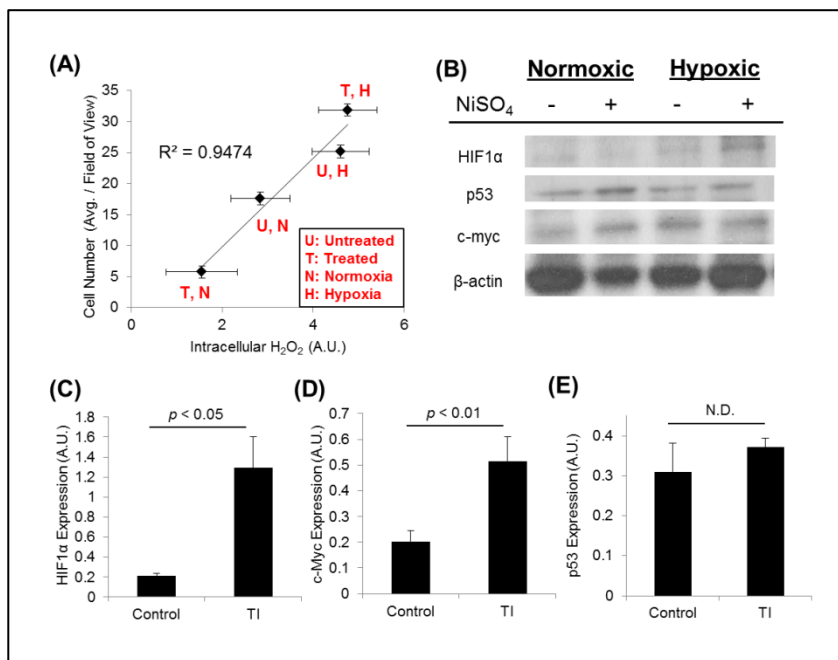


**Figure 2.1: Treatment with $NiSO_4$ under hypoxic conditions increases cell number and stimulates expression of cancer-related proteins in hMSCs. (A)** Cell number decreased with $NiSO_4$ treatment in normoxia (T,N) relative to untreated, normoxic control (U,N).  Under hypoxic conditions, cell number increased (U,H) and treatment with $NiSO_4$ further enhanced this effect, suggesting that the cytotoxic effects of Ni are more tolerated under hypoxia.  Interestingly, cell number was shown to correlate with intracellular $H_2O_2$ levels.  **(B)** Expression of the oncogenes HIF1α and c-myc, and the tumor suppressor protein p53, were altered upon treatment with $NiSO_4$ and/or hypoxia.  **(C-E)** hMSCs cultured under Ni-treated hypoxia (TI condition) exhibited a protein expression profile of that was similar to that classically seen in cancers (n ≥ 3 independent experiments).  N.D. – no statistical difference.

such that the effect of passage was not considered.  As seen in Figure 2A, $NiSO_4$ treatment in normoxia (**T, N**) reduced cell number compared to the untreated normoxia condition (**U, N**).  However, the untreated hypoxic condition (**U, H**) increased cell number versus normoxia alone, and $NiSO_4$ treatment in hypoxia (**T, H**) led to a further increase in cell number.  Interestingly, the cell number in each condition correlated linearly with intracellular $H_2O_2$ content ($R^2 = 0.9474$), suggesting a role of $H_2O_2$ in regulating cell proliferation.

Expression of cancer-related proteins was evaluated in each condition (**Figure 2.1B**).  In untreated normoxia, expression levels for HIF1α and c-myc were very low, and p53 expression was

moderate. Upon treatment with $NiSO_4$ in normoxia, the expression of c-myc and p53 increased as compared to untreated normoxia, and this correlated with a drastic reduction in cell number (**Figure 2.1A**), verifying that the interplay of p53 and c-myc regulates proliferation and apoptosis. In untreated hypoxia, HIF1α and c-myc expression were upregulated as compared to untreated normoxia, which correlated with increased cell number and supports the role of these transcription factors in accelerating proliferation. P53 expression did not appear to change between these two untreated conditions. Finally, $NiSO_4$ treatment in hypoxia stimulated a strong increase in HIF1α expression as compared to untreated hypoxia, indicating the synergistic role of nickel and hypoxia in accumulating HIF1α. Additionally, c-myc expression remained strong in this condition and p53 expression did not appear to change as compared to the untreated, normoxic condition. Taken together, the $NiSO_4$-treated hypoxia condition most closely resembled a classical cancer profile (i.e. strong expression of HIF1α and c-myc with moderate p53 activity). We therefore identified 100 μM $NiSO_4$ treatment under 0.5% $O_2$ hypoxia as the most effective condition for transformation induction (**TI**). Control was defined as the normoxic untreated condition (0 M $NiSO_4$, 21% $O_2$). As seen in Figure 5C-E, the relative expression levels of the three cancer-related proteins were more rigorously investigated between the control and TI conditions (n ≥ 3 independent experiments). In the TI condition, HIF1α and c-myc expression were significantly up-regulated while p53 expression did not statistically change (**Figure 2.1C-E**), validating that the hMSCs in the TI condition exhibit an expression profile that generally mimics that of cancer cells.

*ROS- and passage-dependent response to carcinogenic hypoxia*

The passage-dependent response of hMSCs to the TI condition was then characterized in terms of proliferation, apoptosis, Western blot, RT-PCR, and immunophenotype. The TI condition reduced proliferation of P7-9 hMSCs, but stimulated proliferation in P12+ cells as compared to their respective controls (**Figure 2.2A**). Furthermore, activity of the apoptosis-related protein, caspase-3, was increased in the TI condition for P7-9 cells but decreased significantly for P12+ hMSCs (**Figure 2.2B**).

The two passage groups also exhibited different expression patterns for cancer-related proteins (**Figure 2.2C**). In the control condition, basal expression for the oncogenes c-myc and HIF1α was higher for P12+ cells but expression of p53 was much lower, as compared to P7-9 hMSCs. Interestingly, P7-9 expression of c-myc was virtually non-existent in the control condition, but c-myc was expressed strongly in P12+ control cells. In the TI condition, expression of all three proteins increased for both passage groups, as compared to their respective controls.

The two passage groups also exhibited substantial differences at the level of gene expression (**Figure 2.2D-H**).  Expression of the glycolytic enzyme *GAPDH* increased significantly in the TI condition for both passage groups (**Figure 2.2D**), and these results agree with literature findings regarding an increased dependence upon glycolysis by hMSCs in hypoxia[65].  *C-myc* gene expression also increased significantly for both passage groups in the TI condition, but *p53* expression did not change (**Figure 2.2E-F**).  Interestingly, *p53* gene expression was higher for both conditions in P12+ cells, as compared to P7-9 cells, but p53 protein expression was actually lower for P12+ cells (**Figure 2.2C**), suggesting a drastic difference in post-transcriptional regulation between the two passage groups.  In the TI condition,
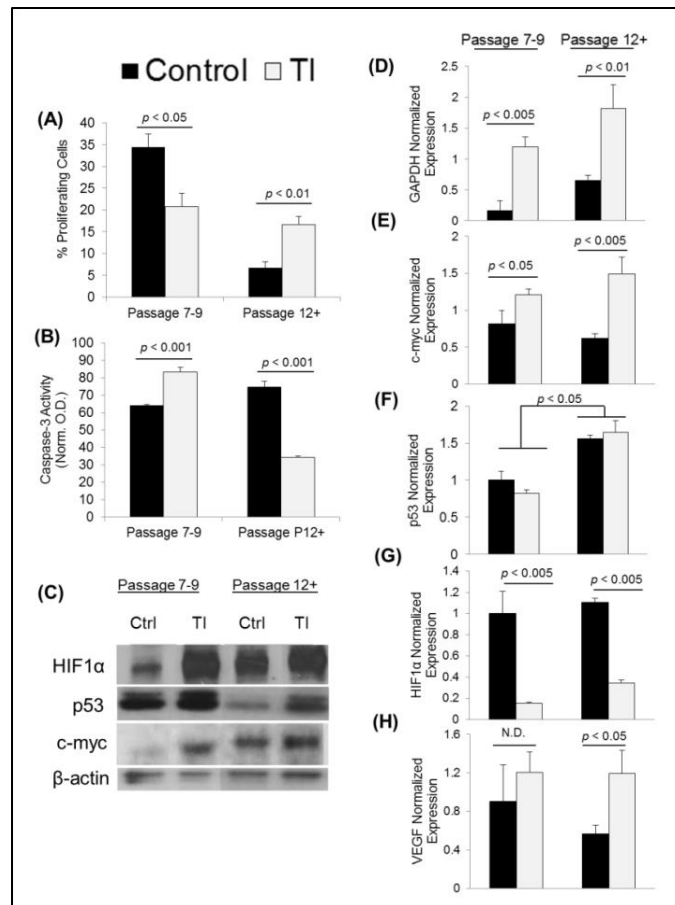


**Figure 2.2: hMSC response to the TI condition is passage-dependent.** (**A**) Proliferation decreased in P7-9 cells in the TI condition, but increased in P12+ cells.  (**B**) Apoptosis increased in P7-9 cells in the TI condition, but decreased in P12+ cells.  (**C**) Protein expression profiles for the two passage groups showed P12+ cells to exhibit strong basal expression of the oncogenes HIF1α and c-myc and weak expression of the tumor suppressor protein p53.  In the TI condition, expression of each of these proteins increased for both passage groups.  (**D-H**) Gene expression profiles for the two passage groups in control and TI conditions.  Genes of interest include (**D**) the glycolytic enzyme *GAPDH*, (**E**) *c-myc*, (**F**) *p53*, (**G**) *HIF1α*, and (**H**) *VEGF*.  Statistical significance is represented by lines connecting the conditions/groups that were compared.  N.D. – no statistical difference.

14

*HIF1α* gene expression decreased for both passage groups compared to control (**Figure 2.2G**). However, gene expression of the HIF1α-regulated *VEGF* did not change in the TI condition for P7-9 cells, but increased significantly for P12+ cells (**Figure 2.2H**), indicating that the hypoxia-responsive expression program was indeed activated.

We then sought to identify the status of replicative senescence in both passage groups as well as the role of the TI condition in modulating this behavior (**Figure 2.3A**). In the control condition, both passage groups stained positive for β-galactosidase expression (blue cells), indicating replicative senescence and supporting previous findings in the literature[9]. In the TI condition, hMSCs from both passage groups effectively left the senescent state, as indicated by a drastic reduction in the number of blue-stained cells.

The expression level of the positive hMSC markers CD90 and CD105 was then investigated by flow cytometric analysis (**Figure 2.3B-C**). Unstained cells are represented by the red, leftmost curve. Control hMSCs from both passage groups strongly expressed both markers (black outline, rightmost



|  | % Expressing Cells | | | |
|---|---|---|---|---|
|  | Passage 7-9 | | Passage 12+ | |
|  | Control | TI | Control | TI |
| CD 90 | 69.2 | 22.2 | 98.3 | 54.0 |
| CD 105 | 83.1 | 41.7 | 90.1 | 67.2 |
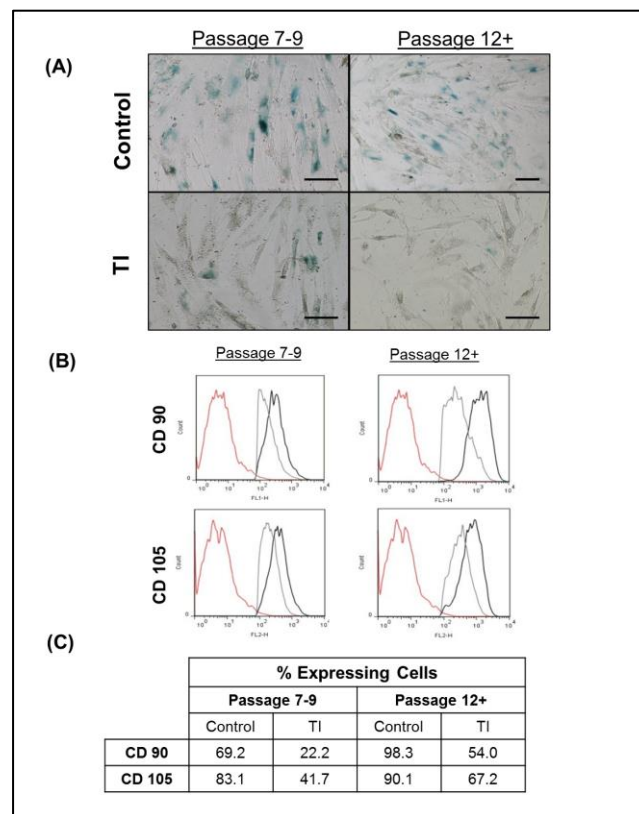
**Figure 2.3: The TI condition stimulates hMSC exit from replicative senescence and alterations in expression of stemness markers.** (**A**) hMSCs were observed to be in a state of replicative senescence in the control condition, but culture in the TI condition stimulated their exit from senescence. Scale bars = 100 μm. (**B**) Graphical representation immunophenotyping by flow cytometry (red outline - unstained control cells; black outline – control condition; grey outline – TI condition). (**C**) Quantification of flow cytometry data.

curve). Surprisingly, when quantified, P12+ cells showed stronger expression of these markers, indicating an effective maintenance of stemness into later passage (**Figure 2.3C**). In the TI condition, CD90 and CD105 expression decreased in both passage groups (grey outline, middle curve), but when quantified, P12+ cells were shown to retain their stemness to a higher degree than P7-9 cells. These data indicate that the TI condition stimulated differentiation, or significant downregulation, of hMSC-positive markers, in P7-9 cells that was not observed to the same degree in P12+ cells.

Because the two passage groups exhibited substantially different responses to the TI condition, and ROS are known to play crucial roles in both healthy tissue maintenance and cancer[80], the oxidative state of the two groups of cells was investigated (**Figure 2.4**). In the TI condition, intracellular $H_2O_2$ levels decreased for P7-9 cells but increased significantly in P12+ hMSCs (**Figure 2.4A**). In parallel, mROS were decreased in the TI condition in P7-9 cells but were unaltered in P12+ cells (**Figure 2.4B**),
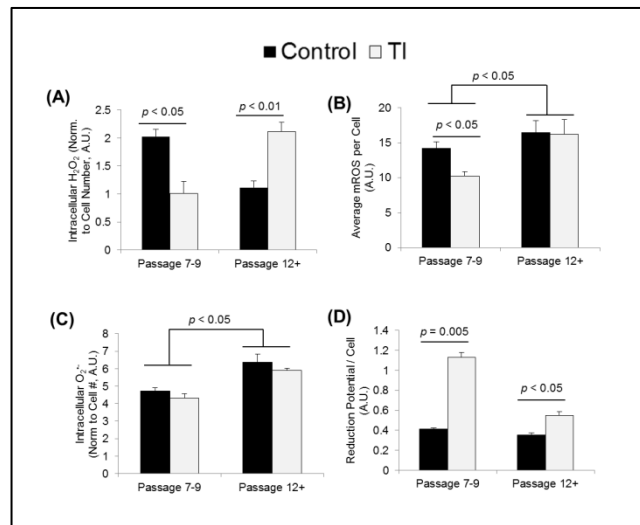


**Figure 2.4: Intracellular ROS levels, redox potential, and MMP activity are passage- and treatment-dependent.** (**A**) $H_2O_2$ levels decreased in the TI condition for P7-9 cells but increased for P12+ cells. (**B**) mROS and (**C**) $O_2^{\cdot-}$ levels were significantly higher P12+ cells versus P7-9. (**D**) Reduction potential was drastically lower for P12+ cells versus P7-9. (**E**) Zymography revealed little change in pro-MMP-9 expression in the three conditions, but expression of pro- and active-MMP-2 was altered in both a passage- and ROS-dependent manner. (**F-H**) Analysis of gene expression for MMP-2, -14, and TIMP-2 showed passage-dependent differences that provided insight for the discrepancies observed in zymography. * $p < 0.05$ and † $p < 0.01$ vs. respective control condition or between groups as indicated by lines. N.D. – no statistical difference.

and intracellular $O_2^{\cdot-}$ levels were significantly higher for all P12+ cells, as compared to all P7-9 cells (**Figure 2.4C**). These findings indicated that the reduction potential (i.e. anti-oxidative activities) of P12+ cells was dysregulated as compared to P7-9 cells. As seen in Figure 8D, P7-9 cells exhibited a significantly stronger reduction potential than did P12+ cells, suggesting that ROS-handling mechanisms

become disrupted in late passage hMSCs. Indeed, an accumulation of $O_2^{\cdot-}$ has been described in late passage hMSCs[6], and dysfunctional redox potential therefore follows as an explanation for increased susceptibility to the TI condition, which is not observed in lower passage, P7-9 cells.

*In vivo consequence following hMSC implantation*

When hMSCs were implanted *in vivo*, tumor-like nodules formed in all animals within one month (**Figure 2.6A**). Upon resection, nodules from the P7-9 control, P7-9 TI, and P12+ control groups were identical in gross morphology, exhibiting little to no vasculature and a homogeneous structure that resembled cartilaginous tissue. In contrast, nodules removed from all P12+ TI animals contained small, white structures embedded within the cartilaginous tissue, suggesting a stark difference in composition upon initial observation. Histological analyses, including H&E, Ki67, and F4/80, revealed specific differences between the groups (**Figure 2.5**). In all groups, H&E-stained sections of the subcutaneous implants revealed well-circumscribed nodules of mesenchyme with cartilaginous differentiation (**Figure 2.5, Row A**), which was confirmed by positive nuclear staining by S100 antibody (**Figure 2.6B**). Angiogenesis of the nodules was evaluated by a CD31 antibody. The nodules from all groups were virtually devoid of vessel lumen (**Figure 2.6, Row C**) despite single cells that stained positive for CD31. The subcutaneous nodules were surrounded by host soft tissues consisting predominately of fat and fibrous stroma with intermixing inflammatory cells. The cartilaginous nodules from groups P7-9 control, P7-9 TI, and P12+ control were all comparable with sparse to minimal cellularity and a low proliferative index as indicated by Ki-67 immunohistochemistry (5-10% nuclear staining; **Figure 2.5, Rows B,C**). The nodules from group P12+ TI were similar in overall appearance to the other groups, but displayed distinct differences. Specifically, the P12+ TI nodules had a significantly higher cellularity with a markedly increased proliferative index (20-50% nuclear staining by Ki-67), suggesting that this group most closely resembled the formation of a classical tumor.
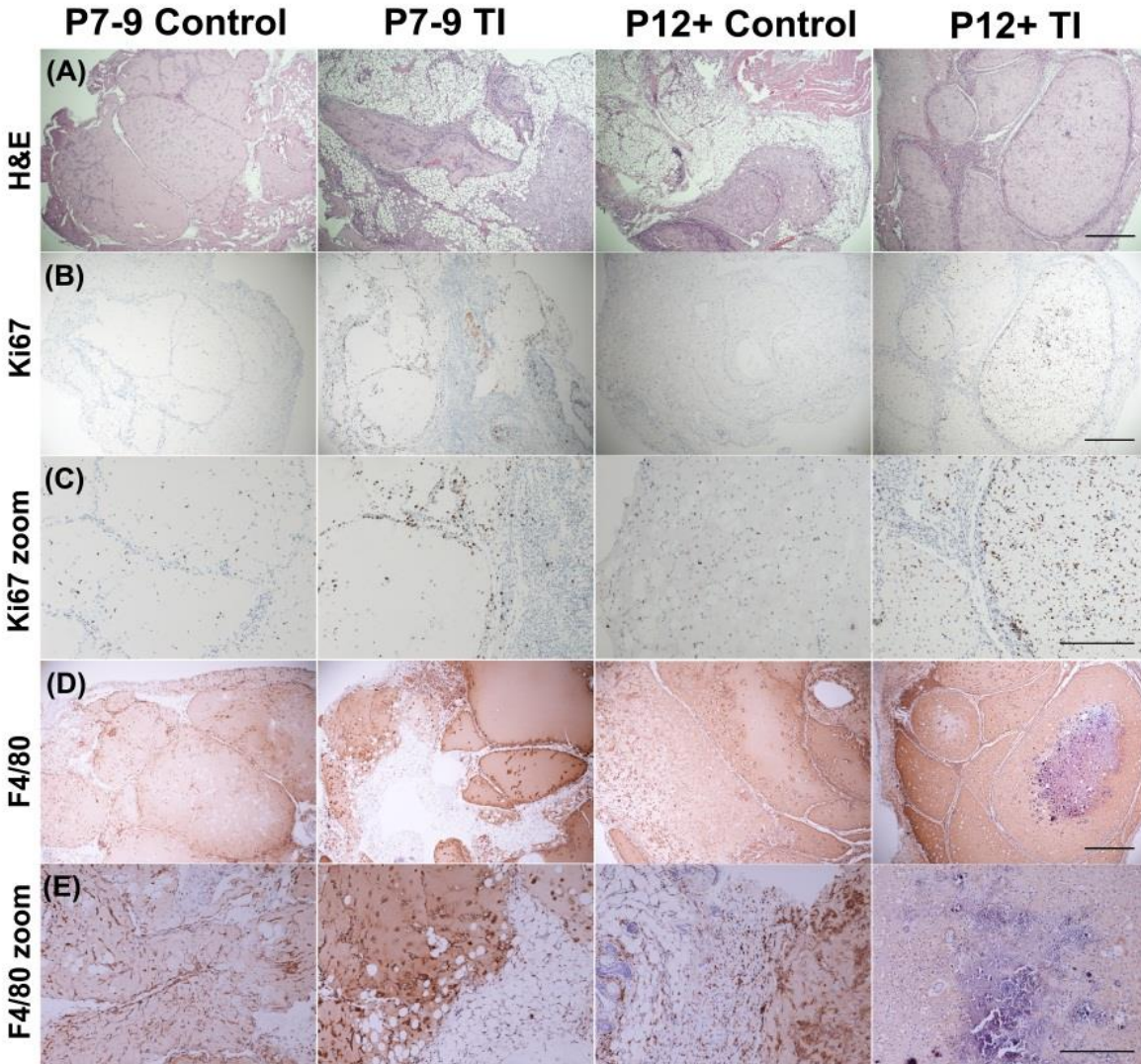
**Figure 2.5: Tissue samples from *in vivo* implantation experiments reveals significant differences between passage and treatment groups.** **(Row A)** Hematoxylin and eosin (H&E) staining showed that the tumor-like nodules from each group exhibited well-circumscribed mesenchyme with cartilaginous differentiation. In particular, tissues from the P7-9 control, P7-9 TI, and P12+ control groups contained high levels of adipose and stromal host tissue that surrounded the nodules whereas the P12+ TI group consisted primarily of distinct, hMSC-derived areas. **(Rows B,C)** The proliferative index of the two control groups was exceptionally low, exhibiting little to no positive staining for Ki67. In contrast, the two TI groups exhibited strong expression of Ki67; however, in the P7-9 TI group, this staining was isolated to the periphery of the nodules, including the host-derived stromal tissue, whereas the P12+ TI group demonstrated strong staining throughout the interior of the nodules. **(Rows D,E)** F4/80 staining for murine macrophages revealed that samples from the two control groups contained small macrophages that were evenly distributed throughout the nodules, but the two TI groups were arranged in clusters and displayed significantly more cytoplasm. Furthermore, the P12+ TI group displayed large areas within the nodule core that suggested early bone formation. Taken together, the P12+ TI group most closely represents the early stages of cancerous transformation. Scale bars: Rows A, B, and D = 500 μm; Rows C, and E = 250 μm.

The nodules from all groups were also evaluated for the presence of macrophages by F4/80 (**Figure 2.5, Rows D,E**). The macrophages in control groups were small and evenly distributed throughout both the nodules and surrounding stroma (**Figure 2.5, Row D**). In contrast, the macrophages in TI groups were decreased in number, predominately arranged in clusters within the nodules, and displayed significantly more cytoplasm (**Figure 2.5, Row E**). These data suggest that treatment under the TI condition stimulated an immunomodulatory effect beyond the intrinsic capability of hMSCs cultured under control conditions. Overall, P12+ TI hMSCs exhibited significantly increased cellularity, a higher proliferative index, and potential bone formation in the center of the nodules while minimizing macrophage infiltration, indicating that the *in vivo* result for this group could represent a neoplastic process that closely resembles that of a classical tumor, as compared with other groups.
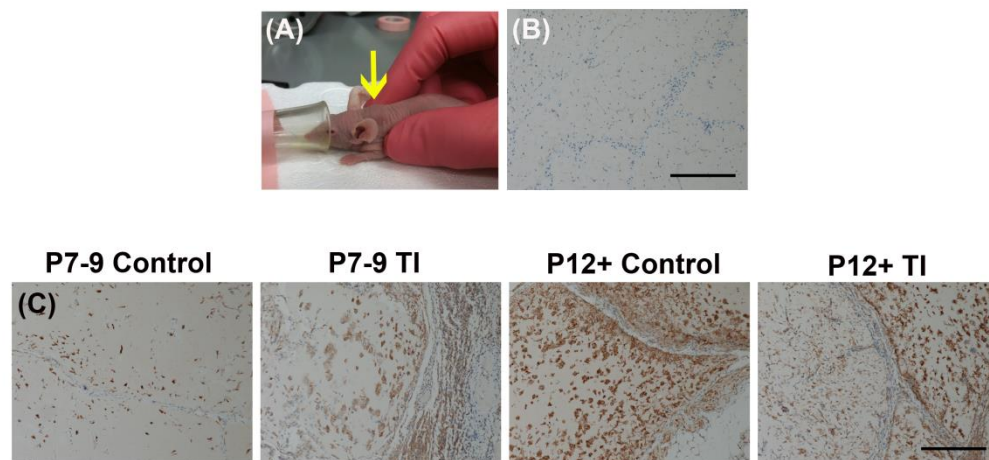


**Figure 2.6: *In vivo* implantation of hMSCs results in tumor-like nodule formation.** **(A)** Within one month, tumor-like nodules formed in all animals and **(B)** the tissue samples stained positive for S100, indicating cartilaginous differentiation. **(C)** Although single cells stained positive for CD31, vessel lumen formation was not observed, suggesting that the nodules were not vascularized. Scale bars = 250 μm.

**Discussion**

The behavior of MSCs changes with increasing passage and donor age in both humans[9, 10] and mice[81]. When expanded *in vitro*, hMSCs begin to acquire senescence-associated abnormalities between passages 7 and 12, including changes in gene and protein expression patterns, and arrested proliferation[9]. The present study sought to 1) develop and characterize a novel model for *in vitro* cancerous transformation, 2) profile the hMSC passage-dependent response to carcinogenic hypoxia, 3) observe the

differences in the *in vivo* consequence of the hMSC groups when implanted subcutaneously, and 4) identify a key mechanism governing this relationship.

We found that P12+ hMSCs represented a more transformation-susceptible population than P7-9, according to the data presented above. We have also identified a potential mechanism of action that draws from three independent, external influences (hypoxia, nickel, and hMSC passage) that intricately modulate the activities of three transcription factors (HIF1, p53, and c-myc) through dysregulated ROS, ultimately resulting in early transformation as elaborated in **Figure 2.7**. These findings illustrate a crucial aspect of hMSC passage-dependence: namely how cell senescence and transformation susceptibility are altered with increasing *in vitro* expansion, and how these events likely mirror those that occur during aging. To our knowledge, this is the first study to expose hMSCs to an environmentally-prevalent carcinogen while under hypoxia to mimic the physiologically-relevant transformation microenvironment. This study demonstrates the first step towards an experimental model of environmental carcinogen-driven hMSC transformation and will be used to design in-depth studies that aim to build a better understanding of the cell passage-dependent susceptibility of hMSCs to oncogenesis.

We investigated the combinatorial effects of hypoxia and nickel on the two passage groups of hMSCs and identified their mechanistic relationship (**Figure 2.7**). First, hypoxia stimulates a modest accumulation of HIF1 and p53 (**Figure 2.1B**), but hypoxia alone does not stimulate transactivation of p53-regulated genes because p53 is directly inactivated by HIF1[68,69]. In parallel, Ni exerts its effects through activation of the hypoxia response pathway, resulting in further accumulation and stabilization of HIF1[70]. Treatment with Ni alone also stimulates the accumulation of p53 (**Figure 2.1B**) but accumulated HIF1 inactivates p53 activity[69]. Therefore, the cooperative effects of hypoxia and Ni treatment synergistically amplify this cascade, resulting in a continually-increasing bias of proliferative, cell survival genes (HIF1-regulated) relative to apoptosis, cell cycle arrest genes (p53-regulated) (**Figure 2.2**). Additionally, late passage hMSCs have been shown to accumulate $O_2^{\cdot-}$ due to faulty redox mechanisms[6] (**Figure 2.4**) and downregulate genes and proteins associated with cell cycle regulation and the DNA damage response[9, 11] (i.e. decreased expression of p53, **Figure 2.2C**). Ni treatment has been shown to stimulate intracellular ROS production[75], which causes an overwhelming increase in oxidative stress that was seen in the present study to be well-tolerated by healthy P7-9 cells, but not late passage P12+ cells (**Figure 2.4**). In parallel, our data show that late passage hMSCs intrinsically express a higher basal level of the oncogenes c-myc and HIF1α with a concurrent reduction in p53 expression (**Figure 2.2C**). Because Ni and hypoxia further enhance the levels of c-myc and HIF1 expression, respectively, and also stimulate ROS production, the faulty redox mechanisms that are present in late passage cells, in cooperation with altered oncogene and tumor suppressor expression, appear to predispose late passage hMSCs to transformation susceptibility. Indeed, when implanted *in vivo* P12+ TI hMSCs resulted in the
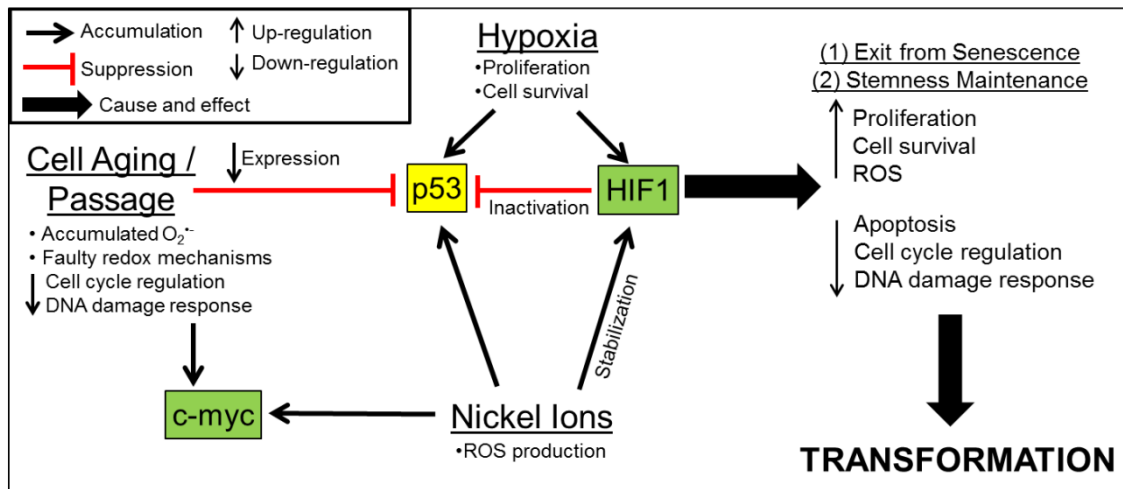
**Figure 2.7: Proposed mechanism by which the TI condition encourages cancerous transformation of late passage hMSCs.** This process involves three external modulators (hypoxia, Ni, and cell passage) that alter the activity of three internal regulators (p53, HIF1, and c-myc) to promote hMSC transformation. Oncogenes are shown in green boxes and tumor suppressor is shown in the yellow box. Hypoxia promotes proliferation and cell survival by accumulating HIF1 over p53 production, and upregulating the expression of HIF1-regulated genes. HIF1 directly inhibits transactivation of p53. Ni treatment causes the accumulation of c-myc over p53 production, and stabilizes HIF1, thereby further downregulating the expression of p53-regulated genes. Cell aging/passage result in accumulation of c-myc, decreased p53 expression, and buildup of ROS due to faulty redox mechanisms. In carcinogenic hypoxia, late passage hMSCs experience serial insults that promote their exit from senescence while maintaining expression of stemness markers, increasing proliferation, cell survival, and ROS, and decreasing apoptosis, cell cycle regulation, and the DNA damage response. These factors, when combined, are proposed to result in cancerous transformation of late passage hMSCs.

formation of tumor-like nodules whose activities more closely resembled those of classical tumors when compared to other groups, namely increased cellularity and proliferative index with decreased macrophage infiltration.

As described in Figure 2.7, these combined observations reveal that P12+ hMSCs exit a senescent state while maintaining strong expression of stemness markers and oncogenes. These alterations in cell behavior result in increased proliferation, cell survival, and ROS with a concurrent decrease in apoptosis, cell cycle regulation, and the DNA damage response, resulting in early hMSC transformation. Taken together with the analysis of *in vivo* tissue samples following implantation, these data suggest that late passage hMSCs in the TI condition most closely resemble an *in vitro* approximation of *in vivo* hMSC transformation, and can be used for further studies to elucidate fundamental inter- and extra-cellular mechanisms governing pathological changes in hMSC behavior.

CHAPTER 3


Specific Aim #2: Physicochemical polymer properties modulate hMSC redox and stemness status


**Introduction**


The goal of this Aim is to identify the influence of physiochemical matrix cues from the synthetic cell culture substrates on late passage hMSC behavior in terms of redox mechanisms and the expression of stemness genes/proteins (discussed in Chapter I). These matrix cues include stiffness, protein/cell adhesiveness, surface topography, and contact angle with water, all of which are regulated by the chemical composition of the material. The cellular response to these properties can be considered a "structure-function relationship" in which the material structure directly influences cellular functions, and surveying how cells respond to test polymer culture substrates with differing properties will provide insight for extrinsic regulation of these biological mechanisms by the polymers ("outside-in signaling").

In previous work from the Sung laboratory, a library of block copolymers was developed as cell culture substrates for regulating the behavior, phenotype, and oxidative activities of primary human coronary artery endothelial and smooth muscle cells (**SW Crowder** *et al. Acta Biomater* 2012)[82]. Following from this work, the current chapter is divided into three portions:

(i)     A brief discussion of the work referenced above in which the copolymers were synthesized and characterized in terms of the physicochemical and mechanical properties;

(ii)     A description and thorough characterization of the surface and biointerface properties of the copolymers;

(iii)     Observation and measurements of cellular behaviors when cultured atop the copolymer substrates


Copolymers composed of three subunits at varying molar ratios were employed for both first- and second-generation libraries: poly($\varepsilon$-caprolactone) (**PCL**) is a slow degrading, hydrophobic, biocompatible polymer that has been used in various biomedical applications[52, 83, 84]; poly(ethylene glycol) (**PEG**) is a hydrophilic polyether that can influence surface chemistry related to anti-adhesion of proteins and cells[85], bulk and degradation properties[86, 87] and oxidative activity[88, 89]; and, carboxyl PCL (**cPCL**) which carries a negative charge that improves hydrophilicity, can counteract repellent effects of PEG[89], and provides a site for functionalization of bioactive molecules to the polymer backbone[90]. Copolymers of *x* mole %

PEG, $y$ mole % PCL, and $z$ mole % cPCL are identified as $x$%PEG-$y$%PCL-$z$%cPCL where PEG-PCL is a block copolymer but cPCL addition is random within the PCL subunit (**Figure 3.1**)[91]
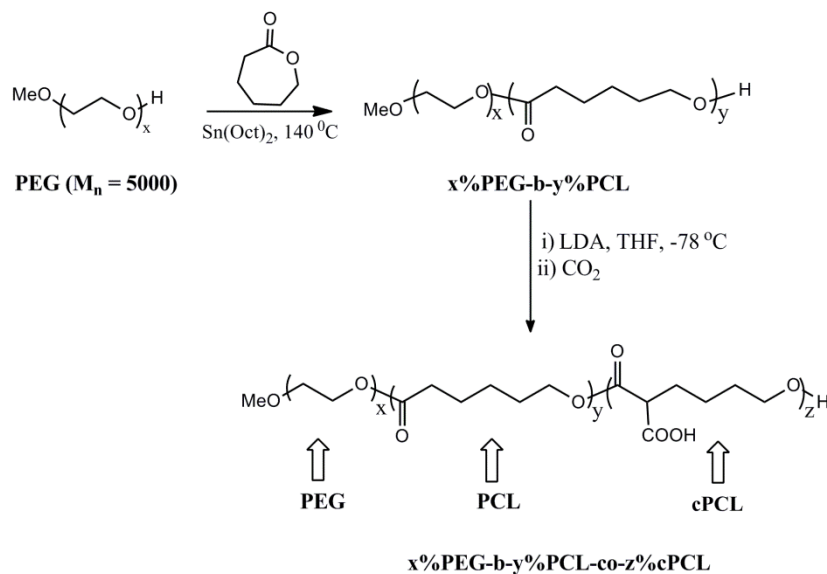


**Figure 3.1:** Synthesis scheme of PEG-PCL-cPCL copolymers by ring opening polymerization of ε-caprolactone monomer in the presence of 5,000 kDa PEG, followed by random introduction of a carboxyl group due to treatment with lithium diisopropyl amide (LDA). Adapted from SW Crowder *et al. Acta Biomater.* (2012)

## Materials and Methods

*Polymer Synthesis*

Poly(ethylene glycol) (PEG, $M_w$ = 5000) was purchased from Sigma Aldrich (St. Louis, MO). Poly(ε-caprolactone) (PCL) homopolymer as well as PEG, PCL, and carboxyl-PCL (cPCL) copolymers were synthesized according to methods previously described [90, 92, 93]. PCL polymers were synthesized by ring-opening polymerization and, in the case of copolymers, were extended from PEG. Terpolymers (i.e., polymers containing all three subunits) were synthesized according to the method reported previously [90], but with $x$%PEG-$b$-y%PCL as the starting material. Copolymers of $x$ mol % PEG, $y$ mol % PCL, and $z$ mol % cPCL were identified as $x$%PEG-$b$-y%PCL-$co$-z%cPCL where PEG-PCL is a block copolymer but cPCL addition is random within the PCL subunit. The polymers are abbreviated $x$%PEG-$y$%PCL-$z$%cPCL.

Polymer structure and molar percentages were confirmed by $^1$H NMR spectra: **100%PCL:** $^1$H NMR (CDCl$_3$) = $\delta$ 4.06 (t, 3H, -OCH$_2$), 2.31(t, 2H, -CH$_2$), 1.66 (m, 2H, -CH$_2$), 1.37 (m, 4H, -CH$_2$) ppm; **90%PCL-10%cPCL:** $^1$H NMR (CDCl$_3$) = $\delta$ 4.06 (t, 3H, -OCH$_2$), 3.4 (m, 1H, -CH-COOH), 2.31(t, 2H, -CH$_2$), 1.66 (m, 2H, -CH$_2$), 1.37 (m, 2H, -CH$_2$) ppm; **4%PEG-96%PCL:** $^1$H NMR (CDCl$_3$) = $\delta$ 4.06 (t, 3H, -OCH$_2$), 3.65 (s, 4H, -OCH$_2$), 2.31(t, 2H, -CH$_2$), 1.66 (m, 2H, -CH$_2$), 1.37 (m, 4H, -CH$_2$) ppm; **8%PEG-92%PCL:** $^1$H NMR (CDCl$_3$) = $\delta$ 4.06 (t, 3H, -OCH$_2$), 3.65 (s, 4H, -OCH$_2$), 2.31(t, 2H, -CH$_2$),

1.66 (m, 2H, -CH$_2$), 1.37 (m, 4H, -CH$_2$) ppm; **4%PEG-86%PCL-10%cPCL:** $^1$H NMR (CDCl$_3$) = δ 4.06 (t, 3H, -OCH$_2$), 3.4 (m, 1H, - CH-COOH), 2.31(t, 2H, -CH$_2$), 1.66 (m, 2H, -CH$_2$), 1.37 (m, 2H, -CH$_2$) ppm; **8%PEG-82%PCL-10%CPCL:** $^1$H NMR (CDCl$_3$) = δ 4.06 (t, 3H, -OCH$_2$), 3.4 (m, 1H, -CH-COOH), 2.31(t, 2H, -CH$_2$), 1.66 (m, 2H, -CH$_2$), 1.37 (m, 2H, -CH$_2$) ppm.

*Characterization of Physicochemical and Mechanical Properties (adapted from SW Crowder et al. 2012)[82]*

Copolymers were characterized by thermogravimetric analysis (TGA), differential scanning calorimetry (DSC), and dynamic mechanical analysis (DMA).  For testing mechanical and thermal properties, solvent cast films were prepared at 5% weight/volume (w/v) in dichloromethane (DCM), poured into a 100 mm glass Petri dish, left at room temperature in air overnight, and then placed under vacuum for two days to remove excess solvent.  Differential scanning calorimetry (Q1000, TA Instruments, New Castle, DE, USA) was performed with sample mass between 5 and 10 mg in aluminum pans with tops.  The procedure included two temperature sweeps from -80°C to 100°C with a ramp rate of 10°C / minute.  The values from the second sweep were reported such that thermal history was erased (n = 3).  Thermogravimetric analysis (TGA-1000, Instrument Specialist Inc., Twin Lakes, WI) was performed using a heating rate of 20$^o$C / minute to a final temperature of 600$^o$C.  Dried polymer powder was used for DSC and TGA experiments.

Dynamic mechanical analysis (Q800 DMA, TA Instruments) was performed with samples that were soaked in dH$_2$O at 37°C for 2 days prior to testing. Samples were hydrated prior to testing to evaluate the mechanical properties as they would be in physiological conditions.  Wet stress and strain were recorded using a submersion clamp containing dH$_2$O at room temperature.  A preload force of 0.1 N was applied to each sample and force was increased at a rate of 0.1 N/minute until failure.  The average Young's Modulus is reported (n = 3).  For temperature sweeps, a tension clamp was used with dry samples in air.  The procedure included two runs from -80°C to 50°C with a ramp rate of 20 °C/minute and a displacement of 30 μm at 1 Hz (original sample length was 25 mm).  All values were calculated using Universal Analysis software provided by TA Instruments.

*Thin Film Substrate Preparation for Cell Culture, and Surface/Biointerface Characterization*

Unless otherwise noted, all *in vitro* experiments were performed on spin-coated polymer films that were prepared with a commercial spin-coater (Laurell Technologies, North Wales, PA, USA). Circular glass cover slips (15 mm in diameter; Fisher Scientific) were first cleaned with 100% ethanol (Sigma Aldrich), rinsed with dH$_2$O, and heated to 80°C for ~20 min to dry.  A 1% weight/volume (w/v) solution of the specified polymer in tetrahydrofuran (THF, Sigma) was spun for 30 seconds at 3,000 RPM atop the clean glass cover slip (50 μl polymer solution / sample).  Samples were then exposed to constant

vacuum for ≥30 min to remove excess solvent and kept in a desiccator until use. For cell experiments, substrates were UV sterilized for 30-60 min on each side before use; for 15 mm cover glass or 3D scaffolds, samples were placed in a 24-well plate, and secured with an autoclaved silicon O-ring (McMaster Carr, Atlanta, GA, USA).

*Characterization of Surface Properties and Biointerface Properties*

Surface roughness was measured on dry, spin-coated samples by profilometry (Dektak 150 Surface Profiler, Veeco, Plainview, NY, USA) using a 2 mg force, a 1000 μm scan length over 10 seconds, and a 65.6 μm z-axis scan range. Ten measurements were made on each of three independent samples and the average deviation from the arithmetic mean (Ra) is reported. Protein adsorption was measured by quartz crystal microbalance with dissipation (QCM-D). Polymer was spin coated onto gold-coated quartz crystal (5 MHz, QSX 301; Q-Sense AB, Goetenberg, Sweden) using a ~50 ml of 10 mg / ml solution at 3000 rpm for 30 s using a spin coater (Headway Research Inc., TX). QCM-D measurements were carried out using a Q-Sense E4 instrument (Q-Sense AB, Goetenberg, Sweden) at 37.5 °C with 10% FBS, according to standard protocols[94]. The data were analyzed using Voigt model in the Q Tools software supplied by Q-Sense, Inc. Contact angle was performed with a goniometer (Ramé-Hart, Succassunna, NJ, USA) using 10 μl droplets of deionized water. Three measurements were taken on each of three independent samples, and the average advancing contact angle is reported (n = 9).

Surface topography was observed with a scanning electron microscope (Hitachi S-4200, Tokyo, Japan) at an accelerating voltage of 1 – 5 kV, after gold sputter coating (Cressington Scientific, Watford, United Kingdom) for 1 minute at a separation height of 6 cm. Samples that were exposed to PBS incubation were soaked in PBS overnight at 37°C in a humidified incubator, moved to a desiccator for at least one day to dry, and were then prepared for SEM. For collagen adsorption, spin-coated samples were incubated with fluorescein-labelled calf skin collagen (Elastin Products Inc, Owensville, MO, USA) at 100 μg / ml in PBS for at least two hours at 37°C in a humidified incubator, and were then rinsed four times with PBS before imaging. Fluorescent samples were imaged under a Nikon Eclipse Ti inverted fluorescence microscope (Nikon Instruments Inc, Melville, NY).

*Cell Culture*

hMSCs were either purchased from Lonza (Walkersville, MD, USA) or acquired from patients at Vanderbilt University Medical Center in cooperation with Dr. Pampee P. Young, according to previously published methods[95]. hMSCs were maintained in complete media (CM) composed of alpha-minimum essential media with nucleosides (Life Technologies, Carlsbad, CA, USA) with 16.7% fetal bovine serum (Life Technologies), 1% penicillin/streptomycin (Life Technologies), and 4 μg / ml plasmocin

(InvivoGen, San Diego, CA, USA). Cells were kept in a humidified incubator at 37°C and 5% $CO_2$, and media was replaced twice each week. When ~80% confluent, hMSCs were detached with 0.05% trypsin-EDTA, re-seeded at a density of 100 - 500 cell / $cm^2$, and cultured for 7-14 before reaching confluence (depending upon passage number). For all experiments, cells were seeded at a density of 10,000 viable cells / $cm^2$, as determined by exclusion of Trypan blue, and cultured for three days.

*Western Blot*

Western blots were performed with standard protocols, as described in Specific Aim #1. Primary antibodies included mouse anti-human APE/Ref-1 (1:4000, Abcam) and rabbit anti-human β-actin (1:2000, Abcam). HRP-conjugated secondary antibodies were raised in goat (1:3000, Abcam).

*Immunocytochemistry*

To measure cell proliferation by 5-bromo-2'-deoxyuridine (BrdU) incorporation, 20 μM BrdU was added to hMSC culture media for 16 hours; fixed with 4% paraformaldehyde (PFA, Sigma) for 15 min; permeabilized with 0.3% Triton-X (Sigma) for 15 min; and blocked with 10% goat serum (Sigma) for >2 hours, all at room temperature. DNA was denatured by treatment with HCl (1 N 10 min on ice, 2N 10 min at room temperature, followed by 20 min at 37°C, and neutralized with borate buffer (pH 9.0 ) for 12 min at room temperature). hMSCs were then incubated with 1:100 rat anti-BrdU primary antibodies (Abcam, Cambridge, MA, USA) overnight at 4°C, followed by incubation with 1:200 DyLight594-conjugated goat anti-rat secondary antibodies (Abcam) for 2 hours at room temperature, and counterstained with Hoechst (Sigma, 2μg / ml). For staining filamentous actin, hMSCs were fixed with 4%PFA and blocked with 10% goat serum, then incubated with AlexFluor488-labelled phalloidin (Life Technologies) in 1% bovine serum albumin (BSA) in PBS for 20 minutes, following the manufacturer's protocol. Cells were then washed and counterstained with Hoechst. Imaging was performed with a Nikon Ti inverted microscope (Nikon Instruments Inc., Melville, NY, USA). Percent proliferating cells represents the number of BrdU-positive cells out of the total number of cells in each field of view (n ≥ 12 images / group).

*ROS Measurement by Flow Cytometry*

hMSCs were incubated with 10 μM 5-chloromethyl-2',7'-dichlorodihydrofluorescein diacetate (CM-$H_2$DCFDA, Life Technologies) for 45 min at 37°C, trypsinized and pelleted by centrifugation (500x g, 5 min), and resuspended in 0.05% Trypan blue in PBS to quench extracellular fluorescence. Cells were then run on a FACS Calibur flow cytometer (BD Biosciences, Franklin Lakes, NJ, USA) and data were analyzed with FlowJo software (Tree Star Inc., Ashland, OR, USA).

*Conventional and Quantitative Real-Time Polymerase Chain Reaction (cPCR and qRT-PCR)*

hMSCs on spin-coated substrates were homogenized with the Trizol reagent (Life Technologies), mixed with chloroform (1:5 Trizol:chloroform), and separated by centrifugation (12,000x g, 15 min, 4°C). The RNA contained within the aqueous phase was then isolated with RNeasy columns (Bio-Rad, Hercules, CA, USA), according to the manufacturer's instructions. cDNA was synthesized using a kit (Applied Biosystems, Life Technologies) and qRT-PCR was performed with a SYBR Green master mix (Bio-Rad) with 15 - 20ng cDNA and 500 nM each of forward and reverse primers, using a CFX Real-Time PCR System (Bio-Rad). The qRT-PCR protocol included: 95°C for 3 min, followed by 40 cycles of denaturation at 95°C for 30 sec, annealing at 58°C 30 sec, and extension at 72°C for 30 sec. PCR array for extracellular matrix and adhesion molecules (SA Biosciences, Qiagen, Valencia, CA, USA) was performed according to the manufacturer's instructions. For cPCR, products were separated on a 2% agarose gel containing ethidium bromide for 15 minutes at 100V, and bands were visualized with a gel imaging station. For qRT-PCR, the expression of each gene of interest was normalized to expression of glyceraldehyde 3-phosphate dehydrogenase (GAPDH) as a housekeeping gene, generating the $\Delta C(t)$ value, and expression of $2^{-\Delta C(t)}$ with $n \geq 3$ biological replicates for each experiment is reported. Primer sequences are listed in Appendix I, and only those that showed single, specific amplicons were used for qRT-PCR experiments.

*Statistical Analysis*

Comparisons between two groups were performed with a Student's unpaired t test. Comparisons between multiple groups were performed with a one way analysis of variance (ANOVA) with a Tukey *post hoc* test to adjust p-values for multiple comparisons. In all cases, $p < 0.05$ is considered statistically significant. Mean ± standard deviation is reported, unless otherwise noted.

**Results**

*Physicochemical and Mechanical Copolymer Properties*

Thermal degradation of each polymer sample was first evaluated by TGA. The results reveal stability of all polymers up to 200°C, supporting their use in physiological applications at 37°C (Figure 3.2). DSC was then used to monitor changes in the thermal properties of different polymer compositions (Table 3.2). The enthalpy change ($\Delta H$) and melting temperature ($T_m$) of 100%PEG was higher than those of 100%PCL. Compared to 100%PCL, $\Delta H$ increased slightly upon addition of PEG to the PCL homopolymer (i.e., 4%PEG-96%PCL and 8%PEG-92%PCL), but decreased as cPCL was generated (i.e.,

90%PCL-10%cPCL) (**Table 3.1**). Interestingly, addition of both PEG and cPCL in the terpolymers (i.e., 4%PEG-86%PCL-10%cPCL and 8%PEG-82%PCL-10%cPCL) greatly decreased ΔH, compared to the test homo- and copolymers. Also, ΔH increased as the PEG content increased from 4% to 8% in the test terpolymers.  The DMA results showed that the wet glass transition temperature (Wet $T_g$) decreased as the PEG and/or the cPCL content(s) increased in the test polymer types (**Table 3.1**). In particular, in the test terpolymers, the addition of cPCL amplified the PEG effect, resulting in a further reduction of wet $T_g$.

DMA was used to evaluate the wet mechanical properties of the test polymers.  Upon generation of cPCL (i.e., 90%PCL-10%cPCL), the wet Young's modulus (E) and ultimate tensile strength ($\sigma_U$) decreased, compared to 100%PCL (**Table 3.1**).  Addition of PEG (i.e., 4%PEG-96%PCL and 8%PEG-92%PCL) also decreased these parameters compared to 100%PCL, but to a lesser extent than 90%PCL-10%cPCL.  In terpolymers, addition of both PEG and cPCL dramatically reduced E and $\sigma_U$, compared to the test homo- and copolymers, indicating the combined effects of PEG and cPCL on the mechanical properties.

In conclusion from the copolymer library, the three polymer subunits exhibited distinct characteristics and, when copolymerized at different molar ratios, the resulting polymer properties were
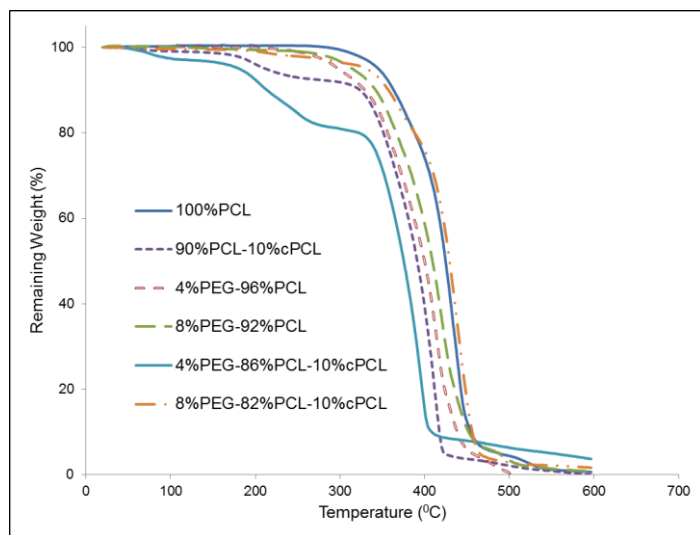


**Figure 3.2:** Thermogravimetric analysis (TGA) of copolymer library verifies that thermal degradation occurs only at 200°C and above, indicating the applicability of the polymers for use in physiological environments.  Adapted from SW Crowder *et al. Acta Biomater* (2012).

tailored, which could directly modulate cellular response (data not shown).  PCL is a semi-crystalline, hydrophobic polymer with slow degradation kinetics in aqueous environments [83, 84].  Addition of the random hydrophilic cPCL subunit or PEG block improved water absorption, facilitated hydrolytic cleavage, and resulted in a faster degradation rate (not shown).   In dry conditions, adding cPCL reduced enthalpy change and melting temperature, most likely due to decreased chain regularity and crystallinity (**Table 3.1**). Inclusion of the PEG block, however, increased these values.  It is hypothesized that this is due to improved chain packing and crystallinity, which is supported by the values for 100%PEG.  In wet

conditions, addition of either cPCL or PEG reduced $T_g$, E, and $\sigma_U$ (**Table 3.1**). This effect was further enhanced in the test terpolymers due to the increased water absorption by the hydrophilic subunits, which decreased crystallinity and reduced mechanical properties. Taken together, these data indicate the ability to tailor material properties through copolymerization techniques.

| Polymer Composition | $\Delta H$ (J/g) | $T_m$ (°C) | Wet $T_g$ (°C) | Wet E (MPa) | Wet $\sigma_U$ (MPa) |
|---|---|---|---|---|---|
| 100%PCL | $79.2 \pm 4.0$ | 58.0 | -57.5 | $232.6 \pm 49.6$ | $14.6 \pm 3.4$ |
| 90%PCL-10%cPCL | $73.7 \pm 1.4$ | 57.8 | -58.1 | $122.4 \pm 49.4$ | $7.0 \pm 2.5$ |
| 4%PEG-96%PCL | $82.2 \pm 2.3$ | 57.3 | -57.9 | $145.6 \pm 44.8$ | $11.9 \pm 3.3$ |
| 8%PEG-92%PCL | $91.3 \pm 5.5$ | 58.0 | -59.6 | $178.0 \pm 47.3$ | $13.0 \pm 4.0$ |
| 4%PEG-86%PCL-10%cPCL | $58.1 \pm 4.7$ | 57.0 | -59.8 | $43.6 \pm 2.9$ | $2.4 \pm 0.6$ |
| 8%PEG-82%PCL-10%cPCL | $71.0 \pm 1.1$ | 57.1 | -59.4 | $11.9 \pm 4.1$ | $0.6 \pm 0.3$ |
| 100%PEG | $216.7 \pm 4.3$ | 60.5 | N/A | N/A | N/A |

**Table 3.1: Thermal and mechanical copolymer properties.** Differential scanning calorimetry (DSC) data for change in enthalpy upon melting ($\Delta H$) and melting temperature ($T_m$) for the copolymer library. Wet glass transition temperature ($T_g$), wet Young's modulus (E), and wet ultimate tensile stress ($\sigma_U$) were obtained with dynamic mechanical analysis (DMA) using solvent casted polymer films incubated in $dH_2O$ for two days at 37 °C. 100%PEG was used as a reference polymer for thermal properties but could not be cast into films for DMA since it is soluble in water. For each, $n \geq 3$ independent measurements. All data are presented as mean $\pm$ SEM. Adapted from SW Crowder *et al. Acta Biomater* (2012).

*Characterization of Surface Properties and Biointerface*

A second batch of copolymers was synthesized for Specific Aim #2 of this dissertation project using the technique described above, but the molar ratios of PEG were increased in order to magnify the effect on cell behavior. These copolymers were formatted as thin, spin-coated films (~100nm) atop glass cover slips, and were characterized for protein adsorption by QCM-D, surface roughness by profilometry, surface topography by scanning electron microscopy (SEM), and hydro-phobicity/-philicity by contact angle with water. The copolymers were then sterilized and used as synthetic culture substrates for hMSCs *in vitro*, and the resulting cellular behavior was observed with an emphasis on alteration of redox status and expression of stemness genes/proteins.
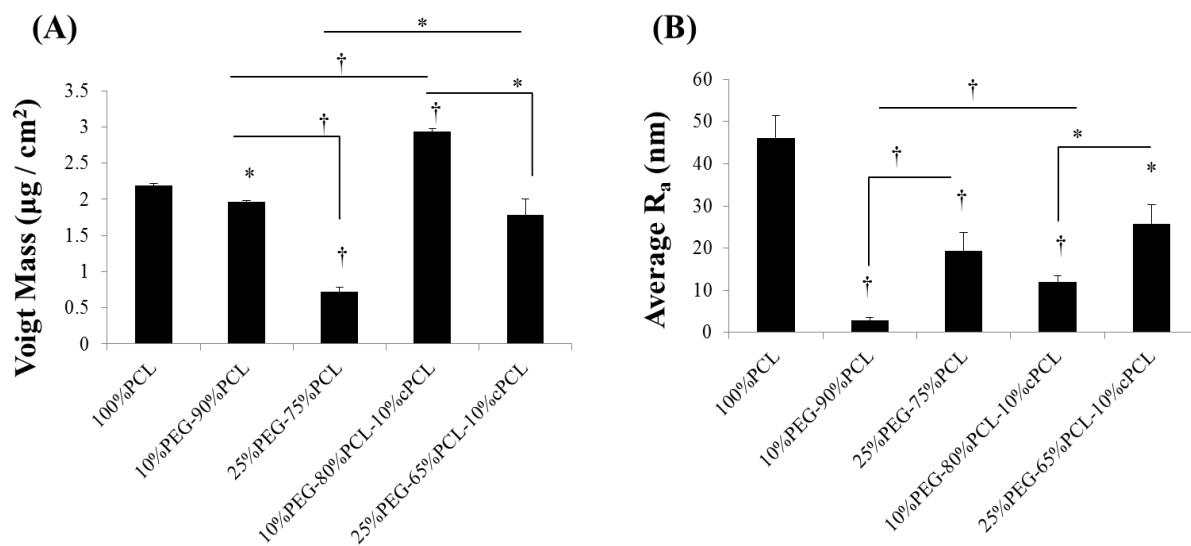


**Figure 3.3: Surface characterization of copolymer library.** (**A**) Protein adsorption measured by QCM-D and (**B**) surface roughness measured by profilometry. Increasing PEG composition resulted in decreased protein adsorption, but a rougher surface. The inclusion of cPCL improved protein adsorption, but created an even rougher surface. * $p < 0.05$, † $p < 0.005$ versus 100%PCL, or as indicated by lines.

The biointerface/surface properties of the copolymers were heavily influenced by chemical composition. Due to the protein-repellant effect of PEG, total protein adsorption was shown to decrease as the amount of PEG increased in the polymer composition, but this effect was rescued by the inclusion of the 10%cPCL component (**Figure 3.3**). The roughness of dry copolymer surfaces also varied greatly between copolymer types (**Figure 3.3**). The copolymerization with PEG decreased the roughness remarkably from 100% PCL but as the PEG content increased from 10 to 25%, the surface became more heterogeneous and rougher. The inclusion of the cPCL component exacerbated this effect. In order to observe the copolymer surface topography in both "dry" and "wet" conditions, samples were observed by

scanning electron microscopy (SEM, **Figure 3.4**) either directly after spin coat and vacuum drying ("dry", Rows A,B) or following overnight incubation in phosphate buffered saline (PBS) and then re-dried in a desiccator ("wet", Row C).  The 100%PCL homopolymer exhibited a classic appearance of a semi-crystalline polymer in which obvious grain boundaries with spotted crystal growth patterns were formed during spin-coating ("dry"), and were retained in the "wet" condition.   In contrast, the other four copolymers underwent alteration of the surface features in the "wet" samples, as compared to the "dry" conditions. 10%PEG-90%PCL and 10%PEG-80%PCL-10%cPCL formed large pores (~1-2 μm) when exposed to PBS whereas the "dry" 10%PEG-90%PCL samples had very small pores and the "dry" 10%PEG-80%PCL-10%cPCL samples exhibited virtually no pore formation but rather heterogeneous surface domains and patterns likely due to phase separation of the three copolymers[52, 96].  Furthermore, the 25%PEG-75%PCL sample exhibited a rough surface topography in both "dry" and "wet" conditions, and the 25%PEG-65%PCL-10%cPCL sample demonstrated a drastic rearrangement at the surface under "wet" conditions, as compared to "dry."  As shown in Figure 3.4 Row D, the effective surface topography of each polymer type was confirmed by adsorption of fluorescently-labelled collagen onto the samples. The 100%PCL homopolymer exhibited formation of obvious domains, as indicated by the conserved pattern at the sample surface (i.e. below the large, fluorescent aggregates).  In contrast, the 10%PEG-90%PCL sample exhibited a porous surface with homogeneous distribution of ~1-2 μm pores interspersed with larger, heterogeneous pores.   The fluorescence pattern of 25%PEG-75%PCL appeared homogeneous, similar to that of its corresponding "wet" SEM image.  The cPCL-containing copolymers demonstrated a high degree of porosity, with a more uniform distribution on the 10%PEG-80%PCL-10%cPCL sample, as compared to the 25%PEG-65%PCL-10%cPCL sample.  Since nanoscale surface topography has been shown to be a major regulator of hMSC phenotype and function[97], the inherent presence of pores that form at the surface of copolymers under aqueous conditions, and the preferential adsorption of the model protein collagen to the pore exterior, will undoubtedly play a critical role in how hMSCs respond to culture upon these materials.
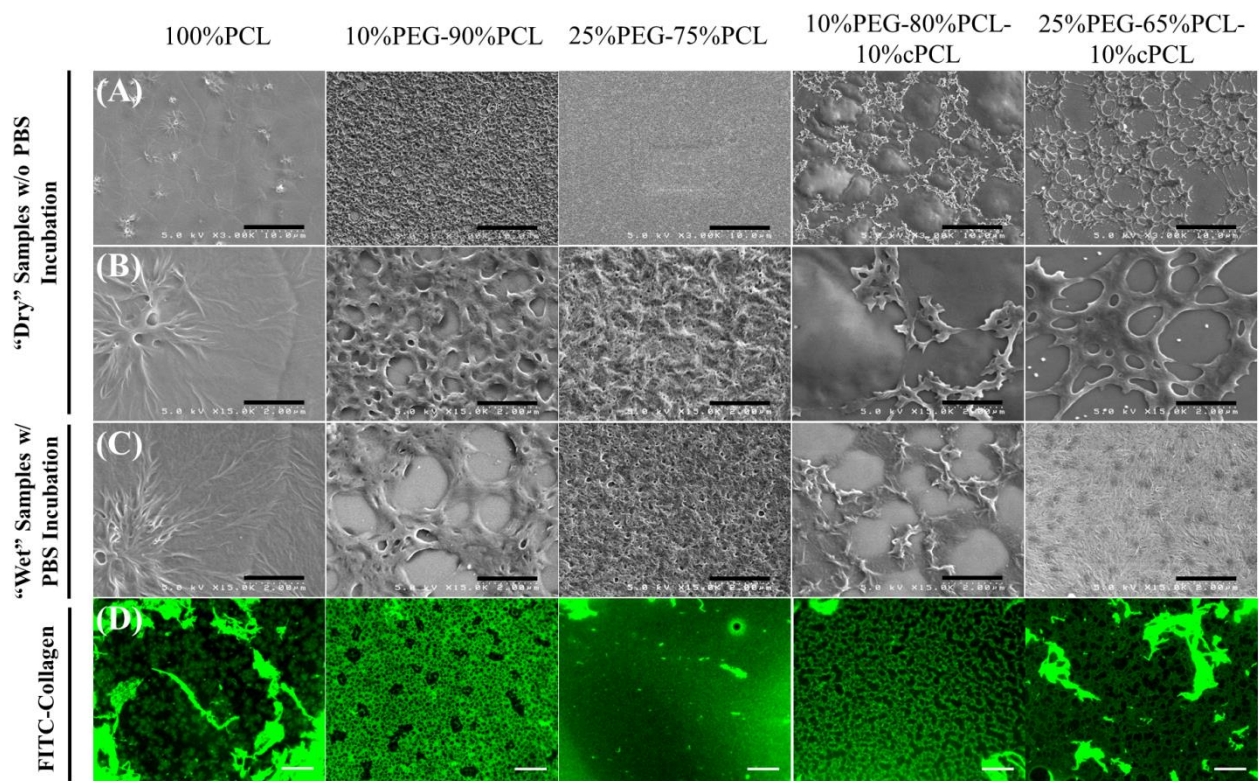
**Figure 3.4: Surface features and protein adsorption patterns of copolymer library.** Scanning electron microscopy images reveal surface topography for **(A-B)** dry and **(C)** wet spin-coated polymer samples. PEG-PCL and PEG-PCL-cPCL substrates were heavily influenced by exposure to an aqueous environment, resulting in rearrangement of the surface features. **(D)** Adsorption of fluorescein-labeled collagen demonstrates the formation of adsorptive and repellant domains at the polymer surface, confirming the features observed by SEM. Scale bars: (A) 10 μm, (B,C) 2 μm, (D) 20 μm.

| Contact Angle with Water (degrees) (Mean ± S.D.) | | |
|---|---|---|
| Polymer Composition | 0 hours (Dry) | 2 hours (Wet) |
| 100%PCL | 76.94 ± 2.32 | 79.23 ± 0.98 |
| 10%PEG-90%PCL | 69.43 ± 4.72 | 75.02 ± 0.49 |
| 25%PEG-75%PCL | 69.80 ± 1.57 | 71.12 ± 1.03 |
| 10%PEG-80%PCL-10%cPCL | 75.17 ± 2.67 | 74.41 ± 2.07 |
| 25%PEG-75%PCL-10%cPCL | 67.26 ± 2.26 | 56.84 ± 12.37 |

**Table 3.2: Copolymer library - contact angle with water**

Contact angle of the copolymers with water was greatly influenced by chemical composition. As seen in Table 3.2, contact angle for dry samples had little difference between the groups. However, following two hours of exposure to a humidified cell culture incubator, increasing amounts of PEG in the polymer chains resulted in a decreased contact angle (indicating increased hydrophilicity), and this effect was synergistically enhanced upon inclusion of cPCL.

*Response of Late Passage hMSCs to Copolymer Culture Substrates*

In order to continue the work from Specific Aim #1, late passage (P11+) hMSCs were cultured for three days on one of the copolymer substrates, or tissue culture polystyrene (TCPS) as a material control. Extensive *ex vivo* culture of hMSCs causes acquisition of abnormal gene and protein expression profiles that mimic *in vivo* aging[5, 9, 11]. Passage 8 (P8) hMSCs cultured on TCPS were used as a middle passage control undergoing early acquisition of abnormal behavior and ROS accumulation[9, 11]. As seen in Figure 3.5, the co/terpolymers elicited drastic alterations in hMSC morphology. In particular, the PEG-PCL copolymers, but not the cPCL-containing materials, stimulated formation of cell aggregates ("colonies"), likely due to the protein-repellant effect of PEG, which is counteracted by the cPCL (discussed above). In addition, as aforementioned, the unique pore size and distribution patterns seen in these copolymers might influence this cell morphology. The high percentage of PEG in the composition
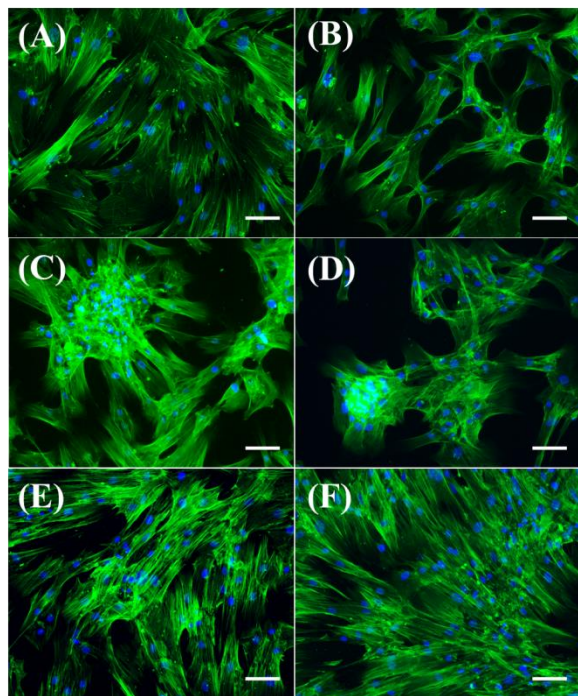


**Figure 3.5:** hMSCs cultured upon (**A**) TCPS or (**B-F**) copolymer substrates for three days, fixed, stained with phalloidin (green) and Hoechst nuclear counterstain. (**B**) 100%PCL, (**C**) 10%PEG-90%PCL, (**D**) 25%PEG-65%PCL, (**E**) 10%PEG-80%PCL-10%cPCL, (**F**) 25%PEG-65%PCL-10%cPCL. Scale bars = 100μm

of 25%PEG-75%PCL resulted in heterogeneity in cell seeding; in some cases, cells would adhere to the substrate and form distinct colonies (**Figure 3.5**), but within the same seeding condition, wells would exist with zero cell attachment. Because of the unpredictable nature of this substrate during experiments, its use in these studies was limited; however, the data collected are included for sake of completeness.

Intracellular ROS levels, as measured by DCFDA fluorescence by flow cytometry (FCM), and proliferation rate (BrdU$^+$ cells) were mediated by cues from the copolymer substrates (**Figure 3.6**). Both intracellular ROS levels (**Figure 3.6A**) and proliferation (**Figure 3.6B**) decreased for hMSCs cultured on 100%PCL, as compared to TCPS, and these levels decreased further when cultured on 10%PEG-90%PCL and 25%PEG-75%PCL substrates, with increasing amounts of PEG in the copolymer resulting in lower ROS levels and proliferation rates. 25%PEG-75%PCL exhibited a bimodal distribution of ROS levels, suggesting that two, distinct populations of hMSCs with differing intracellular statuses might co-exist on this material. Relative to the PEG-PCL copolymers, inclusion of cPCL in the polymer chain reversed the decrease in ROS and proliferation rate, effectively reinstating the hMSCs back to levels similar to that of TCPS. Interestingly, intracellular ROS levels correlated linearly with percent proliferating cells ($R^2 = 0.7832$, **Figure 3.6C**), which agrees with data that were collected in Specific Aim #1 (**Figure 2.4**). Since naïve stem cells tend to be slow-dividing with low levels of ROS[98], it is possible that the PEG-PCL copolymers might be stimulating a reversion to a more native stem cell phenotype, effectively acting as a synthetic niche for hMSCs.

Expression of the multifunctional APE/Ref-1 protein has been shown to decline in aging, senescent hMSCs, and forced expression via plasmid transfection can rescue the cells from senescence and lower intracellular ROS levels[6]. In order to identify how intracellular ROS are regulated by cell-biomaterial interactions, the expression of APE/Ref-1, p53, SESN1, and SESN2 were investigated (**Figure 3.7**). In agreement with previous reports[6], protein-level expression of APE/Ref-1 was downregulated in P11+ hMSCs cultured on TCPS, as compared to P8 hMSCs; however, expression was reinstated to varying degrees on all of the polymer substrates, with the strongest expression levels on 100%PCL and 10%PEG-90%PCL, and low expression on cPCL-containing polymers. Surprisingly, gene-level expression of all four redox-related mechanisms did not show statistical significance between culture substrates, although trends appeared in the data. Specifically, the expression of *APE/Ref-1* (**Figure 3.7B**) and *SESN1* (**Figure 3.7C**) were both upregulated on copolymers with increasing PEG content, and this effect was counteracted by cPCL. The average gene expression of *APE/Ref-1* and

**(A)**



Unstained Control
TCPS
100%PCL
10%PEG-90%PCL

Unstained Control
25%PEG-75%PCL
10%PEG-80%PCL-
10%cPCL
25%PEG-65%PCL-
10%cPCL

Counts

DCFDA Fluorescence

**(B)**



**(C)**



$R^2 = 0.7832$
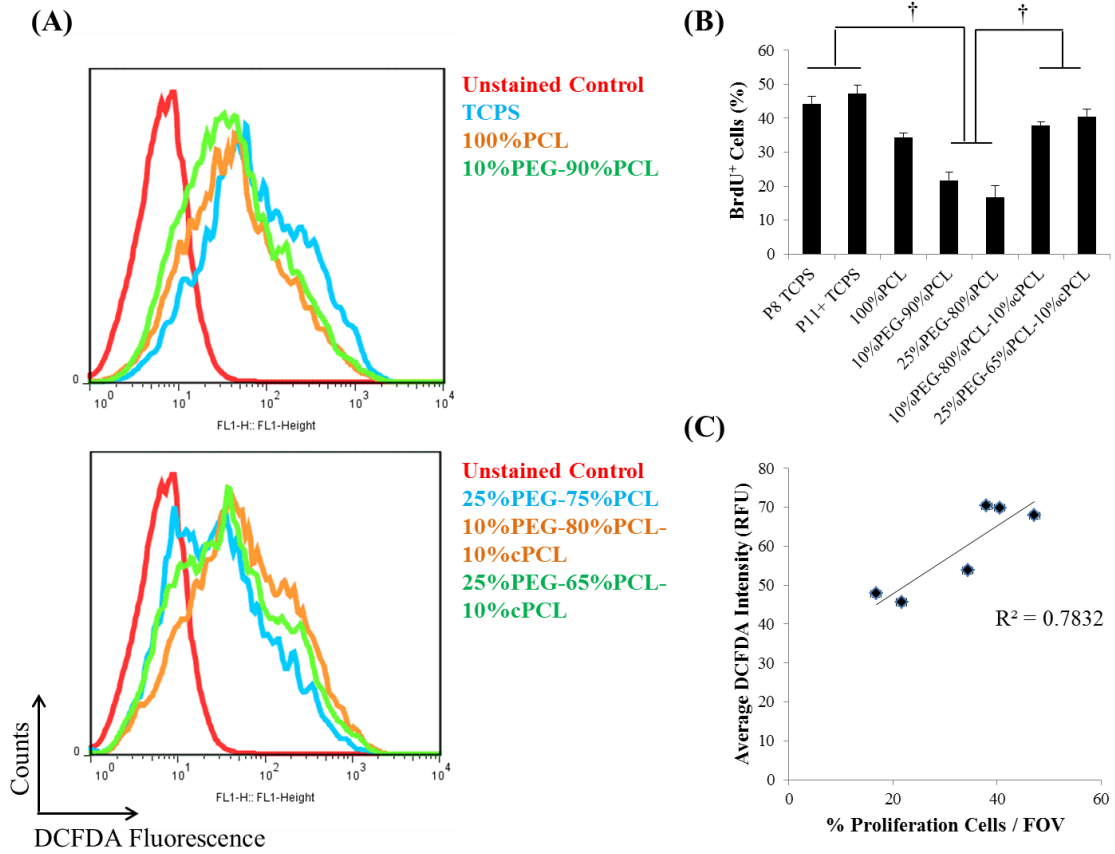
**Figure 3.6: Intracellular ROS and proliferation are altered by the culture substrate.** **(A)** ROS levels measured by flow cytometry and **(B)** percent proliferating cells by BrdU incorporation **(C)** correlate linearly with an $R^2$ value of 0.783. † $p < 0.01$ between groups indicated by the lines.

*SESN1* correlated linearly (**Figure 3.7D**, $R^2$ = 0.698).  Furthermore, the expression of *p53* (**Figure 3.7E**) and *SESN2* (**Figure 3.7F**) decreased in all P11+ hMSCs, as compared to P8 cells, and the composition of the copolymer substrate minimally affected these values, although their expression also correlated linearly (**Figure 3.7G**, $R^2$ = 0.885).   These data suggest that cell-biomaterial interactions can influence the expression of certain intracellular redox mechanisms, but with only limited efficacy.
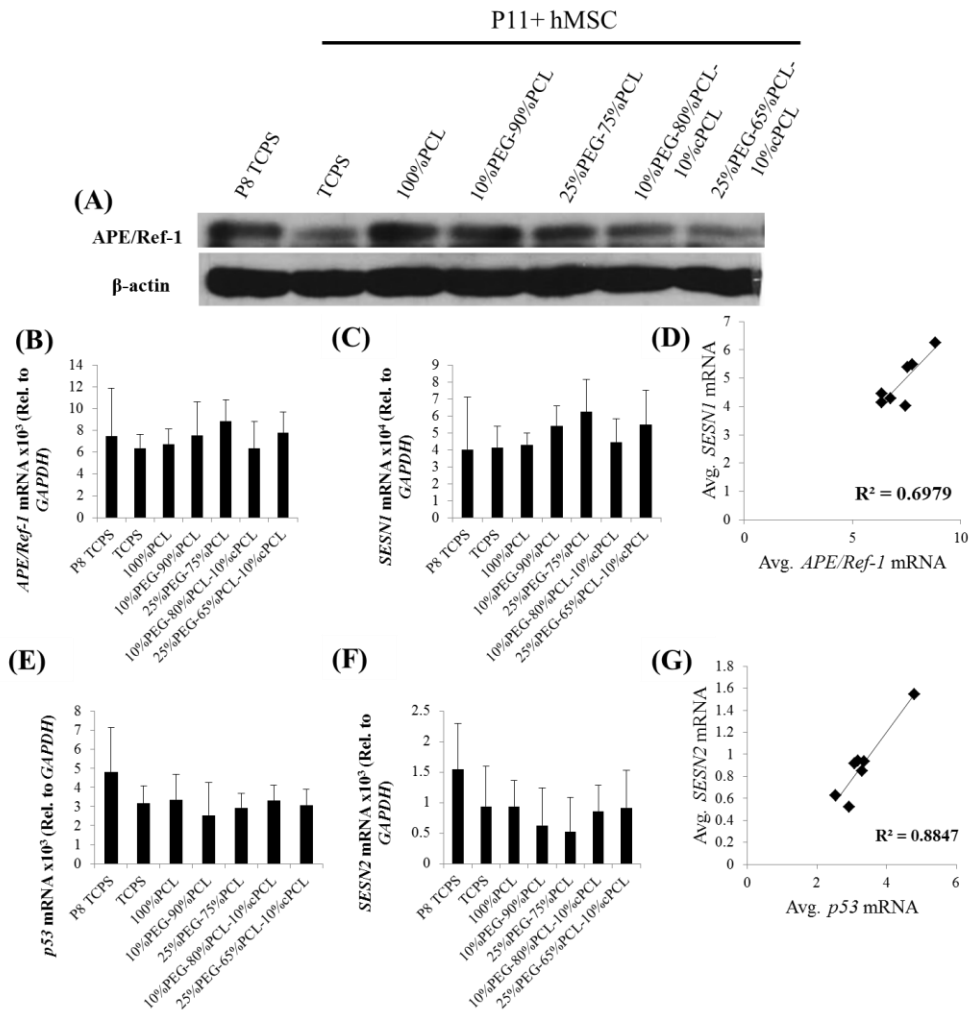


**Figure 3.7: Expression of redox-related genes and proteins on copolymer substrates. (A)** Western blot for APE/Ref-1 shows a decrease in P11+ hMSCs, relative to P8 cells, which can be reinstated to varying degrees following culture on copolymer substrates.  qRT-PCR data for **(B)** *APE/Ref-1*, **(C)** *SESN1*, **(E)** *p53*, and **(F)** *SESN2* reveal no significant differences between groups.   However, a correlation in trends was observed for **(D)** *APE/Ref-1* and *SESN1*, as well as for **(G)** *p53* and *SESN2*. N ≥ 4 biological replicates.
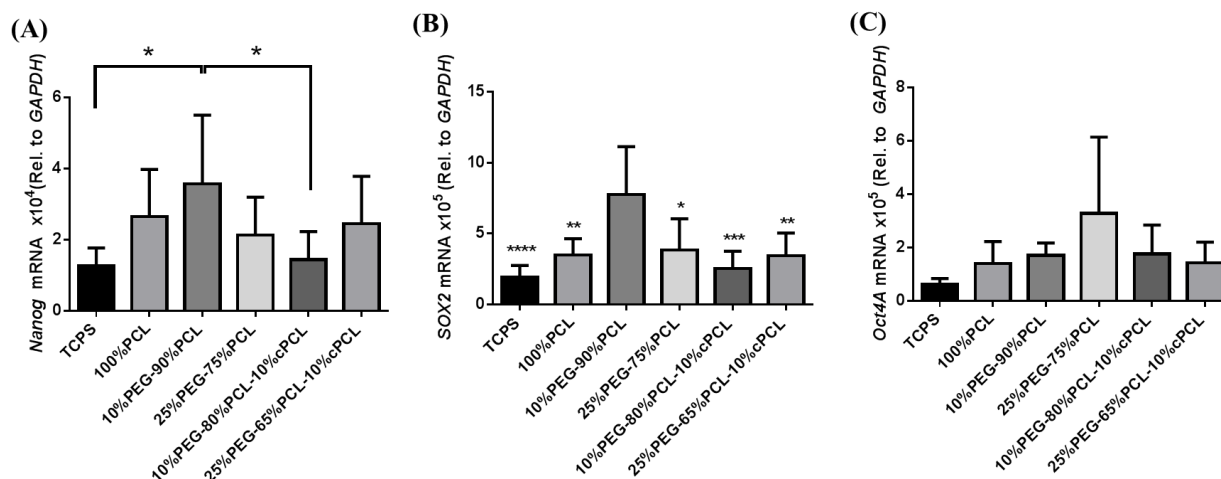
**Figure 3.8: Stemness gene expression is modulated by culture on the various copolymers**. qRT-PCR data for the stemness genes **(A)** *Nanog*, **(B)** *SOX2*, and **(C)** *Oct4A*. Although no significant changes were observed for *Oct4A*, P11+ hMSCs cultured on 10%PEG-90%PCL demonstrated a significant increase in *Nanog* and *SOX2* expression, compared to TCPS and various other polymers. *$p < 0.05$, ** $p < 0.01$, *** $p < 0.005$, **** $p < 0.001$ versus 10%PEG-90%PCL, or as indicated by lines. $N \geq 4$ biological replicates.

The regulation of the stemness genes, *Nanog, SOX2*, and *Oct4A* on the copolymer substrates was next evaluated by qRT-PCR (**Figure 3.8**). Interestingly, P11+ hMSCs cultured on 10%PEG-90%PCL exhibited the strongest upregulation of *Nanog* (**Figure 3.8A**) and *SOX2* (**Figure 3.8B**), but no significant change was observed for *Oct4A* (**Figure 3.8C**). Surprisingly, the expression trends of the stemness genes did not follow any material parameter (i.e. PEG/cPCL content, contact angle, roughness, or protein adsorption), which stimulated a question of how outside-in signaling at the cell-biomaterial interface was driving the observed increase.

In order to begin to identify how interactions at the cell-biomaterial interface regulate intracellular ROS levels and expression of stemness markers, a PCR array (SA Biosciences) was performed that focused on extracellular matrix proteins and adhesion molecules. As seen in Figure 3.9, several potential "hits" showed promise during the initial screening, including intercellular adhesion molecule 1 (ICAM-1), integrin $\alpha_2$ (ITGA2), platelet-endothelial cell adhesion molecule (PECAM-1), osteopontin (OPN), and several matrix metallotproteinases (MMPs) (**Figure 3.9A**). When confirmed by qRT-PCR with multiple biological replicates, the genes with significant change in expression level on 10%PEG-90%PCL included ITGA2, OPN, PECAM-1, MMP3, MMP10, and MMP13 (**Figure 3.9B**). In order to verify that the qRT-PCR data did not falsely depict increased expression of all tested targets, integrins $\alpha_6$ (ITGA6) and $\beta_1$ (ITGB1) were measured since their expression did not change in the original PCR array screen (**Figure 3.9A**).

**Conclusions**

The data contained within this Chapter indicate the ability to control hMSC behavior and function by solely changing the chemical composition of the synthetic culture substrate, without adding extrinsic biochemical mediators. Copolymerization techniques allow for variation of material properties by altering the molar ratio of the copolymer subunits, thereby affecting the overall chemical composition. Shown here, the material properties that were systematically changed with chemical composition include thermal characteristics and phase changes ($T_g$, $\Delta H$, $T_m$ – **Table 3.1**), protein adsorption (**Figure 3.3**), surface roughness (**Figure 3.3**), and contact angle (**Table 3.2**). Additionally, differences in surface topography due to interactions with water and phase separations were seen by SEM of the polymer surfaces, and preferential adsorption patterns for collagen was dictated by these features (**Figure 3.4**). Furthermore, when aging hMSCs were cultured atop these copolymer substrates, their morphology (**Figure 3.5**) and intracellular mechanisms were altered. For example, intracellular ROS levels, along with proliferation status, were readily altered on the various substrates, and were shown to correlate linearly (**Figure 3.6**). Interestingly, the narrow panel of redox-related genes that was investigated did not
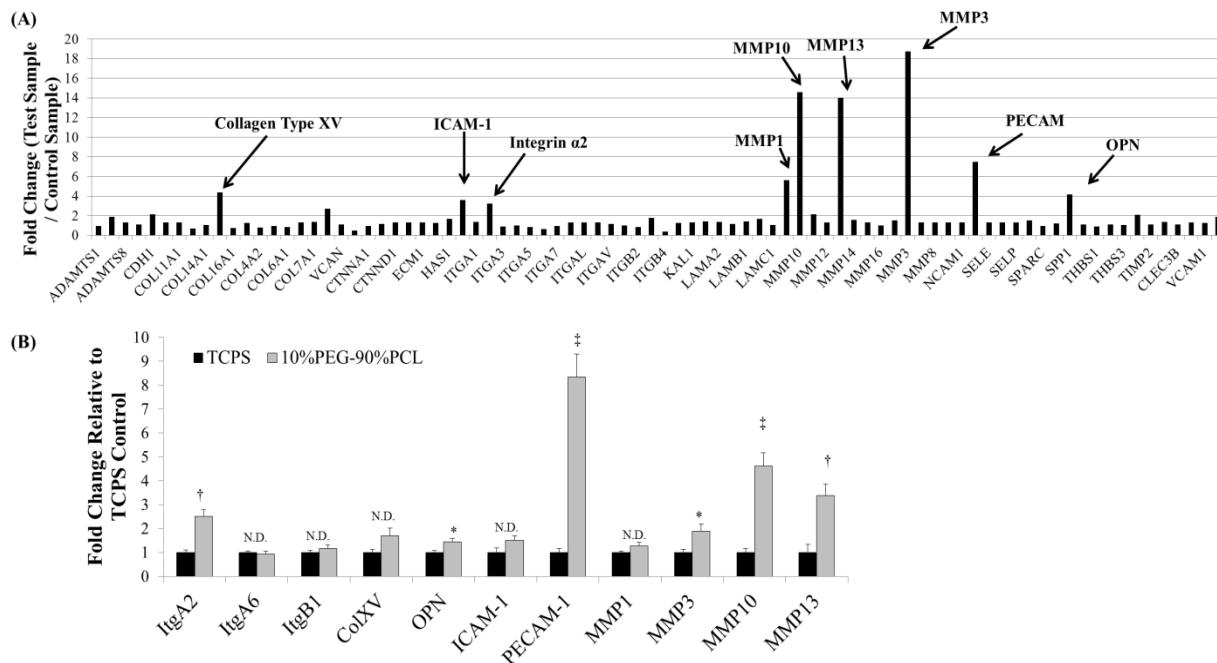


**Figure 3.9: (A)** PCR array for extracellular matrix and adhesion molecules produced several potential "hits" for how the cell-biomaterial interface is regulating/influencing intracellular ROS and stemness changes (N = 1 for PCR array screen). **(B)** Confirmation of PCR array data with N = 4 biological replicates verifies specific genes with significant upregulation on 10%PEG-90%PCL versus TCPS, including *ItgA2*, *OPN*, *PECAM-1*, *MMP3*, *MMP10*, *MMP13*. $* p < 0.05$, $\dagger p < 0.01$, $\ddagger p < 0.005$ versus TCPS.

show significant differences between groups, but revealed proportional correlations in gene-level expression between *APE/Ref-1* and *SESN1*, as well as *p53* and *SESN2* (**Figure 3.7**). When the expression of the stemness genes *Nanog*, *SOX2*, and *Oct4A* was measured, hMSCs cultured on 10%PEG-90%PCL exhibited a significant increase in two of these three factors, relative to TCPS (**Figure 3.8**). Since naïve stem cells are known to exhibit low levels of intracellular ROS[98], reduced proliferation, and strong expression of stemness genes, it is possible that the 10%PEG-90%PCL substrate acts as a synthetic niche for reverting hMSCs back to a more physiologically-relevant phenotype. To identify potential mechanisms at the cell-biomaterial interface driving the observed increase in stemness, a PCR array was performed that focused on extracellular matrix and adhesion molecules, and a number of potential cell-cell interaction, cell-matrix interaction, and matrix remodeling genes-of-interest were identified (**Figure 3.9**). To this point, the ability to regulate stem cell functions by altering material properties has been demonstrated. In the following Chapter, the role of the copolymer substrate in regulating cell function is investigated, with a systematic approach to identify the key mechanisms of the cell-biomaterial interaction(s) driving this event.

CHAPTER 4


Specific Aim #3: Phenotypic regulation of hMSCs by polymer substrates: implication of
increased stemness and pericyte characteristics


**Introduction:**


In Chapter III of this dissertation, hMSC behavior was shown to be regulated by culture atop synthetic copolymer substrates through mechanisms that remain heretofore undefined. In the current Chapter, hMSCs cultured atop 10%PEG-90%PCL substrates will be thoroughly analyzed for their phenotype and function by qRT-PCR, Western blot, immunocytochemical staining, flow cytometry, *in vitro* functional assays, and *in vivo* implantation. For this portion of the study, young (i.e. low passage) hMSCs will be used in order to evaluate the effect of the polymer in a more clinically-relevant model, as low passage cells are usually used for therapeutic purposes. hMSCs derived from patients at Vanderbilt University Medical Center will first be evaluated for their expression of upregulated factors that were observed in Chapter III. Then, the gene- and protein-level expression profiles of a commercial hMSC source will be analyzed, with regard to maintenance of hMSC stemness and pericyte phenotype. Next, implantation of hMSCs cultured within three-dimensional, porous scaffolds fabricated from 10%PEG-90%PCL into immunocompromised mice will be evaluated for blood vessel formation and maturation using techniques such as optical coherence tomography (OCT). Finally, potential mechanisms driving the outside-in signaling at the hMSC-polymer interface will be systematically identified with specific inhibition of each mechanistic factor influencing the observed changes in hMSC behavior, eventually leading to novel, fundamental insights regarding hMSC identity. The data generated in this dissertation, culminating in the final points of this Aim, demonstrate a novel approach for material-mediated control over hMSC function, providing new methodologies for generating a homogeneous hMSC population with a pro-angiogenic, pericyte-like phenotype.


**Background:**


*hMSCs and Pericytes*

In 2008, Crisan *et al.* demonstrated that perivascular cells (i.e. pericytes) isolated from multiple human organs exhibited characteristics distinctly similar to those of hMSCs[99]. In particular, pericytes were identified by a panel of markers, such as positive expression for CD146, platelet-derived growth

factor receptor beta (PDGFRβ), neuron-glial antigen 2 (NG2), and alpha-smooth muscle actin (αSMA), and negative expression of vascular endothelial cadherin (VE-cadherin), Von Willebrand factor (vWF), and PECAM. The isolated pericytes demonstrated multilineage differentiation capacity *in vitro* (adipogenic, chondrogenic, osteogenic, myogenic), and exhibited an expression profile of surface proteins identical to that of hMSCs (i.e. CD105$^+$, CD90$^+$, CD146$^+$, CD44$^+$ ; CD34$^-$, CD133$^-$, CD45$^-$) both when serially-expanded *in vitro*, as well as in the native perivascular niche *in vivo*. These findings raised a fundamental question of pericyte/hMSC identity: are all hMSCs actually pericytes[100]?

Pericytes, also known as mural cells, are a supportive, mesenchymal cell type that is embedded within the vascular basement membrane of blood microvessels[101, 102]. Pericytes are known to make direct contacts with the endothelium ("peg-socket type") and participate in the development, stabilization, and maturation of vasculature through both physical interactions and paracrine signaling mechanisms[101, 103, 104]. The recruitment of pericytes to newly-formed vasculature stimulates the production of new basement membrane *in vitro*[105]. Furthermore, the CD146$^+$ fraction of perivascular cells, but not unfractionated MSCs or CD146$^-$ cells, have been shown to maintain the undifferentiated state of human hematopoietic stem cells, suggesting a critical role for pericytes in the bone marrow niche[106]. Although similar in lineage to vascular smooth muscle cells (VSMCs), the localization and marker expression of pericytes appear to be unique. Pericytes typically express αSMA, NG2, PDGFRβ, and regulator of G-protein signaling 5 (RGS5)[101, 104, 107], but this expression profile can be altered in certain circumstances, such as tumor angiogenesis and wound healing[108].

Pericytes regulate endothelial function through specific signaling pathways, including transforming growth factor beta (TGF-β)/TGFβR, PDGF/PDGFR, and Angiopoietin-1 (Ang1)/Ang2/Tie2[101, 103]. Each of these ligand/receptor combinations is tightly controlled *in vivo* and represents a mutual relationship between pericytes and endothelial cells (ECs), leading to diverse and often contradictory effects, such as pericyte recruitment, pericyte loss, vessel sprouting, or vessel stabilization[101, 103]. Of particular interest for this dissertation project is the Ang1/Ang2/Tie2 signaling pathway. The Tie2 receptor is predominantly expressed on endothelial cells and activation by its primary agonist, Ang1[109], leads to endothelial cell proliferation[110], vessel stabilization and pericyte coverage[101]. *In vivo* treatment with an Ang1-encoding plasmid enhances the formation of collateral vessels in ischemia-induced angiogenesis[111], and *in vitro* Ang1 treatment of ECs results in the upregulation of proliferation, migration, and survival genes, while downregulating proapoptotic and cycle regulatory genes[112]. Furthermore, *in vitro* Ang1 exposure stimulates the recruitment of smooth muscle cells through EC-mediated release of hepatocyte growth factor[113] and heparin binding EGF-like growth factor[114]. In contrast, the secondary Tie2 ligand, Ang2, antagonizes Ang1 activity by competitively binding the Tie2 receptor, but by itself is not sufficient for stimulating signal transduction[115], thereby interrupting Ang1

functionality[101, 113]. Ang2 is, however, required for certain developmental events, such as postnatal angiogenesis and lymphatic patterning[116], indicating that its effects are not simply redundant. Instead, it is believed that the opposing activities of Ang1 and Ang2 support a paradigm in which constitutive Ang1/Tie2 activity regulates fundamental vascular homeostasis, and the dynamic Ang2 activity playing a role in short-lived processes with specific outputs. To this end, ECs are known to produce Ang2 and maintain it in stored Weibel-Palade bodies with the ability to rapidly secrete the molecule to produce an autocrine effect[117]. Ang1, however, is produced predominantly by perivascular cells and not ECs, maintaining steady-state vascular homeostasis[118]. In the context of vessel angiogenesis, Ang1 activation of Tie2 results in vessel stability and pericyte coverage whereas the presence of Ang2 antagonizes Ang1, leading to lack of Tie2 activation, pericyte loss, and vessel sprouting[101, 118]. Therefore, the interplay of Ang1 and Ang2 in regards to EC homeostasis, pericyte function, and angiogenesis is complex, highly regulated, and their balance is critically important for vascular function.

*hMSCs and Pericytes in Tissue Engineering*

While the use of hMSCs for regenerative therapies has exploded in the last decade, applications of pericytes in tissue engineering remain largely uninvestigated. As expected, that majority of tissue engineering efforts with pericytes have involved the generation and stabilization of vascular networks. For example, one recent paper produced cell sheets from *in vitro* co-culture of endothelial, osteogenic, and CD146^{+} perivascular cells, and showed that the stability of the vascular network was enhanced when implanted *in vivo*, as evidenced by improved integration with host vasculature and increased vessel diameter[119]. In a 2010 study, a group from the University of Pittsburgh evaluated synthetic polymer scaffolds loaded with human pericytes to generate small-diameter tissue engineered vascular grafts[120]. The authors implanted the pericyte-loaded scaffolds (or unseeded control scaffolds) as an aortic interposition graft in a rat model for eight weeks and found that a significantly higher degree of patency was observed with the seeded scaffolds, and a tissue architecture that resembled that of native vasculature was present. The study possessed significant pitfalls, however, since the authors did not compare the pericyte-loaded scaffolds with that of any other cell type, instead only an unseeded control. Furthermore, aside from the measurement of patency, most comparisons were made between the pericyte-loaded scaffold and the native aorta, as opposed to the control scaffold, making interpretation of the pericyte contribution unclear.

Aside from using bona fide pericytes in tissue-engineered constructs, several investigations have attempted to used MSCs as a pro-angiogenic supporting cell type for vascular applications[121-126], exploiting their inherent phenotypic relationship to pericytes. One elegant study implanted hMSCs with

43

ECs in a collagen/fibronectin gel into immunodeficient mice, revealing stable vasculature formation for more than 130 days[127]. Interestingly, hMSCs alone could not form functional vasculature *in vivo*, indicating that the hMSCs themselves were not undergoing EC differentiation in this context but rather orchestrating a regulated event. **The specific differences between hMSCs and pericytes tend to be unclear in the recent literature.** To address this issue, two papers were published in 2013 that have demonstrated functional differences between the two cell types. In a short communication to *Small*, Zouani *et al.* developed a micro-patterned system *in vitro* to study the ability of pericytes to stabilize EC tubes without collapsing[128]. The authors showed that pericytes, but not hMSCs, were able to migrate through a mock basement membrane to maintain the integrity of EC tubes, whereas the MSC-supported tubes were collapsed at 16 hours post-incubation. In parallel to these findings, a series of *in vitro* assays were used to distinguish the differing abilities of pericytes and hMSCs[129]. Using three different co-culture models with human ECs, the authors demonstrated that human placenta-derived pericytes, but not hMSCs or fibroblasts, were able to stabilize EC tubes in 2D culture atop Matrigel, promote the spontaneous extension of angiogenic sprouts in 3D co-culture, and stimulate the formation of interconnected, multi-layer EC cords. Furthermore, the authors showed that only the CD146$^+$ fraction of pericyte or hMSC populations were able to maintain EC tubes and stimulate sprouting, suggesting a potential for overlap between the two seemingly-distinct cell types.

*Maintenance of hMSC Phenotype*

The majority of investigations regarding hMSC phenotype have focused on directed differentiation toward a specific lineage. These include, but are not limited to, the classical differentiation pathways[1], such as osteogenic[32, 130-134], chondrogenic[135-138], and adipogenic[133, 139] lineages. However, as discussed in Chapters I and II, hMSCs serially-expanded *ex vivo* acquire senescence-associated abnormalities that resembles *in vivo* aging, thereby negating their therapeutic potential. Because of this, some researchers have considered concepts beyond the realm of directed hMSC differentiation, instead focusing on maintenance of stemness (an undifferentiated phenotype) in order to prevent spontaneous differentiation. For example, a 2011 study from *Nature Materials* described the use of nanoscale surface "pits" to maintain the undifferentiated state of hMSCs[97]. Through a simplistic fabrication method, the authors generated a flat poly(caprolactone) (PCL) surface with nanometer-scale pits (120nm deep) spaced at a uniform 300nm center-to-center distance, or offset by 50nm in a random direction. The authors had previously shown that the offset pattern generated the most effective osteogenic differentiation[134], and took the reciprocal route in this paper by studying the surface whose properties most effectively *prevented* differentiation. The equally-spaced pits were shown to retain hMSC stemness, as evidenced by the protein-level expression of Stro-1 and ALCAM, two naïve hMSC markers, and gene-level expression of

CD63 and ALCAM.  This study raised a fundamental question of the physiological state of hMSCs and the *in vivo* niche: What is a mechanism by which the extracellular environment modulate quiescence/maintained stemness versus proliferation/differentiation?

*Extracellular Matrix Cues Influence hMSC Fate and Function*

  In 2006, Engler *et al.* published a seminal paper regarding extracellular matrix-derived cues on hMSC fate[24].  Using a crosslinked poly(acrylamide) (PA) gel system coated covalently-linked collagen, the authors showed that hMSCs would commit to specific lineages based solely on the stiffness/elasticity of the underlying substrate.  Interestingly, the stiffness of the *in vitro* system appeared to correlate with the *in vivo* analogue for the tissue type to which the cells were differentiating (i.e. soft matrix stimulated neuronal differentiation, a matrix of moderate stiff stimulated myogenic differentiation, and a stiff matrix stimulated osteogenic differentiation).  This paper seemed to revolutionize how the tissue engineering and stem cell biology communities thought about cell mechanosensing and outside-in signaling.  However, in 2012 a study was released in *Nature Materials* that refuted the findings of Engler and colleagues, showing that, although the same results were produced with PA gels, a similar material system composed of poly(dimethyl siloxane) (PDMS) could not induce the same cellular response when fabricated to corresponding stiffness values[25].  Instead, the authors were able to elegantly prove that the observed effect was, in fact, stimulated by the *spacing* of the tethered extracellular matrix molecules (i.e. collagen), which was a function of PA crosslink density and effectively modulated intracellular tension.  From this article, it became clear that the events occurring at the cell-biomaterial interface are undeniably complex and cannot be reduced to a single variable to explain large-scale, global changes within the cells.

*hMSC Expression Profile in Stemness and Differentiation*

  The hMSC expression profile tends to be confusing as many of the markers overlap with other cell types while other markers increase or decrease during differentiation, often in a time-dependent manner.  The commonly-accepted hMSC profile includes: $CD13^+$, $CD44^+$, $CD49a^+$, $CD49b^+$, $CD63^+$, $CD90^+$, $CD105^+$, $CD146^+$ and $CD11b^-$, $CD34^-$, $CD45^-$, $CD133^-$ [140]. Three additional markers that are considered to define undifferentiated, naïve hMSCs from the bone marrow include CD63 (HOP-26), ALCAM (activated leukocyte cell adhesison molecule, CD166), and STRO-1[97, 141].  The STRO-1 monoclonal antibody marks the fraction of adult bone marrow that possesses osteogenic differentiation capacity[142] and colony forming potential[143].  STRO-1 has been considered the best marker of hMSCs[140] despite the fact that, until recently, its antigen was unknown.  In 2011, the antigen to which the STRO-1 antibody binds was determined to be a 75kDa protein found in mature ECs, raising an even deeper question of what is the nature and function of the STRO-1 antigen?  Despite this lack of knowledge,

STRO-1 remains an important marker for isolating hMSCs and can be used to monitor the undifferentiated status of these cells since it decreases with *ex vivo* expansion[144]. Interestingly, pericytes are also known to be positive for STRO-1[106] which further suggests an *in vivo* relationship between the two cell types that might be lost in culture.

To date, the most comprehensive phenotypic profile of the hMSC surface proteome was performed in 2011 by Niehage and colleagues in which they identified almost 900 proteins present in the plasma membrane by mass spectrometry and confirmed specific proteins-of-interest with flow cytometry[145]. In short, the authors verified the commonly-accepted profile of hMSCs, identified several novel membrane-bound proteins, and were able to classify how protein expression levels changed during osteogenic and adipogenic differentiation. Relative to uninduced hMSCs, adipogenic induction caused an increase in expression for CD63, CD71, CD146 and CD166/ALCAM, whereas osteogenic differentiation induced an increase in CD54 and CD166 expression. Although both CD63 and ALCAM have been used as markers of undifferentiated hMSCs in high-impact literature[97], it is clear from this study that these markers might not be a fair representation of stem cell status and potential. In particular, ALCAM increased for both osteogenic and adipogenic differentiation in the Niehage study, and was shown over fifteen years ago to be involved in osteogenesis as the $F_{ab}$ fragment of ALCAM antibodies to MSCs undergoing osteogenic induction accelerated the process[146]. Therefore, STRO-1, CD63, and ALCAM appear to be useful markers for isolating naïve hMSCs, but ALCAM expression is not a clear measure of the undifferentiated status of hMSCs during culture.

*Goals of Aim3 Studies*

Three critical transcription factors, Oct4A[147], Nanog, and SOX2, are known to maintain the undifferentiated state of embryonic stem cells (ESCs) and also play a role in the maintained stemness of hMSCs. In particular, free-floating aggregates of hMSCs have been shown to exhibit enhanced expression of Oct4 and SOX2, which is mediated through CD49f (integrin $\alpha_6$)[148]. Furthermore, as hMSCs are expanded *in vitro*, the expression levels of Oct4 and Nanog have been shown to decrease, resulting in spontaneous differentiation and a hyper-methylated epigenetic state[149]. In regards to biomaterial culture substrates, only a few studies have investigated the expression of hMSC stemness genes in response to changing material cues[150-152], indicating that material-mediated control of hMSC stemness is an under-investigated topic from which both clinical and basic science applications could benefit. Therefore, the goals of this Aim are described in Figure 4.1, and include:

(1)  Characterize and verify the expression profile for hMSCs cultured on the 10%PEG-90%PCL copolymer substrate using early passage cells from a commercial source and samples from multiple patients at Vanderbilt University Medical Center;

(2)  Determine the biological relevance of the PEG-PCL hMSCs by:
   (2a) Measuring the effects of PEG-PCL or TCPS hMSCs on HUVECs *in vitro*;
   (2b) Evaluating the influence of PEG-PCL hMSCs on vascularization *in vivo*

(3)  Understand the structure-function relationship between the material properties and hMSC behavior through:
   (3a) Hypothesis of the interfacial mechanism driving the observed hMSC phenotype;
   (3b) Designing experiments to decouple material properties in order to identify specific parameters driving the outside-in signaling events.
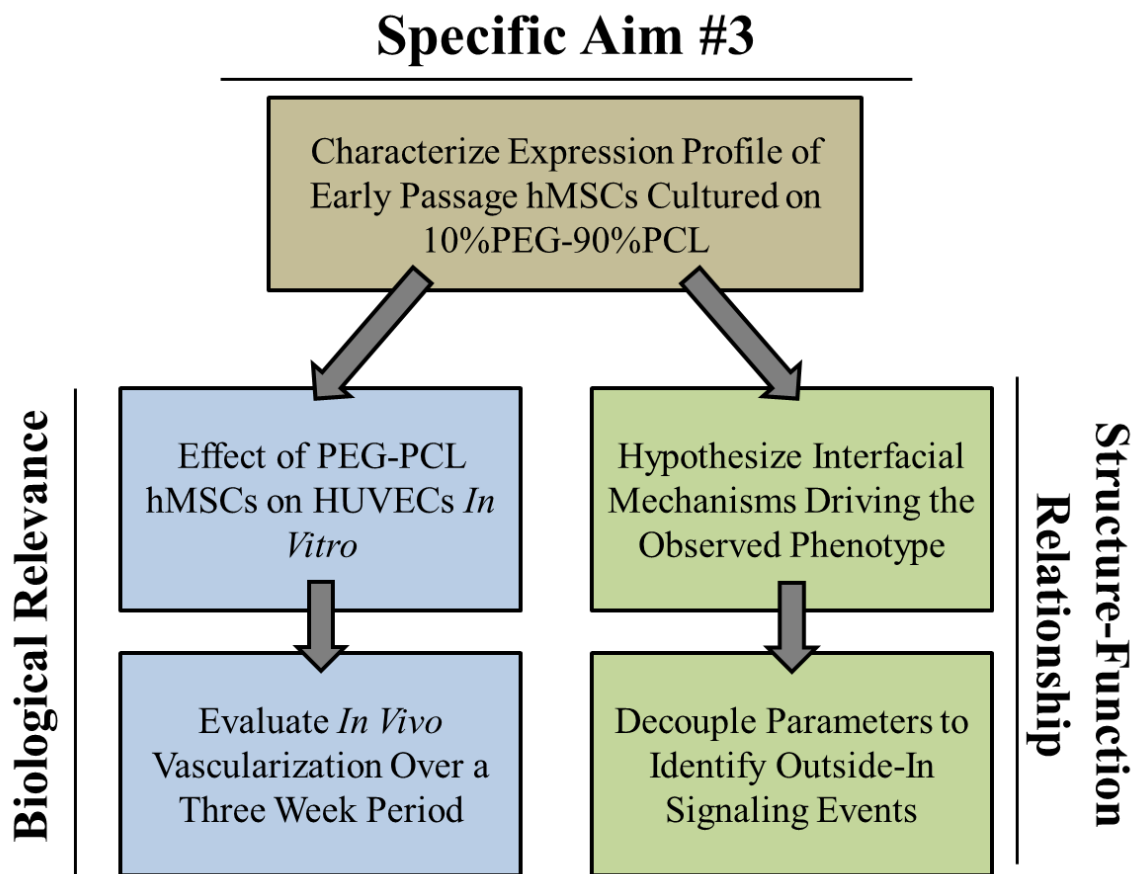


**Figure 4.1:** Specific aim #3 flow of experiments to determine biological relevance and structure-function relationship for hMSCs cultured atop PEG-PCL copolymer substrates.

**Materials and Methods**

*Substrate Preparation for Test Polymers*

Unless otherwise noted, all *in vitro* experiments were performed on spin-coated polymer films that were prepared with a commercial spin-coater (Laurell Technologies, North Wales, PA, USA). 15mm circular glass cover slips (Fisher Scientific) were first cleaned with 100% ethanol (Sigma Aldrich), rinsed with dH$_2$O, and heated to 80°C for ~20 min to dry. A 1% weight/volume (w/v) solution of the specified polymer in tetrahydrofuran (THF, Sigma) was spun for 30 seconds at 3,000 RPM atop the clean glass cover slip (50 µl polymer solution / sample). For preparation of "large-scale" Petri dish polymer films, Pyrex Petri dishes (Corning) were cleaned as described above, and 1 mL of a 1% w/v solution of polymer in THF was spun for 2 min at 1,500 RPM to coat the surface. All samples were then exposed to constant vacuum for ≥30 min to remove excess solvent and kept in a desiccator until use. For preparation of salt-leached, three-dimensional polymer scaffolds, 500 mg polymer was dissolved in 10 ml dichloromethane (DCM) and poured over 12 g of NaCl salt crystals of specified size (size range 212 µm – 450 µm, achieved using two different size sieves) in a Teflon dish, allowed to dry in a chemical fume hood overnight, then further dried under vacuum for 1 hr to remove any remaining solvent. Scaffolds were cut into the specified size (~15mm or ~6mm for 24-well or 96-well plate culture, respectively, using metal punches) and kept in dH$_2$O on a shaker at room temperature for 3 days to remove salts, with water changed twice daily. Scaffolds were moved to a desiccator until use. For cell experiments, substrates were UV sterilized for 30-60 min on each side before use; for 15mm cover glass or 3D scaffolds, samples were placed in a 24-well plate, and secured with an autoclaved silicon O-ring (McMaster Carr, Atlanta, GA, USA).

*Cell Culture*

hMSCs were either purchased from Lonza (Walkersville, MD, USA) or acquired from patients at Vanderbilt University Medical Center in cooperation with Dr. Pampee P. Young, according to previously published methods[95]. hMSCs were used before passage 6 for this Aim, and were maintained in complete media (CM) composed of alpha-minimum essential media with nucleosides (Life Technologies, Carlsbad, CA, USA) with 16.7% fetal bovine serum (Life Technologies), 1% penicillin/streptomycin (Life Technologies), and 4 µg / ml plasmocin (InvivoGen, San Diego, CA, USA). For chemically-defined media (CDM) experiments, CDM was purchased from Lonza (TheraPEAK MSCGM-CD) and did not contain fetuin-A (personal communication with company). For serum concentration experiments, media with antibiotics and anti-mycoplasma agent was mixed with a predetermined amount of FBS to yield the desired concentration. Cells were kept in a humidified incubator at 37°C and 5% CO$_2$, and media was

replaced twice each week. When ~80% confluent, hMSCs were detached with 0.05% trypsin-EDTA, re-seeded at a density of 100 - 500 cell / cm$^2$, and cultured for 7-14 days before reaching confluence (depending upon passage number). For all experiments, cells were seeded at a density of 10,000 viable cells / cm$^2$, as determined by exclusion of Trypan blue, and cultured for three or seven days, as noted.

*Protein Adsorption and Liquid Chromatography-Mass Spectrometry/Mass Spectrometry (LC-MS/MS)*

Complete culture media was added to wells of a 24-well plate (0.5ml / well) and proteins were allowed to adsorb to the material surface overnight (n ≥ 3 wells / material). Media was then removed, and the surfaces were gently washed three times with PBS to remove unadsorbed proteins. Radio immunoprecipitation assay (RIPA) buffer containing protease and phosphatase inhibitors was then added to each well. Eluted protein was measured by the BCA assay (Pierce, Thermo Scientific, Waltham, MA, USA) against a bovine serum albumin (BSA) standard curve. At least three independent wells for each substrate type were quantified and the average is reported. Proteins were then loaded onto a 10% Novex gel (Life Technologies), resolved approximately 1 cm into the gel, and then stained with colloidal Coomassie[153]. The entire contents of each lane were subjected to in-gel trypsin digestion and resulting peptides analyzed by a 70 minute data dependent LC-MS/MS analysis. Briefly, peptides were autosampled onto a 200 mm by 0.1 mm (Jupiter 3 micron, 300A), self-packed analytical column coupled directly to a linear trap quadrupole (LTQ, ThermoFisher) using a nanoelectrospray source and resolved using an aqueous to organic gradient. A series of a full scan mass spectrum followed by 5 data-dependent tandem mass spectra (MS/MS) was collected throughout the run and dynamic exclusion was enabled to minimize acquisition of redundant spectra. MS/MS spectra were searched via SEQUEST against a bovine database (UniprotKB− reference proteome set) that also contained reversed version for each of the entries[154]. Identifications were filtered and collated at the protein level using Scaffold (Proteome Software).

*Western Blot*

Western blot was performed with standard protocols, as described in Specific Aim #1. Primary antibodies are described in Appendix I, and HRP-conjugated secondary antibodies were raised in goat (1:3000, Abcam).

*Immunocytochemistry and Immunophenotyping by Flow Cytometry*

hMSCs were fixed with 4% paraformaldehyde (PFA, Sigma) for 15 min, permeabilized with 0.3% Triton-X (Sigma) for 15 min when probing intracellular targets, and blocked with 10% goat serum (Sigma) for >2 hours, all at room temperature. hMSCs were then incubated with primary antibodies in

1% BSA (Appendix I) overnight at 4°C, followed by incubation secondary antibodies (AlexaFluor488-, AlexFluor-550, or AlexaFluor594-conjugated goat anti-mouse or anti-rabbit at 1:500; Abcam, Cambridge, MA, USA) in 5% goat serum for 2 hours at room temperature, and counterstained with Hoechst (Sigma, 2μg / ml). Imaging was performed with a Nikon Ti inverted microscope (Nikon Instruments Inc., Melville, NY, USA) and images were processed with ImageJ (National Institutes of Health, Bethesda, MD, USA).

For flow cytometry, unstained hMSCs were used to set voltages for the fluorescence and scatter channels. Single-stained hMSCs were used to determine compensation values so that fluorescence signal within one channel was definitively from a positively-stained cell. Cells were then run on a FACS Calibur flow cytometer (BD Biosciences, Franklin Lakes, NJ, USA). Each experiment represents 10,000 gated cells, and data were analyzed by FlowJo software (Tree Star Inc., Ashland, OR, USA).

*Conventional and Quantitative Real-Time Polymerase Chain Reaction (cPCR and qRT-PCR)*

hMSCs on spin-coated substrates were homogenized with the Trizol reagent (Life Technologies), mixed with chloroform (1:5 Trizol:chloroform), and separated by centrifugation (12,000x g, 15 min, 4°C). The RNA contained within the aqueous phase was then isolated with RNeasy columns (Bio-Rad, Hercules, CA, USA), according to the manufacturer's instructions. cDNA was synthesized using a kit (Applied Biosystems, Life Technologies) and qRT-PCR was performed with a SYBR Green master mix (Bio-Rad) with 15 - 20ng cDNA and 500nM each of forward and reverse primers, using a CFX Real-Time PCR System (Bio-Rad). The qRT-PCR protocol included: 95°C for 3 min, followed by 40 cycles of denaturation at 95°C for 30 sec, annealing at 58°C 30 sec, and extension at 72°C for 30 sec. For cPCR, products were separated on a 2% agarose gel containing ethidium bromide for 15 minutes at 100V, and bands were visualized with a gel imaging station. For qRT-PCR, the expression of each gene of interest was normalized to expression of glyceraldehyde 3-phosphate dehydrogenase (GAPDH) as a housekeeping gene, generating the $\Delta C(t)$ value, and expression of $2^{-\Delta\Delta C(t)}$ relative to the TCPS control with $n \geq 3$ biological replicates for each experiment is reported. Primer sequences are listed in Appendix I and only those that showed single, specific amplicons were used for qRT-PCR experiments.

*In Vitro Evaluation of Conditioned Media and Lumen Formation*

Red fluorescent protein (RFP)-transfected human umbilical vein endothelial cells (rHUVECs) were purchased from Angio-Proteomie (Boston, MA, USA), maintained in MesoEndo culture media (Cell Applications, Inc., San Diego, CA, USA) and used before passage 10. For migration experiments, 100,000 HUVECs per well were seeded in commercial transwell migration plate with 8 μm pores (Corning Inc., Corning, NY, USA) at $n \geq 3$ independent wells / group. After four hours, HUVECs that

had not migrated from the top layer were physically removed with a sterile cotton-tipped applicator, and the insert was then fixed in 10% formalin, 84% methanol, and 6% water for five minutes. Cell nuclei were then stained with Hoechst (2 μg / ml) and imaged at 10x magnification with n ≥ 6 images / sample. The average number of migrated nuclei in each image is reported.

For co-culture studies, hMSCs were cultured on TCPS or PEG-PCL for three days, then removed and mixed with rHUVECs (1 hMSC : 2 rHUVECs) and cultured in 1:1 MesoEndo:CM in type-I collagen gels (1.4 mg / ml) for 48 hours before fixation (n ≥ 4 independent samples / group). Co-cultures were then permeabilized and stained with AlexaFluor488-conjugated phalloidin (Life Technologies) and imaged under a confocal microscope (Zeiss LSM 710). For quantification, lumen were counted and measured (ImageJ) in each image, and the averages are reported with n ≥ 4 images / sample.

*In vivo experiments*

Three-dimensional scaffolds of either 100%PCL or 10%PEG-90%PCL were cut into 6 mm discs, sterilized by UV exposure for 1 hour on each side, placed into 96-well plates, and held in place with silicon O-rings. The bottom of the 96-well plates was first coated with 1% agarose to prevent cell attachment, following previously published protocols[148]. hMSCs were seeded at a density of $10^5$ cells / scaffold (or left in culture media for "blank" scaffolds) and cultured for one week in complete media before subcutaneous implantation into the ventral region of athymic, NU/J Foxn1$^{nu/nu}$ male nude mice (6-8 weeks of age, n = 8 animals, The Jackson Laboratory, Bar Harbor, ME, USA). Four types of scaffolds were used for this experiment: 100%PCL without cells ("blank"), 100%PCL seeded with hMSCs, 10%PEG-90%PCL without cells ("blank"), and 10%PEG-90%PCL seeded with hMSCs. One of each scaffold type was implanted into the same animal, totaling four scaffolds per animal into eight animals.

Speckle variance optical coherence tomography (OCT) was used for *in vivo* imaging[155]. To visualize projection images of the vasculature within the implanted scaffolds, volume data sets were processed with a speckle variance technique that computes the variance in each pixel over seven repeated A-lines at each lateral position. The resulting speckle variance images represent OCT flow signal for perfused vessels within the imaged volume. Noise due to signal fall-off was excluded by thresholding the corresponding structural images to create a mask, and an average signal projection over the depth (∼1 mm) of the speckle variance OCT data was used to visualize all vessels present in the volume. Images were enhanced with an optimized, modified Frangi filter[156] to enhance vessel-like features, and the enhanced image was multiplied by the initial image to accentuate the vessels. Quantification of vessel density was performed using MATLAB (MathWorks, Natick, MA, USA) built-in Canny edge detection[157] to find edge features, and active contours to mask in edges, and the vessel density was calculated as the mask pixels over total pixels in the image.

Comparisons between two groups were performed with a Student's unpaired t test. Comparisons between multiple groups were performed with a one way analysis of variance (ANOVA) with a Tukey *post hoc* test to adjust p-values for multiple comparisons. In all cases, $p < 0.05$ is considered statistically significant. Mean ± standard deviation is reported, unless otherwise noted.

## Results

*Early Passage hMSC Gene and Protein Expression Profile*

Specific Aims #1 and #2 focused on late passage, aging hMSCs as a model for *in vivo* aging, with increased susceptibility to oncogenic insult (Aim #1) or biomaterial-mediated manipulation of cell function (Aim #2). However, because clinical uses of hMSCs involve only brief *ex vivo* expansion, the current Aim employs early passage hMSCs as a more clinically-relevant model for tissue engineering therapies.

PECAM is expressed by all cells within the vascular compartment, including leukocytes, platelets, and endothelial cells (ECs)[158]. Classically, pericytes are considered to be negative for CD31 expression[99, 107], but debate regarding pericyte identification remains in the literature[108]. Integrin $\alpha_2$ (ITGA2) is predominantly expressed by endothelial cells attaching to the basement membrane and is indispensable for angiogenesis both *in vitro* and *in vivo*[159, 160]. Because PECAM and ITGA2 were the most significantly upregulated genes tested in the PCR array in Specific Aim #2 (**Figure 3.9**), and both of these proteins are readily found in the vasculature, the next direction of this project focused upon identifying the phenotype of hMSCs resulting from culture on 10%PEG-90%PCL (from here, this polymer will be referred to as PEG-PCL). Although hMSCs demonstrate potential for vasculogenic differentiation[161, 162], and MSCs and ECs can both originate from a common mesodermal precursor[163], the expression of PECAM alone is not sufficient to simply assume endothelial differentiation. Therefore, hMSCs cultured on TCPS or PEG-PCL were tested for pericyte markers at the protein level by immunostaining and for endothelial-specific markers at the gene level in order to further clarify their behavior.
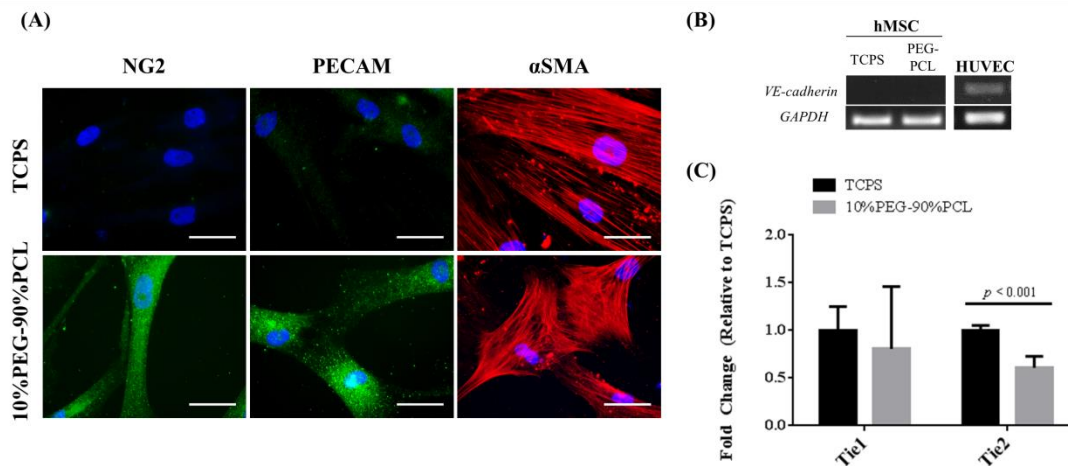
**Figure 4.2:** Pericyte and endothelial marker expression for hMSCs cultured on TCPS and PEG-PCL. **(A)** Immunofluorescent staining for pericyte markers NG2, PECAM, and αSMA reveal positive expression for all three markers on PEG-PCL, but not TCPS. Scale bars = 50 μm **(B)** Conventional PCR (cPCR) verifies that hMSCs do not express VE-cadherin. **(C)** Quantitative real-time PCR (qRT-PCR) demonstrates a significant reduction in *TIE2* expression, but not *TIE1*.

As seen in Figure 4.2, hMSCs cultured on PEG-PCL expressed markers that are used to identify pericytes, including NG2, PECAM, and αSMA, whereas hMSCs cultured on TCPS expressed only αSMA, for which hMSCs are known to be positive. VE-cadherin, Tie1, and Tie2 are typical markers of ECs that play critical roles in vascular morphogenesis, stability, and remodeling[101, 164], and their expression was investigated at the gene level by conventional and quantitative RT-PCR (**Figure 4.2B,C**). hMSCs from either TCPS or PEG-PCL did not express detectable levels of *VE-cadherin* (**Figure 4.2B**), suggesting that the observed phenotype is not endothelial. Furthermore, although *Tie1* expression did not change between the two groups, *Tie2* expression decreased significantly for PEG-PCL hMSCs. Therefore, this expression profile (NG2$^+$, PECAM$^+$, αSMA$^+$; *VE-cad*$^-$, *Tie1*$^+$, and *Tie2*$^{low}$) suggests a phenotype that is more reminiscent of naïve pericytes than ECs.

To further characterize the expression of Lonza hMSCs cultured on TCPS or PEG-PCL, the expression of markers observed in Specific Aim #2 was measured at the gene- and protein-levels. Early passage Lonza hMSCs (passage < 6) did not exhibit a change in the expression of stemness genes *Nanog* or *SOX2* on PEG-PCL, but significantly increased the expression of both *PECAM* and *ITGA2* (**Figure 4.3A**). By immunofluorescent staining, the increased expression of ITGA2 was confirmed (**Figure 4.3B**). When observed by scanning electron microscopy (SEM), the colonies that formed on PEG-PCL appeared to have two distinct layers: a bottom layer that spanned the cell-biomaterial interface, and a top layer that grew as a more rounded cluster (**Figure 4.3 C,D**). As shown in Figure 3.3E, the cell aggregate interacted directly with the material surface, where the pores of the material surface were in contact with extensions from the cell aggregate.
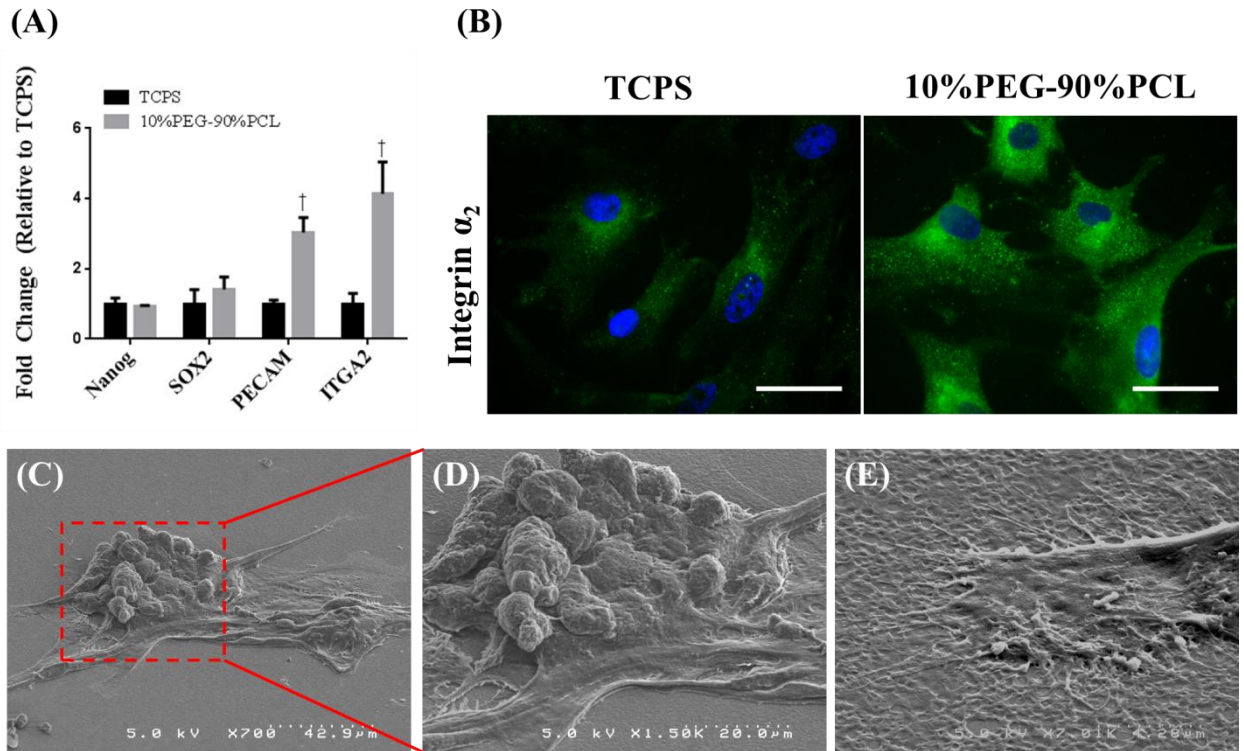
**Figure 4.3:** Characterization of Lonza hMSCs on PEG-PCL following three-day culture. **(A)** qRT-PCR demonstrates a significant increase in the expression of *PECAM* and *ITGA2*. † $p < 0.01$ versus TCPS. **(B)** Immunofluorescent staining confirms a protein-level increase of integrin $\alpha_2$ expression on PEG-PCL as compared to TCPS. Scale bars = 50 μm **(C-D)** Scanning electron microscopy (SEM) imaging reveals the three-dimensional structure of hMSC aggregates on PEG-PCL, as well as confirmation of direct contact between cells and the polymer surface.

In order to confidently confirm that the observed changes in hMSC behavior were not isolated to only one sample from a commercial source, hMSCs harvested from four patients at Vanderbilt University Medical Center were cultured atop PEG-PCL substrates and compared against TCPS. Figure 4.4 reveals that all four patient samples exhibited significant increases in *ITGA2* expression relative to TCPS, and two of the four samples significantly increased *PECAM* expression on PEG-PCL. Furthermore, three of the four patient samples showed a significant decrease in *Tie2* expression, and only one patient sample demonstrated a significant increase for *Nanog* and *SOX2* (**Figure 4.4**). At the protein level, a heterogeneous expression of αSMA, NG2, and PECAM was observed for patient cells on TCPS, according to immunofluorescent staining which shows differing degrees of positive cell numbers for each
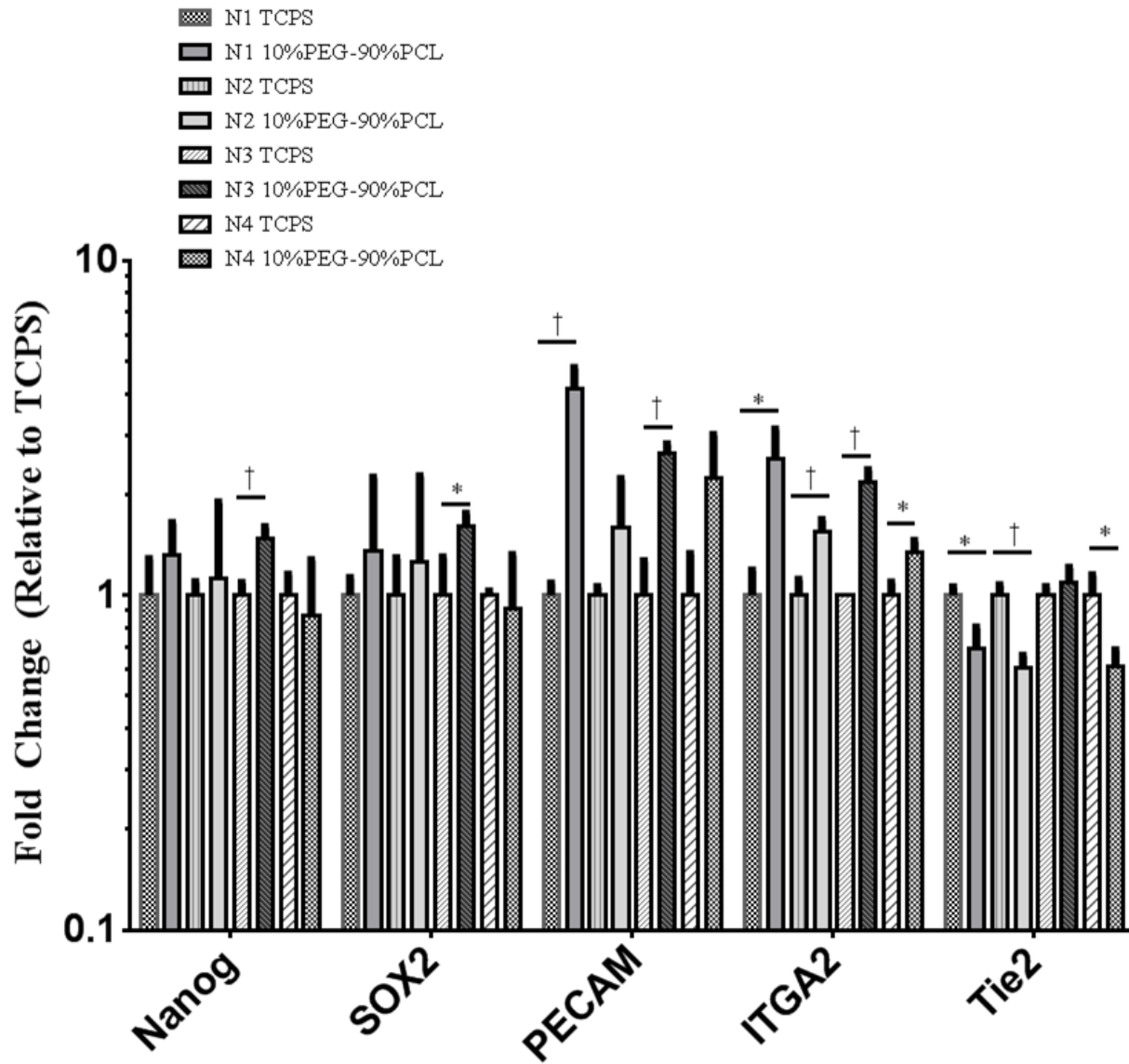
**Figure 4.4:** qRT-PCR of patient hMSCs on PEG-PCL following three-day culture. The expression of genes-of-interest were measured on TCPS and PEG-PCL for four patient hMSC samples from Vanderbilt University Medical Center. One of four samples exhibited a significant increase in *NANOG* and *SOX2* expression on PEG-PCL; two of four samples showed a significant increase in *PECAM* whereas all four samples were significantly increased for *ITGA2* on PEG-PCL; and three of the four significantly decreased *TIE2* expression on PEG-PCL versus TCPS. * $p < 0.05$ and † $p < 0.01$ versus TCPS.
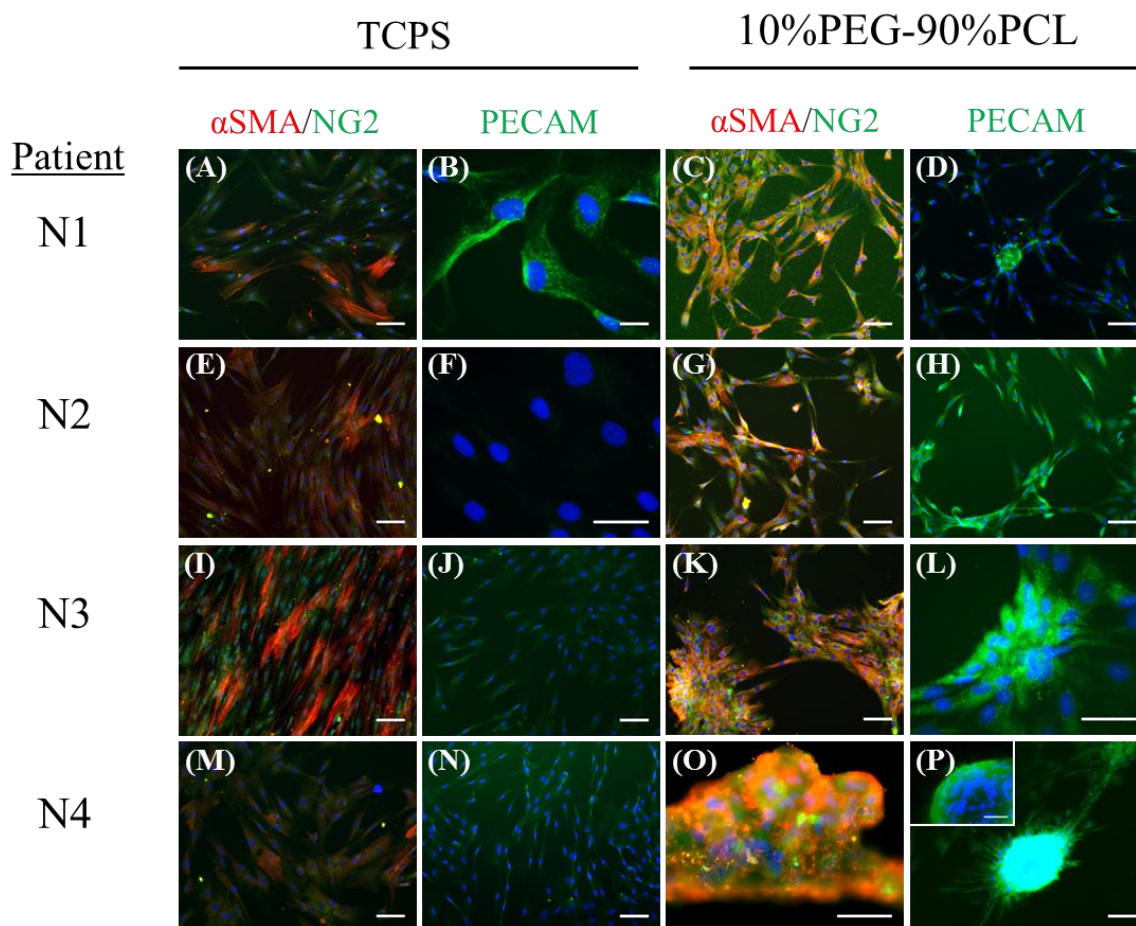
**Figure 4.5:** Immunofluorescent staining for pericyte markers of all four patient samples on TCPS and PEG-PCL after three-day culture. On TCPS, variable levels of expression for αSMA, NG2, and PECAM were observed for the patient samples. Regardless of the expression profile, however, patient hMSCs on PEG-PCL formed tube-like structures (**G, H**), aggregates (**K, L, O, P**), or a mixture of the two (**C, D**), and were positive for all three markers. Unless noted, scale bars = 100 μm; (**F, L, O** and **P insert**) scale bars = 50 μm.

marker (**Figure 4.5**). Interestingly, despite this variability, hMSCs cultured on PEG-PCL all showed positivity for the three markers, forming aggregates rich in αSMA or PECAM, or tube-like structures that stained positive for PECAM. The observed heterogeneity between hMSC samples stimulated a question of the fundamental hMSC transcriptome. To address this, the four patient samples, along with Lonza hMSCs, were examined for the expression of several markers, including pericyte, hMSC, and endothelial positive and negative markers (**Figure 4.6**). On both TCPS and PEG-PCL, hMSCs from all five sources were positive for the pericyte markers *NG2*, *PDGFRβ*, and *CD146*, and negative for the endothelial
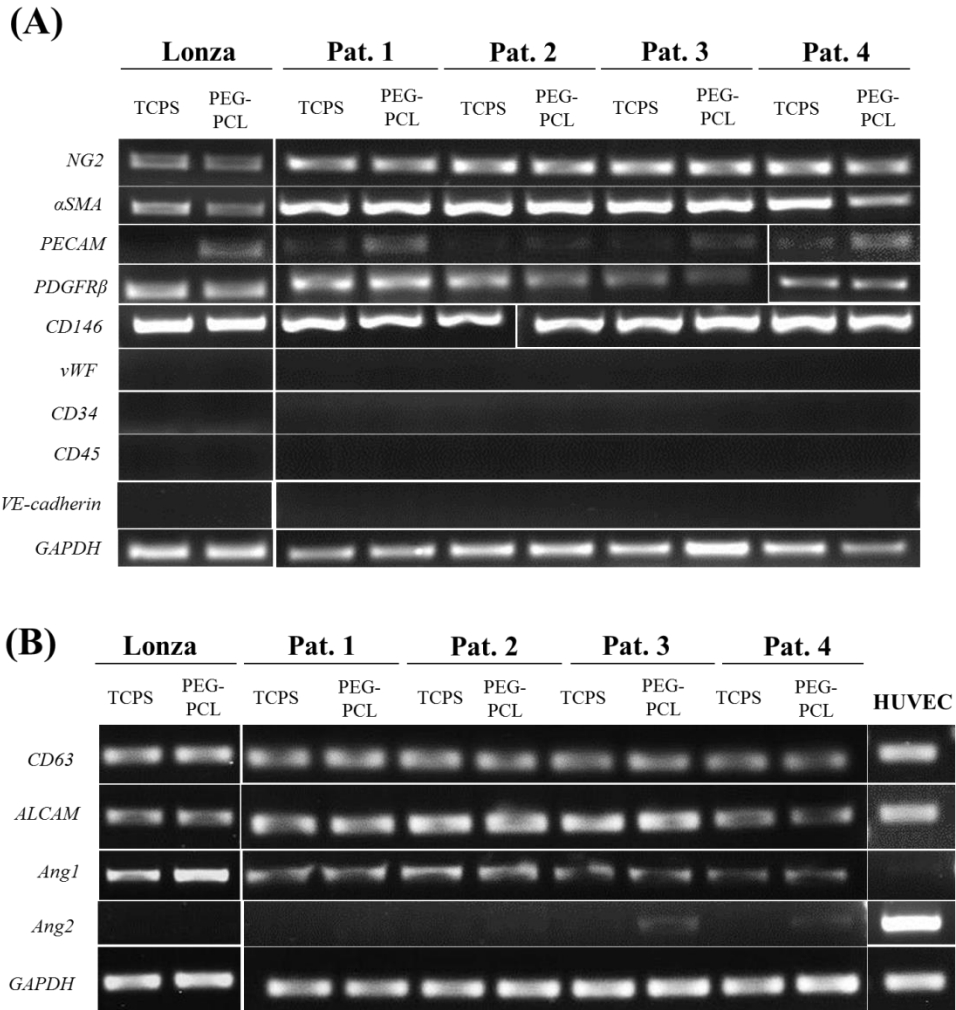
**Figure 4.6:** cPCR data for gene-level expression profiling of Lonza and patient hMSCs following three-day culture. **(A)** All hMSCs were positive for the pericyte markers *NG2*, *SMA*, *PDGFRβ*, and *CD146,* and negative for the endothelial marker *vWF*, the hematopoietic marker *CD34*, and the leukocyte marker *CD45*, regardless of culture substrate. **(B)** Furthermore, all cells were positive for the naïve hMSC markers *CD63* and *ALCAM*, as well as the angiogenic factor, *Ang1*, regardless of culture substrate. However, *Ang2* expression was detectable for only two of the patient hMSCs cultured on PEG-PCL.

markers *vWF* and *CD34*, as well as the leukocyte marker, *CD45* (**Figure 4.6A**). Interestingly, *PECAM* expression appeared to be absent for the TCPS hMSCs from Lonza, but faint bands were observed for two of the patient samples (patient 1, patient 4; **Figure 4.6A**). However, all hMSC sources showed an increase in *PECAM* expression when cultured on PEG-PCL, verifying the trends observed for the quantitative RT-PCR. Furthermore, all five hMSC samples maintained expression of the hMSC markers *CD63*, and *ALCAM*, and the angiogenic factor, *Ang1*, with two patient samples exhibiting detectable *Ang2* expression on PEG-PCL, but not TCPS (**Figure 4.6B**). Since the same trends were observed for hMSCs

from commercial and patient sources, and Lonza hMSCs did not demonstrate *PECAM* expression on TCPS (hMSCs are considered to be negative for PECAM), the remainder of experiments were performed solely with Lonza cells.

To this point, all experiments had been conducted following three day *in vitro* culture. To evaluate the ability to scale up the experiment into a larger format, as would be necessary for clinically-translatable applications, 10 cm diameter, Pyrex Petri dishes were spin-coated with PEG-PCL, and hMSCs were cultured for one week before end point experiments. TCPS control refers to tissue culture-treated T75 flasks for this portion of the work. Using the large-scale format, a similar gene-level expression profile was observed for hMSCs (**Figure 4.7A**), including significant upregulation of *PECAM* and *ITGA2*. In the one-week cultures, *CD63* was significantly increased while *ALCAM* was significantly down-regulated, suggesting that an undifferentiated phenotype was effectively maintained on PEG-PCL since *ALCAM* plays a role in hMSC osteogenic differentiation[146]. To this end, the protein-level expression of Nanog was upregulated on PEG-PCL, along with ITGA2, as compared to TCPS, indicated by Western blot data (**Figure 4.7B**). Because qRT-PCR and Western blot report the average expression
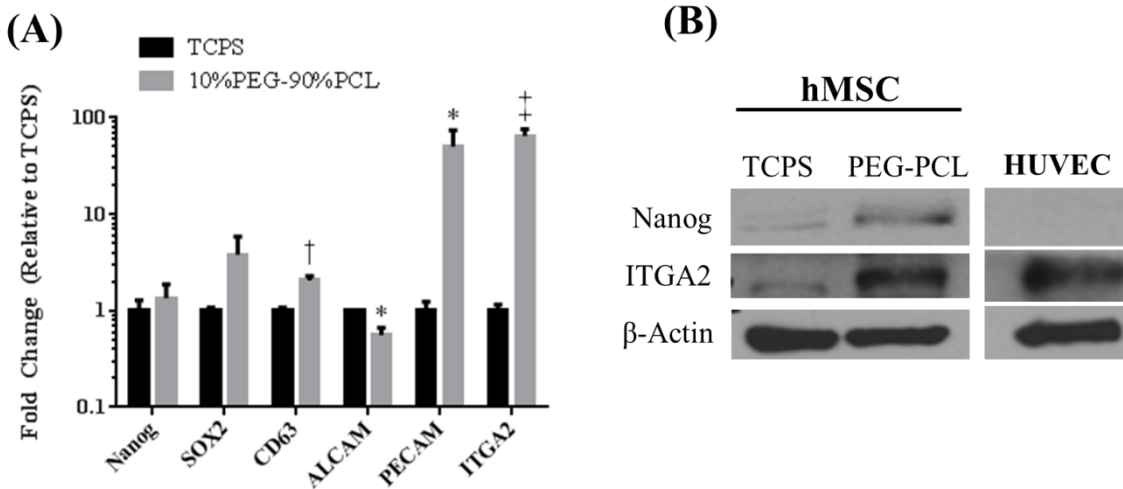


**Figure 4.7:** Characterization of gene- and protein-level expression profile for Lonza hMSCs cultured on large-scale PEG-PCL substrates for one week. **(A)** qRT-PCR demonstrates a significant increase in *CD63*, *PECAM*, and *ITGA2* with a concurrent decrease in *ALCAM*. **(B)** At the protein level, Nanog and ITGA2 expression were increased on PEG-PCL, as compared to TCPS. * $p < 0.05$ and † $p < 0.01$ versus TCPS.

of a given gene or protein within a population, flow cytometry (FCM) was also conducted to evaluate the population characteristics and relative expression levels for certain proteins-of-interest. The expression of PECAM (**Figure 4.8A**) and ITGA (**Figure 4.8B**) was higher for hMSCs cultured on PEG-PCL, as compared to TCPS, confirming the qRT-PCR and Western blot data.
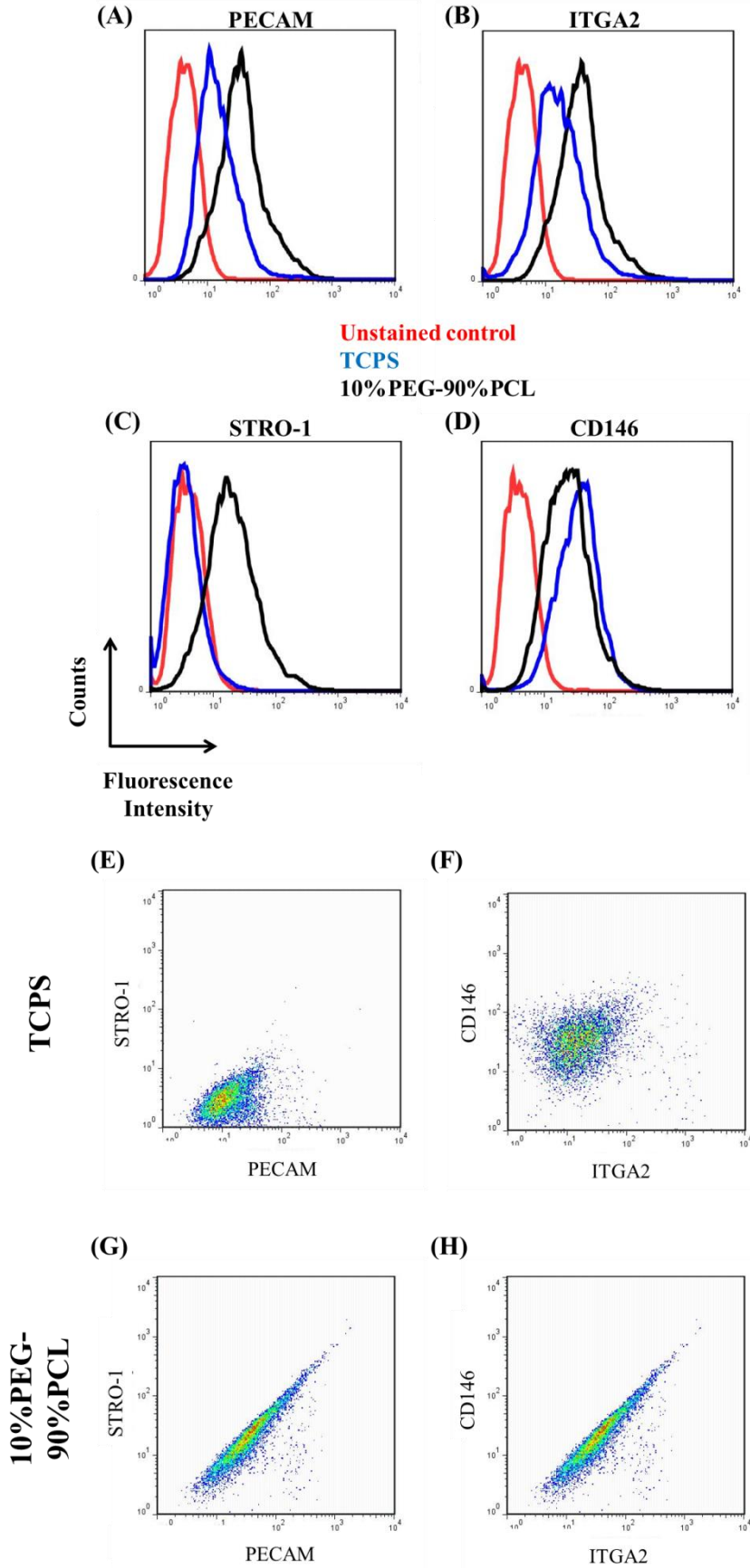
**Figure 4.8:** Flow cytometry of one-week hMSC cultures: **(A)** PECAM and **(B)** ITGA2 expression were stronger for PEG-PCL hMSCs (black lines), as compared to TCPS (blue lines). **(C)** STRO-1 expression was undetectable for TCPS hMSCs but was strong for PEG-PCL. **(D)** In contrast, CD146 expression was stronger for TCPS hMSCs than PEG-PCL. When the expression levels were correlated, TCPS hMSCs demonstrated no correlation for STRO-1 and PECAM **(E)** or CD146 and ITGA2 **(F)**, but PEG-PCL hMSCs showed strong linear correlations for STRO-1 and PECAM **(G)** as well as CD146 and ITGA2 **(F)**.

Strikingly, expression of STRO-1 was activated in hMSCs cultured on PEG-PCL, but was absent for hMSCs on TCPS (**Figure 4.8C**). CD146, a selection marker for pericytes and hMSCs, showed slightly stronger expression for hMSCs on TCPS, as compared to PEG-PCL, suggesting that STRO-1 and CD146, two markers of naïve hMSCs, are not mutually inclusive (**Figure 4.8D**). STRO-1 has been shown to decrease during *in vitro* culture as hMSCs represent, to a lessening degree, their original *in vivo* phenotype; however, in this experiment, CD146 remained strongly expressed for TCPS during *ex vivo* culture and was down-regulated on PEG-PCL, while STRO-1 was re-activated, suggesting that the binary on/off for CD146 might be difficult to interpret. When the fluorescence intensities of double-stained hMSCs were plotted against one another, a linear correlation in expression intensity was observed for PEG-PCL hMSCs (**Figure 4.8G,H**), but not for TCPS (**Figure 4.8E,F**). Because TCPS hMSCs were STRO-1⁻, there was no possibility for correlation to PECAM expression (**Figure 4.8E**); however, PEG-PCL hMSCs showed a tight linear correlation for the two markers (**Figure 4.8G**). Furthermore, although TCPS hMSCs expressed stronger signal for CD146, correlation with ITGA2 was not observed (**Figure 4.8F**) whereas PEG-PCL hMSCs again demonstrated a linear correlation for these markers (**Figure 4.8H**). Although the significance of these correlations is difficult to determine, in future experiments (described in Conclusions), RNA interference of ITGA2 and PECAM will indicate if there is a functional relationship within between these proteins.

*Effect of PEG-PCL hMSCs on HUVECs In Vitro*

As discussed above, hMSCs share inherent similarities with pericytes, an instrumental cell type in the development and maintenance of vasculature. Because an increase in *PECAM* and *ITGA2* has been thematic throughout this Chapter, the influence of PEG-PCL hMSCs on a model EC source, human umbilical vein endothelial cells (HUVECs), was next investigated. Despite the fact that angiogenesis/vasculogenesis is an extremely intricate process that involves countless regulatory factors, cell types, and cross-talk[165], focus was initially placed on the expression of angiopoietin-1 (*Ang1*) and *Ang2* due to changes of their role in the pericyte-EC relationship, as well as the consistent decrease in *Tie2* expression that was observed for Lonza hMSCs and all patient samples (**Figures 4.2C and 4.4**). As an indicator of the heavily-influential pathway of vascular endothelial growth factor (VEGF), *VEGFA* was also included in these measurements.

The gene-level angiogenic expression profile of PEG-PCL hMSCs versus cells on TCPS revealed a significant upregulation of *Ang1* with no significant change in *VEGFA* (**Figure 4.9A,B**). Interestingly, a weak band for *Ang2* was detected by conventional PCR for hMSCs on PEG-PCL, but no signal was detected for TCPS hMSCs (**Figure 4.9A**). When treated with conditioned media from either TCPS hMSCs or PEG-PCL hMSCs, significantly more HUVECs were observed to migrate through a
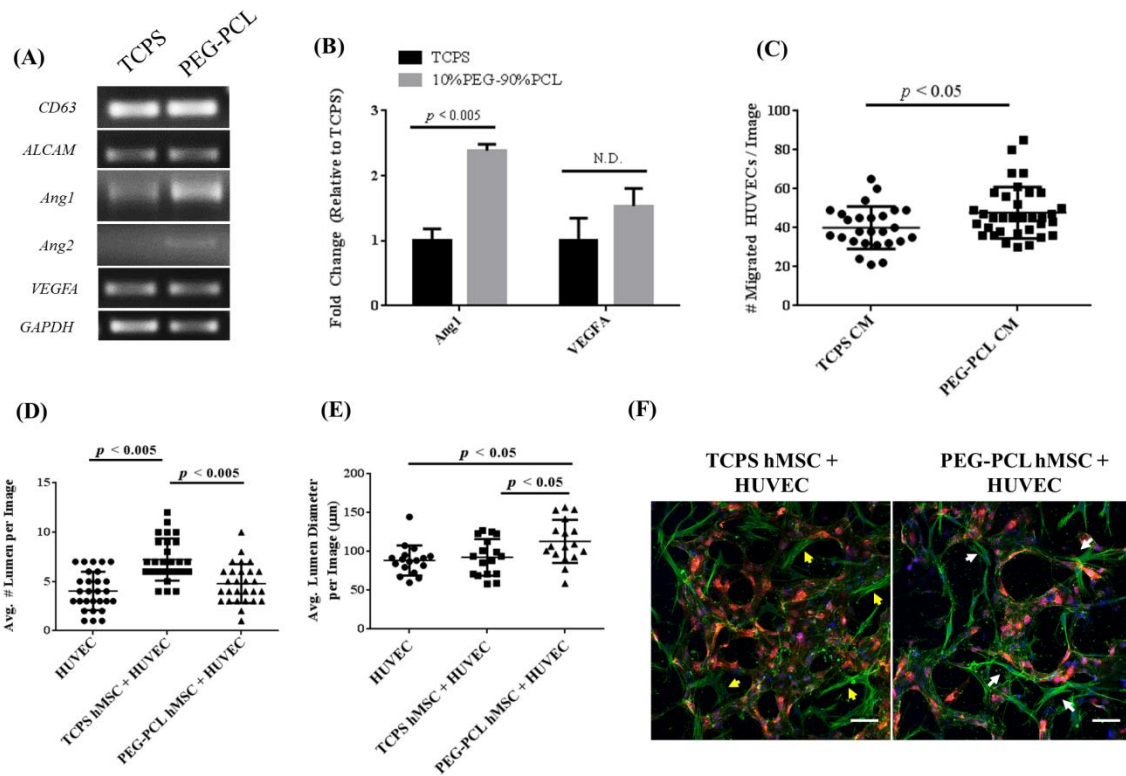
**Figure 4.9:** PEG-PCL hMSC influence on HUVECs *in vitro*. **(A)** Conventional PCR of one-week hMSC cultures demonstrates activation of *Ang2* expression on PEG-PCL, and **(B)** qRT-PCR confirms a significant increase in *Ang1*, but not *VEGFA*, expression on PEG-PCL as compared to TCPS. **(C)** When HUVECs were exposed to conditioned media from PEG-PCL or TCPS hMSCs in a transwell migration assay, significantly more HUVECs migrated through the chamber after four hours in culture. Finally, when HUVECs were co-cultured with hMSCs from TCPS or PEG-PCL in a three-dimensional collagen gel, PEG-PCL hMSCs stimulated the formation of significantly less **(D)**, but larger **(E)**, HUVEC lumen, as compared to the TCPS hMSCs. **(F)** When visualized by confocal microscopy, TCPS hMSCs tended to localize to the inside of HUVEC lumen (yellow arrowheads) whereas PEG-PCL hMSCs remained on the abluminal side (white arrowheads), similar to the *in vivo* localization and functionality of pericytes. Scale bars = 100 μm  N.D. – No difference

commercial transwell assay after four hours (**Figure 4.9C**). These data are in agreement with the literature as Ang1 is known to promote the proliferation and migration of ECs *in vitro*[110, 166]. A co-culture model was next used to evaluate juxtacrine effects and physical interactions between the two cell types (**Figure 4.9D-F**). hMSCs were cultured on TCPS or PEG-PCL for three days, removed, and re-seeded with red fluorescent HUVECs (2:1 HUVEC:hMSC) in a three-dimensional (3D) type-I collagen gel, similar to previous protocols from our lab[165] as well as others[167]. When co-cultured for 48 hours, HUVECs co-cultured with TCPS hMSCs exhibited significantly more lumens in each 10x field of view than did HUVECs alone or those with PEG-PCL hMSCs (**Figure 4.9D**); however, the average size of the lumen in each field of view were significantly smaller than those resulting from PEG-PCL hMSC co-

culture (**Figure 4.9E**). When the co-cultures were fixed, stained with AlexaFluor488-phalloidin, and imaged under a confocal microscope, the localization of the two types of hMSCs appeared to be different (**Figure 4.9F**). TCPS hMSCs appeared to predominantly localize within the HUVEC lumen (yellow arrowheads) whereas the PEG-PCL hMSCs localized at the abluminal side of the HUVECs, which would be observed *in vivo* for bona fide pericytes[101]. Taken together, these data indicate that PEG-PCL hMSCs possess a greater ability to promote HUVEC migration in monoculture through paracrine signaling, as well as stabilization of larger lumen in a 3D model, likely through and Ang1/Ang2/Tie2 mechanism.

The increased *in vitro* activities of HUVECs in contact with PEG-PCL hMSCs or in the presence of hMSC-conditioned media prompted the question of how hMSC behavior/phenotype would be altered in a porous, 3D scaffold fabricated from 10%PEG-90%PCL, and if it could promote vascularization *in vivo*. Using a well-established salt-leaching method[165], uncrosslinked PEG-PCL scaffolds were fabricated
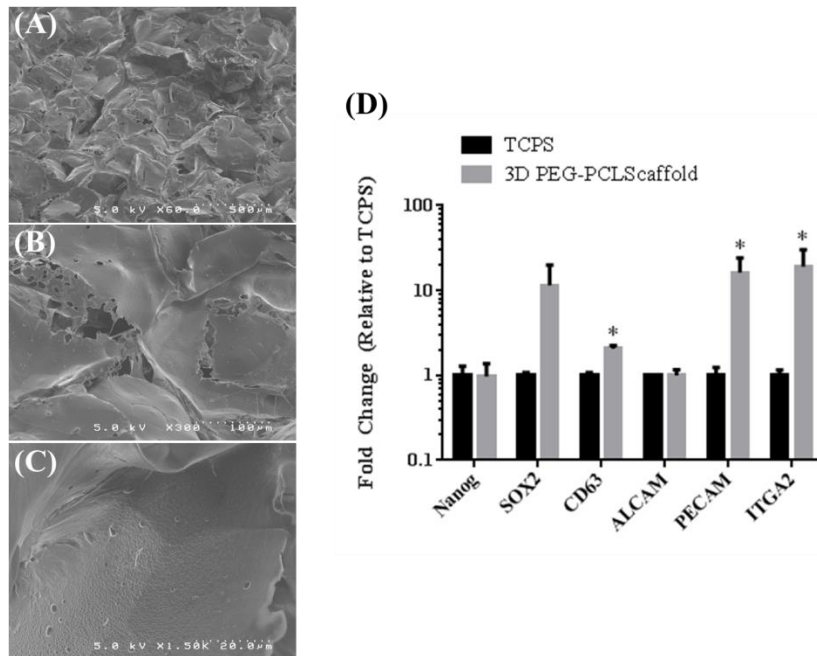


**Figure 4.10:** Three-dimensional PEG-PCL scaffolds stimulate the same gene-level response as two-dimensional culture substrates. **(A-C)** SEM imaging shows macro- and micro-scale pores formed in the PEG-PCL scaffold, including surface pores **(C)**. **(D)** qRT-PCR reveals a similar gene-level expression for 3D scaffolds as 2D culture substrates, including significant increases in *CD63, PECAM,* and *ITGA2* for PEG-PCL hMSCs, versus TCPS. * $p < 0.05$.

and tested *in vitro* against TCPS control. As seen in Figure 4.10, SEM images of 3D scaffold cross-sections reveal a relatively uniform morphology of large holes (A), and regions of degradation that cause smaller holes (B), likely due to the salt-leaching process during which the PEG-PCL scaffolds are exposed to water for three days, resulting in hydrolytic degradation of the PEG chains. Interestingly, pores were still present in the 3D scaffold, and within the range of those found in the two-dimensional, spin-coated substrates from Specific Aim #2 (~0.5 – 2 μm, **Figure 4.10C**). When gene expression was

measured, a profile similar to that of hMSCs on PEG-PCL in 2D was observed, including significant increases in *CD63, PECAM*, and *ITGA2,* as well as an insignificant increase in *Ang1* (**Figure 4.10D**).

*PEG-PCL/hMSC Scaffolds Promote Vascularization In Vivo*

To this point, PEG-PCL has been shown to stimulate a pericyte-like phenotype in hMSCs, both in 2D and 3D formats, which can stimulate increased EC migration and promote tube stabilization. The next step was to evaluate how hMSC-loaded, 3D scaffolds of PEG-PCL would perform when implanted *in vivo*. For the implants, 100%PCL scaffolds were fabricated with the same method and used as a control. To ensure that the scaffold itself wasn't exerting a drastic effect on vascularization, or to simply remove the baseline activity of the host tissue, scaffolds of both types of polymers without cells ("blank") were also included. Using optical coherence tomography (OCT), animals were observed for the formation of vasculature at 3, 7, 14, and 21 days post-implantation. As seen in Figure 4.11, all scaffolds exhibited some degree of vascularization, but this seemed to regress in in PCL scaffolds by day 7, whereas interconnected vascular networks were evident in PEG-PCL scaffolds. By days 14 and 21, both of the hMSC-loaded scaffolds (i.e. 100%PCL and 10%PEG-90%PCL) appeared to have enhanced vascularization relative to the blank scaffold controls. Of note, the image panel shown in Figure 4.11 is comprised of images from the same animal over time, as opposed to representative images for each time point, allowing for clearer interpretation of the data set.

When the OCT images were quantified, several points became clear (**Figure 4.12**). First, the hMSC-loaded PEG-PCL scaffolds stimulated significantly more vessel density than either of the blank scaffolds, but this was not the case for PCL-loaded scaffolds (**Figure 4.12A**). Furthermore, PEG-PCL + hMSCs maintained the highest degree of vessel density over the three week period, albeit without quite reaching statistical significance relative to hMSC-loaded PCL scaffolds ($p = 0.05$ on days 14 and 21 versus PCL + hMSCs, **Figure 4.12A**). However, when the values for all time points for *each* scaffold type were compared, PEG-PCL + hMSCs demonstrated a significantly higher vessel density than PCL + hMSCs or the unloaded PCL blank (**Figure 4.12B**). Furthermore, when only the hMSC-loaded scaffolds were compared, the PEG-PCL-loaded scaffolds demonstrated significance at days 14 and 21 post-implantation (**Figure 4.12C**). These data suggest that the phenotype of PEG-PCL hMSCs demonstrate increased vascularization in the first three days, and are able to maintain this effect over three weeks. When compared with hMSCs on a more classical scaffold, such as 100%PCL, the resulting vascularity was significantly higher at the later time points (**Figure 4.12C**).
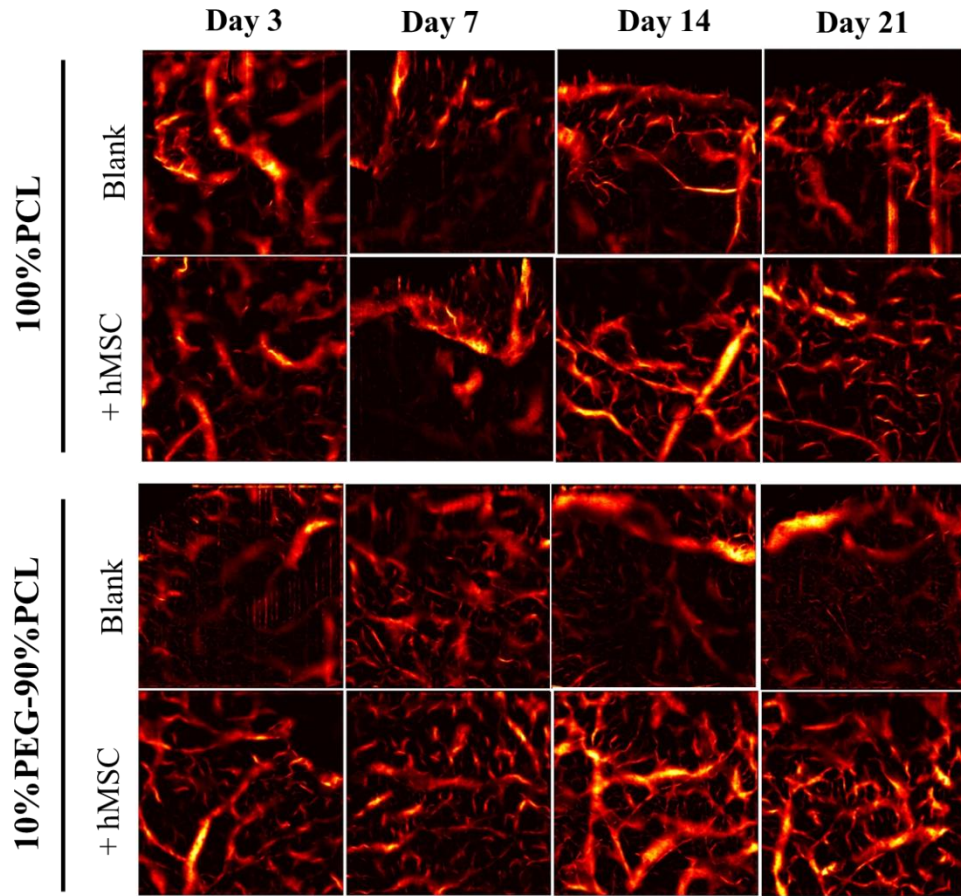
**Figure 4.11:** Optical coherence tomography (OCT) imaging demonstrates time-dependent changes in vasculature *in vivo* over three weeks in the same animal (mouse #1).
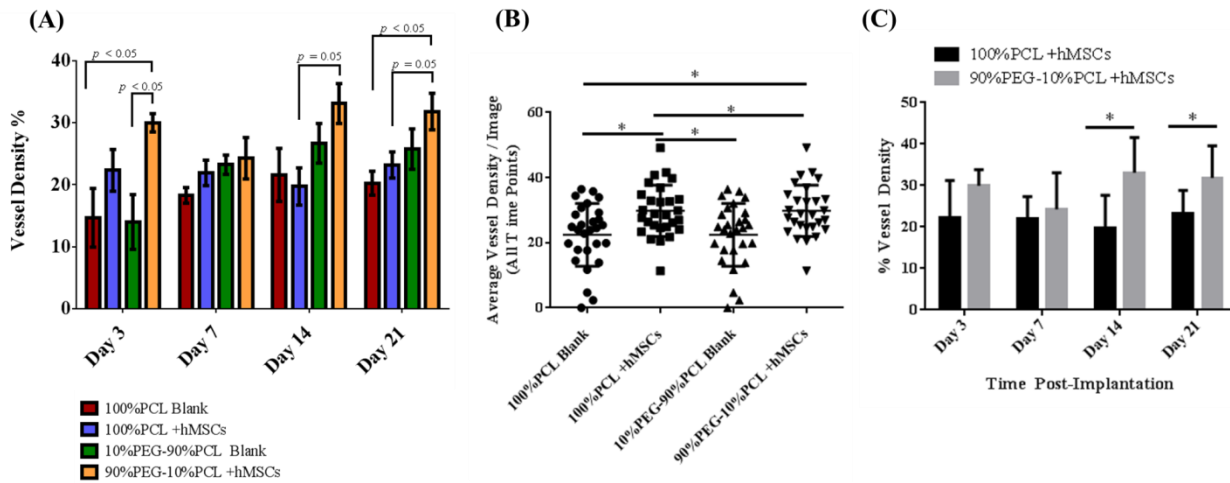


**Figure 4.12:** Quantification of *in vivo* OCT data. **(A)** Quantification of all images over time for seven animals shows a significantly higher vessel density for PEG-PCL scaffolds loaded with hMSCs relative to blank scaffolds at day 3, but is not significant relative to PCL-loaded scaffolds at days 14 and 21 post-implantation. **(B)** When vessel density for each scaffold type was compiled, regardless of time point, hMSC-loaded PEG-PCL scaffolds were significantly higher than blank or hMSC-loaded PCL scaffolds. **(C)** When only the hMSC-loaded scaffolds were compared over time, a significantly higher vessel density was measured for PEG-PCL scaffolds as compared to PCL. $* p < 0.05$ as indicated by the lines or between groups.

*Hypothesis and Determination of Structure-Function Relationships*

The next step was to identify the mechanism by which the cell-biomaterial surface was stimulating the observed increase in *PECAM*, *ITGA2*, *Ang1*, *Ang2*, and Nanog expression. Because the adsorption of serum proteins to the surface of any culture material is required for cells to be able to attach, the influence of serum concentration was evaluated. hMSCs are known to be sensitive to FBS concentration as complete serum deprivation selects for Oct4A-expressing progenitor cells with high angiogenic potential[168-170]. After overnight seeding, hMSCs on both TCPS and PEG-PCL assumed a spindle-shaped morphology for all FBS concentrations (**Figure 4.13A**). On TCPS the cells appeared to spread more as the FBS concentration increased, but hMSCs on PEG-PCL maintained an elongated shape with high aspect ratio, despite FBS content. At the gene level after three days of culture, *PECAM* expression was increased on PEG-PCL for all FBS concentrations, with a similar trend for *ITGA2* (**Figure 4.13B**). Interestingly, in the 2% FBS condition, *Nanog* and *SOX2* expression were undetectable on TCPS, but both genes were observed on PEG-PCL. As the amount of FBS increased, the expression of the two stemness genes increased on TCPS, and the observed variation between TCPS and PEG-PCL
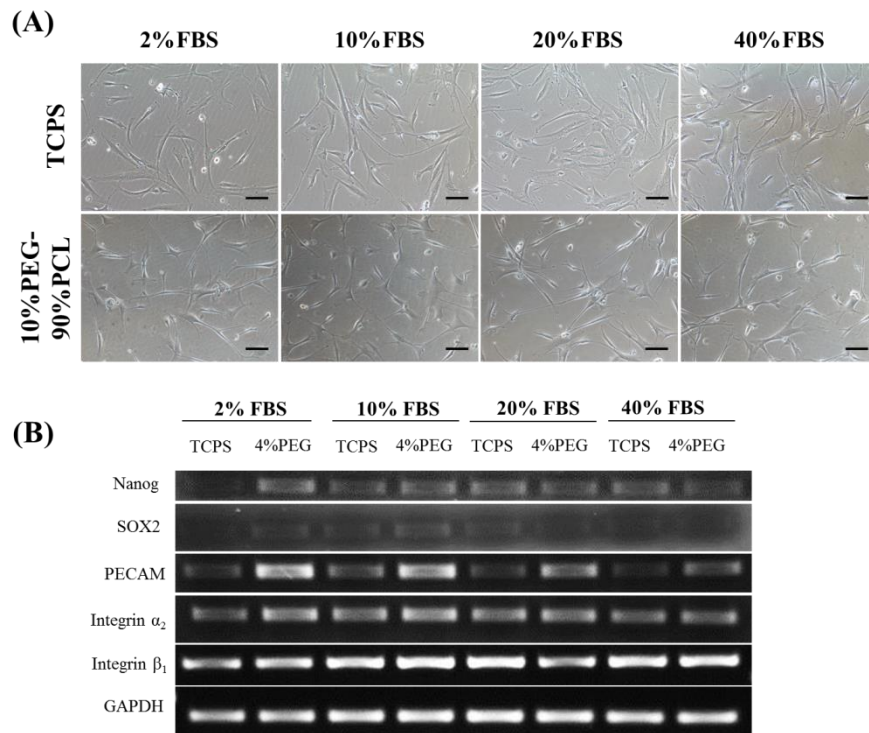


**Figure 4.13:** Serum concentration has negligible effects on PEG-PCL-mediated changes to hMSC behavior. **(A)** After overnight culture, hMSCs become increasingly more spread on TCPS with higher FBS content, abut remain elongated on PEG-PCL. **(B)** After three days, conventional PCR demonstrates that *NANOG* and *SOX2* are most effectively enhanced in 2% FBS condition, and the PEG-PCL effect diminishes as serum concentration increases. Scale bars = 100 μm

became less obvious. These data indicated that increases in *PECAM*, *ITGA2,* and *Nanog* had some influence from the serum, albeit the effect was not fully serum-dependent since it occurred on PEG-PCL for all serum concentrations.

Therefore, we sought to identify how the biomaterial culture substrate was interacting with the culture media in order to understand if a simple alteration of protein adsorption was responsible for the altered hMSC phenotype on PEG-PCL. When the fraction of FBS adsorbed from complete media to the material surfaces was quantified, a striking increase in protein was measured on the PEG-PCL surface, compared to TCPS (**Figure 4.14A**). However, aside from the quantity of protein adsorbed, there was not an obvious, visual difference between the adsorption profiles for the two surfaces, as shown by similar bands that appeared when separated on an agarose gel and stained with colloidal Coomassie (**Figure 4.14B**). The samples from the two groups were analyzed by LC-MS/MS to identify the types and relative abundance of proteins present. Shown in Figure 4.14C are the five most abundant proteins that were measured. Not surprisingly, serum albumin had the greatest presence, followed by serotransferrin, but the most interesting protein identified from this screen was alpha-2-HS-glycoprotein, also known as fetuin-A, which exhibited nearly 3x more signal from the PEG-PCL samples, as compared to TCPS ($p < 0.0001$). Fetuin-A is known to antagonize the bone morphogenetic protein (BMP)/transforming growth factor (TGF)-β superfamily by acting as a TGFβ receptor mimic[171], or binding TGFβ/cytokines[172], which has been shown to block osteogenesis both *in vitro*[171] and *in vivo*[172]. These two major pathways act parallel to one another but antagonistically, and their tightly-orchestrated interplay is of great importance in early development, tissue maintenance, and disease[173]. We therefore measured the gene expression of a TGFβ target gene, plasminogen activator inhibitor-1 (*PAI1*)[174], as well as the downstream BMP genes, DNA-binding protein inhibitors 1 (*ID1*) and 2 (*ID2*)[175]. The role of these genes in hMSCs in unclear and underexplored[176], with contradictory reports of TGFβ/BMP effects on hMSCs in the literature that confound interpretations[177-179]. When measured by qRT-PCR, *ID2* was significantly increased on PEG-PCL, as compared TCPS, for three-day cultures (**Figure 4.14D**), as well as one-week cultures on large-format and 3D scaffolds (**Figure. 4.14E**). *PAI1* significantly decreased on three-day and one-week cultures, but not for 3D scaffolds. Finally, in three-day cultures, *ID1* expression did not change, but large-format and 3D scaffolds demonstrated significantly higher *ID1* expression (**Figure 4.14E**). Expression of TGFβ receptor I (*TGFBR1)* did not change for one-week cultures (**Figure 4.14E**). These data therefore suggested a role for fetuin-A in regulating hMSC function by altering the bias of the TGFβ/BMP pathways.

**(A)**



**(B)**



**(C)**

| Identified Proteins | Accession Number | Molecular Weight | Fisher's Exact Test (P-Value) | Fold Change Relative to TCPS (Approximate) |
|---|---|---|---|---|
| Serum albumin | sp\|P02769\|ALBU_BOVIN | 69 kDa | 95% (0.00096) | ~ 2x |
| Serotransferrin | sp\|Q29443\|TRFE_BOVIN | 78 kDa | 0% (0.20) | ~ 2x |
| Alpha-2-HS-glycoprotein | sp\|P12763\|FETUA_BOVIN | 38 kDa | 95% (< 0.00010) | ~ 3x |
| Alpha-2-macroglobulin | sp\|Q7SIH1\|A2MG_BOVIN | 168 kDa | 0% (0.47) | ~ 1.5x |
| Alpha-1-antiproteinase | sp\|P34955\|A1AT_BOVIN | 46 kDa | 95% (0.00088) | ~ 2x |

**(D)**



**(E)**



**Figure 4.14:** Protein adsorption, identification, and effect on PEG-PCL. **(A)** Significantly more protein adsorbs to PEG-PCL as compared to TCPS, but **(B)** no obvious difference in adsorbed composition was noticed when separated on a gel. **(C)** However, protein identification with LC-MS/MS revealed several candidate proteins that were significantly higher on PEG-PCL than TCPS, including the TGF-β antagonist, fetuin-A. **(D)** Three-day and **(E)** one-week cultures show increased expression of *ID2* with a concurrent decrease in *PAI1*, two downstream TGF-β target genes with competing activities, when cultured on PEG-PCL. These data suggest that the TGF-β pathway is inhibited during culture on PEG-PCL. * $p < 0.05$ and † $p < 0.01$ versus TCPS.

In order to test the role of fetuin-A in the PEG-PCL system, a chemically-defined media (CDM) that does not contain fetuin-A was purchased from Lonza to evaluate if colony formation and alterations

to gene expression would be abrogated. In the presence of either αMEM or CDM, hMSCs spread normally on TCPS and formed colonies on PEG-PCL (**Figure 4.15A**). At the gene level, *Nanog, SOX2,* and *PECAM* were expressed at a basal level on TCPS for αMEM, and these levels appeared to increase on PEG-PCL (**Figure 4.15B**). In stark contrast, however, all detectable expression of *Nanog* and *SOX2* was lost on TCPS in the presence of CDM, but was reinstated when cultured on PEG-PCL. Because the role of fetuin-A was hypothesized to drive the observed increase in stemness for hMSCs on PEG-PCL, and CDM does not contain fetuin but stimulated the same behavior, it became evident that fetuin-A was not the critical regulator. In order to test the ability of the cell-biomaterial interface to drive intracellular alterations, the surface of TCPS or PEG-PCL was pre-coated with either type-I collagen or fibronectin before hMSC culture (**Figure 4.15C-D**). hMSC spreading was slightly reduced on TCPS when pre-
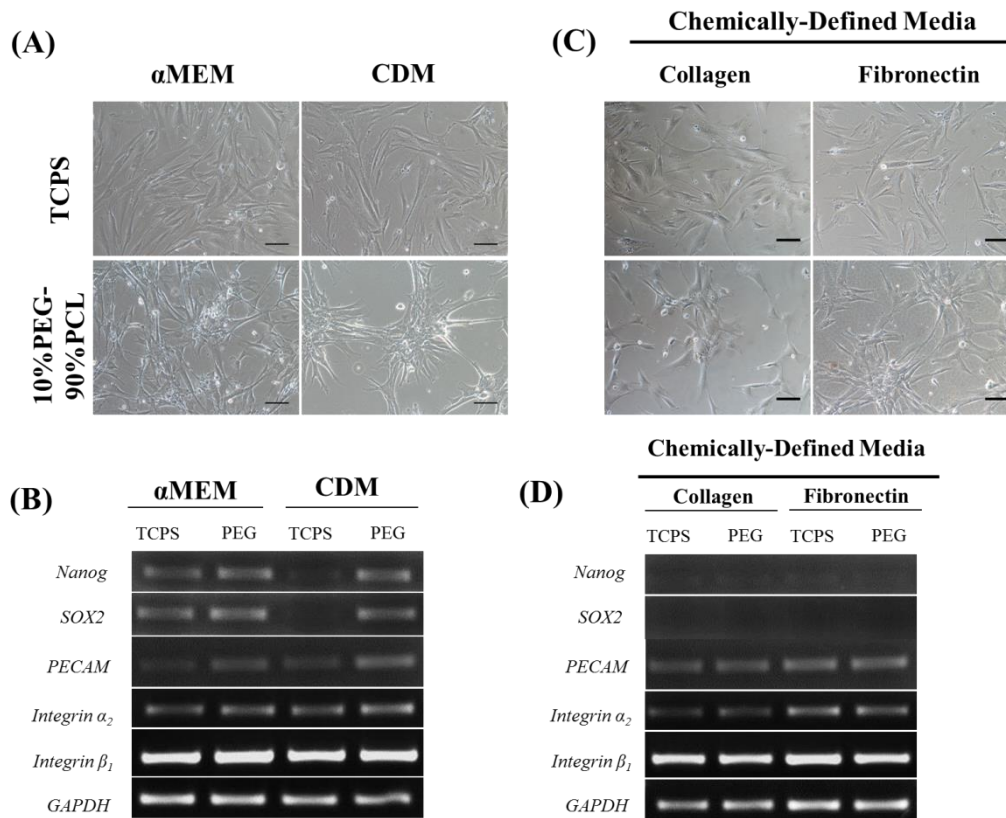


**Figure 4.15:** Chemically-defined media (CDM) without fetuin-A stimulates the same response as normal, complete media, but hMSCs must be in direct contact with the PEG-PCL surface to stimulate this behavior. **(A)** After overnight seeding, hMSCs on PEG-PCL form aggregates in both αMEM and CDM, but form a spread monolayer TCPS. **(B)** Conventional PCR demonstrates a lack of *NANOG* or *SOX2* expression for hMSCs on TCPS in CDM, but both stemness genes were detected on PEG-PCL. **(C)** When TCPS or PEG-PCL surfaces were pre-coated with collagen or fibronectin, hMSCs still formed aggregates on PEG-PCL albeit with better cell attachment over the entirety of the material surface. However, when gene expression was measured by conventional PCR, neither *NANOG* or *SOX2* were detected on pre-coated PEG-PCL surfaces. These data indicate the need for hMSCs to be in direct contact with the material surface for the observed increase in stemness gene expression to be activated. Scale bars = 100 μm.

coated with either collagen or fibronectin, and colonies still formed on PEG-PCL in the presence of either protein (**Figure 4.15C**). When the gene expression profile was measured, neither *Nanog* nor *SOX2* was detected for hMSCs on TCPS or PEG-PCL in either coating condition although *PECAM*, *ITGA2*, and *ITGB1* were all expressed (**Figure 4.15D**). Potentially, the observed effect of the coatings is due to a filling of the pore structure that is present at the PEG-PCL surface, but this question is to be addressed with ongoing experiments. Regardless, the data shown here verify that the cell-biomaterial interface is crucial for regulating the observed hMSC behavior because "masking" the PEG-PCL surface features by pre-coating with collagen or fibronectin blocked the expression of the two stemness genes.

**Conclusions**

In this Aim, the biological relevance hMSCs cultured on PEG-PCL substrates, as well as the structure-function relationship that regulates this behavior, was evaluated. Using patient hMSCs, the observed increases in *PECAM* and *ITGA2* at the gene-level, and PECAM, αSMA, and NG2 at the protein level, were first confirmed. Then, using a large-scale polymer format, one-week cultures were used to confirm scalability in terms of both culture size and time, as well as the pro-angiogenic effects of hMSCs on PEG-PCL when interacting with HUVECs *in vitro* or when implanted in a 3D scaffold *in vivo*. Finally, the observed events were shown to be independent of serum concentration and did not rely on the activity of the protein fetuin-A, which was proven with fetuin-free, chemically-defined media. Furthermore, by pre-coating the PEG-PCL surface, the need for direct interaction between the cells and the biomaterial interface was illustrated because the observed phenotype was lost.

Because hMSCs are considered to be phenotypically related to pericytes, the observed increase in stemness gene and protein expression might indicate a reversion back to a pericyte-like lineage that is lost in traditional culture conditions. Utilizing a systematic engineering approach in which expwerimental observations were used to develop hypotheses, followed by experiments that were designed to test these predictions, the phenotypic regulation of hMSCs as the biointerface was confirmed. Although several ongoing experiments remain, this work represents a fundamental step in (1) the understanding of hMSC behavior and potential for vascular applications; (2) outside-in regulation of stem cell biology by extracellular matrix cues; and (3) suggests an *in vitro* model for investigating the relationship between hMSCs and pericytes.

CHAPTER 5


Summary and Future Work


The doctoral dissertation described in this document has primarily focused on the regulation of human mesenchymal stem cell behavior through biochemical and environmental signals (Aim #1), and extracellular matrix (ECM)-derived cues (Aims #2 and #3). Using late passage hMSCs asa model for *in vivo* aging, Specific Aim #1 described the increased susceptibility of serially-expanded hMSCs to a harsh environment of carcinogenic hypoxia due to faulty redox and pro-survival mechanisms that prevent the cell from effectively protecting itself. The data collected in Aim #1 were used to construct a hypothesized model for the pathways driving the observed events, and culminated in a downregulation of p53-mediated cellular responses.

In Specific Aim #2, a library of copolymers based on poly($\epsilon$-caprolactone) (PCL), poly(ethylene glycol) (PEG), and carboxylated-PCL (cPCL) was developed and characterized for use as synthetic cell culture substrates. Using well-established material characterization techniques, the influence of each particular subunit was evaluated in terms of physicochemical, mechanical, and surface/biointerfacial properties. When aging hMSCs were cultured on the substrates, the intracellular redox levels were modulated, which correlated with proliferative capacity. Although the specific mechanisms driving the event remain unverified, it is thought that a the APE/Ref-1, p53, SESN1, SESN2 cascade might regulate intracellular redox in hMSCs. However, the expression of two key stemness genes, *Nanog* and *SOX2*, was significantly upregulated on one of the copolymers, 10%PEG-90%PCL, as compared to the tissue culture control. When a PCR array was used to identify potential mechanisms at the cell-biomaterial interface that were driving the observed increase, two genes-of-interest were shown to be significantly upregulated: *PECAM* and *ITGA2*. These data were verified by qRT-PCR and used as guidance for the third and final Aim of this project.

In Specific Aim #3, early passage hMSCs from a commercial source, as well as from four patients at Vanderbilt University Medical Center, were used to confirm the results measured with late passage hMSCs in Specific Aim #2. In recent years, the question of *in vivo* hMSC identity has been raised, especially in regards to a landmark paper by Crisan *et al* in 2008 which showed that pericytes (i.e. perivascular support cells, or mural cells) and hMSCs share inherent similarities[99]. Based on this idea, the fact that PECAM and integrin α2 (ITGA2) expression were significantly upregulated for hMSCs cultured on PEG-PCL substrates, and that these two proteins are readily found in vascular compartment, a

suggested phenotypic reversion for hMSCs back to pericytes became the topic of investigation for this Aim. Through a systematic approach, the biological relevance of the observed changes in hMSC behavior was shown to correlate with increased endothelial cell (EC) migration in response to hMSC conditioned media, as well as larger lumens that formed in three-dimensional (3D) co-culture, that is hypothesized to be dependent upon the increased expression of angiopoietin (Ang)-1 and Ang-2. When cultured in 3D, porous scaffolds fabricated from PEG-PCL, hMSCs assumed a similar phenotype to that which was observed in 2D, and *in vivo* implantation of hMSC-loaded scaffolds revealed an increase in vascularity, as determined by optical coherence tomography (OCT) imaging over a three week period. From the standpoint of material properties, the final step of the project focused to elucidate how the polymer surface structure was driving the observed intracellular events. First, hMSCs were cultured in a range of serum concentrations to determine if protein concentration, or adsorption profile, played a role. Although the different serum concentrations stimulated differing degrees of response, the overall gene expression profile was largely unaffected. Next, the fraction of serum proteins that adsorbed to the material surface was next quantified and characterized by mass spectrometry, and a specific protein-of-interest was identified: fetuin-A, an antagonist of the transforming growth factor (TGF)-β/bone morphogenetic protein (BMP) pathway. Using a chemically-defined culture media that does not contain fetuin-A, the effect of PEG-PCL on hMSCs was still observed, remarkably to a stronger degree than the complete culture media that had been used throughout the study. To verify that the interaction of hMSCs and the biomaterial is critical for driving the observed effects, copolymer culture substrates were finally pre-coated with either collagen or fibronectin, which were shown to abrogate the increase in *Nanog* and *SOX2*. This final experiment confirms the necessity for hMSCs to be in complete contact with PEG-PCL, and proves that the interfacial mechanism driving the observed increase is inherent to the copolymer surface and not due to secondary effects of the material properties.

As this project has progressed, several interesting points have arisen that warrant continued investigation. For example, the increased expression of PECAM and ITGA2 was observed throughout Aims #2 and #3, and might play a significant role in hMSC maintenance and self-renewal in this system. Using function-inhibiting antibodies and small hairpin RNA (shRNA) interference, the exact requirements for each of these proteins can be determined. Because both PECAM and ITGA2 are predominantly found in the vasculature, the functional relevance of their increased expression in hMSCs might reveal fundamental insights for the nature of hMSCs, as well as their pro-angiogenic abilities. Furthermore, in Aims #1 and #2, proliferation was shown to correlate with intracellular ROS levels, suggesting a dependent relationship between the two measurements. Because this correlation has never been reported in the literature for hMSCs, but was observed in two different systems within this dissertation project, it would be worthwhile to look more closely at how the regulation of ROS and

proliferation are related. Finally, the copolymer composition 10%PEG-90%PCL (5,000 Da molecular weight PEG block) was shown to effectively increase hMSC stemness more effectively that 0%PEG, 25%PEG, or the tissue culture control, but what about smaller increments of PEG percentage? And if the size of the PEG block is changed, how does that affect domain formation at the material surface, and how is hMSC behavior influenced as a result? These final questions are the focus of an ongoing project in the Sung laboratory, headed by medical science training program (MSTP) student, Daniel Balikov, and will be used to build upon the findings that I uncovered during my time as a graduate student.

In summary the project presented here represents an interdisciplinary engineering approach to fundamental stem cell biology with the overall aim of improving regenerative, hMSC-based therapies. The findings from this project add to an ongoing conversation in the literature regarding extracellular matrix-mediated manipulation of hMSC function and elegantly identify an outside-in signaling mechanism that drives alterations to intracellular behavior. The ongoing and future work related to this project will be used to elucidate fundamental cell-biomaterial interfacial mechanisms in a basic science setting that can be exploited for the design and production of next-generation tissue engineering scaffolds.

Appendix I – Antibody Information and Primer Sequences

Specific Aims #2 and #3

| Target | Host | Company | Dilution Factors | |
| --- | --- | --- | --- | --- |
| | | | IF, FCM | WB |
| αSMA | Mouse | Sigma Aldrich | 1 : 250 | N/A |
| PECAM | Rabbit | Santa Cruz Biotech | 1 : 50 | N/A |
| ITGA2 | Rabbit | Santa Cruz Biotech | 1 : 50 | 1 : 200 |
| STRO-1 | Mouse | Santa Cruz Biotech | 1 : 50 | N/A |
| CD146 | Mouse | BD Pharmingen | 1 : 100 | N/A |
| NG2 | Rabbit | Santa Cruz Biotech | 1 : 50 | N/A |
| Nanog | Rabbit | Cell Signaling | N/A | 1 : 2000 |
| β-Actin | Rabbit | Cell Signaling | N/A | 1 : 2000 |

| Gene Name | Accession # | Forward 5' - 3' | Reverse 5' - 3' | Amplicon (bp) |
|---|---|---|---|---|
| Sestrin 1 | NM_001199933 | CGACCAGGACGAGGAACTT | CCAATGTAGTGACGATAATGTAGG | 273 |
| Sestrin 2 | NM_031459 | CAAGCTCGGAATTAATGTGCC | CTCACACCATTAAGCATGGAG | 323 |
| APE/Ref-1 | NM_001641 | GCAGATACGGGGTTGCTCTT | TTTTACCGCGTTGCCCTACT | 136 |
| p53 | NM_000546.5 | GCGTGTGGAGTATTTGGATGAC | AGTGTGATGATGGTGAGGATGG | 168 |
| SOX2 | NM_003106.3 | ATCAGGAGTTGTCAAGGCAGAG | CGCCGCCGATGATTGTTATT | 172 |
| Nanog | NM_024865.2 | AATACCTCAGCCTCCAGCAGATG | TGCGTCACACCATTGCTATTCTTC | 148 |
| OCT4A | NM_002701.4 | CCTTCGCAAGCCCTCATTTCAC | GGAAGCTTAGCCAGGTCCGA | 169 |
| ITGA2 | NM_002203.3. | TTAGCGCTCAGTCAAGGCAT | CGGTTCTCAGGAAAGCCACT | 179 |
| ITGA6 | NM_001079818.1 | TCA TGG ATC TGC AAA TGG AA | AGG GAA CCA ACA GCA ACA TC | 135 |
| ITGB1 | NM_002211.3 | GCGCGGAAAAGATGAATTTACAAC | ATCTGGAGGGCAACCCTTCT | 245 |
| ICAM1 | NM_000201.2 | TGTGACCAGCCCAAGTTGTT | TGGAGTCCAGTACACGGTGA | 186 |
| PECAM1 | NM_000442.4 | CCAAGCCCGAACTGGAATCT | CACTGTCCGACTTTGAGGCT | 168 |
| OPN | NM_001040058.1 | CTCAGGCCAGTTGCAGCC | CAAAAGCAAATCACTGCAATTCTC | 81 |
| Collagen XV | NM_001855.4 | GGACTGTTGTCCACCTACCG | CTGGGGCCAAGAAGGATCTG | 228 |
| Tie1 | NM_005424.4 | TCTCATGTGGGCGCGG | AGCGGTGTCACCTTTGTTCA | 378 |
| Tie2 | NM_000459.3 | TGCGAGATGGATAGGGCTTG | GCACCTTCCACAGTTCCAGA | 366 |
| TGFBR1 | NM_004612.2 | CCTCGAGATAGGCCGTTTGT | CCAGGTGATGACTTTACAGTAGTTG | 125 |
| ALCAM | NM_001627.3 | AGAACACGATGAGGCAGACG | TGTTTTGATGCAGTCTTTGACTTCT | 162 |
| CD63 | NM_001780.5 | GCCCTTGGAATTGCTTTTGTCG | CATCACCTCGTAGCCACTTCTG | 87 |
| Ang-1 | NM_001146.3 | GCTGACAGATGTTGAGACCCA | TTCCTCCCTTTAGTAAAACACCTTC | 395 |
| Ang-2 | NM_001147.2 | AACTGATGTGGAAGCCCAAGT | GGGTCCTTAGCTGAGTTTGATGT | 387 |
| VEGFA | NM_001025366.2 | CGAGAAGTGCTAGCTCGGG | CTGGGACCACTTGGCATGG | 377 |
| CD34 | M81104 | CATCACTGGCTATTTCCTGATG | AGCCGAATGTGTAAAGGACAG | 440 |
| NG2 | NM_001897 | GCTTTGACCCTGACTATGTTGGC | TCCAGAGTAGAGCTGCAGCA | 195 |
| αSMA | NM_001613 | TGGCTATTCCTTCGTTACTA | CGATCCAGACAGAGTATTTGC | 437 |
| PDGFR-β | NM_002609 | CAGTAAGGAGGACTTCCTGGAG | CCTGAGAGATCTGTGGTTCCAG | 178 |
| vWF | NM_000552 | ATGATTCCTGCCAGATTTGC | CTCACCGGACAGCTTGTAGT | 396 |
| CD45 | Y00638 / NM_080921 | CATGTACTGCTCCTGATAAGAC | GCCTACACTTGACATGCATAC | 660 |
| ID1 | NM_002165.3 | AAACGTGCTGCTCTACGACA | GAACGCATGCCGCCTCG | 254 |
| ID2 | NM_002166.4 | CAGCATCCCCCAGAACAAGA | TTCAGAAGCCTGCAAGGACAG | 205 |
| PAI1 | NM_000602.4 | CCTCTGAGAACTTCAGGATGCAG | CCTGCTGAAACACCCTCACC | 153 |
| MMP1 | NM_002421.3 | AGACAAAGGCCAGTATGCAC | ACTGGGCCACTATTTCTCCG | 193 |
| MMP3 | NM_002422.3 | TACAAGGAGGCAGGCAAGACA | CACAATCCTGTATGTAAGGTGGGTT | 421 |
| MMP10 | NM_002425.2 | ACAAAGAAGGTAAGGGCAGTGA | AGGAGCTGAAGTGACCAACG | 328 |
| MMP13 | NM_002427.3 | CCCCAGGCATCACCATTCAA | CAGGTAGCGCTCTGCAAACT | 150 |
| GAPDH | NM_002046.4 | GCACCGTCAAGGCTGAGAAC | TGGTGAAGACGCCAGTGGA | 138 |

# REFERENCES

1.  Pittenger MF, Mackay AM, Beck SC, et al. Multilineage potential of adult human mesenchymal stem cells. Science. 1999;284:143-147.
2.  Mendicino M, Bailey AM, Wonnacott K, et al. MSC-Based Product Characterization for Clinical Trials: An FDA Perspective. Cell Stem Cell.14:141-145.
3.  LeBlanc K, Frassoni F, Ball L, et al. Mesenchymal stem cells for treatment of steroid-resistant, severe, acute graft-versus-host disease: a phase II study. Lancet. 2008;371:1579-1586.
4.  Ranganath SH, Levy O, Inamdar MS, et al. Harnessing the mesenchymal stem cell secretome for the treatment of cardiovascular disease. Cell Stem Cell.10:244-258.
5.  Madeira A, da Silva CL, dos Santos F, et al. Human mesenchymal stem cell expression program upon extended ex-vivo cultivation, as revealed by 2-DE-based quantitative proteomics. PLoS One.7:e43523.
6.  Heo JY, Jing K, Song KS, et al. Downregulation of APE1/Ref-1 is involved in the senescence of mesenchymal stem cells. Stem Cells. 2009;27:1455-1462.
7.  Izadpanah R, Kaushal D, Kriedt C, et al. Long-term in vitro expansion alters the biology of adult mesenchymal stem cells. Cancer Res. 2008;68:4229-4238.
8.  Zaim M, Karaman S, Cetin G, et al. Donor age and long-term culture affect differentiation and proliferation of human bone marrow mesenchymal stem cells. Ann Hematol.91:1175-1186.
9.  Wagner W, Horn P, Castoldi M, et al. Replicative senescence of mesenchymal stem cells: a continuous and organized process. PLoS One. 2008;3:e2213.
10. Stolzing A, Jones E, McGonagle D, et al. Age-related changes in human bone marrow-derived mesenchymal stem cells: consequences for cell therapies. Mech Ageing Dev. 2008;129:163-173.
11. Wagner W, Bork S, Horn P, et al. Aging and replicative senescence have related effects on human stem and progenitor cells. PLoS One. 2009;4:e5846.
12. Giordano A, Galderisi U, Marino IR. From the laboratory bench to the patient's bedside: an update on clinical trials with mesenchymal stem cells. J Cell Physiol. 2007;211:27-35.
13. Klopp AH, Gupta A, Spaeth E, et al. Concise review: Dissecting a discrepancy in the literature: do mesenchymal stem cells support or suppress tumor growth? Stem Cells.29:11-19.
14. Bergfeld SA, DeClerck YA. Bone marrow-derived mesenchymal stem cells and the tumor microenvironment. Cancer Metastasis Rev.29:249-261.
15. Bernardo ME, Zaffaroni N, Novara F, et al. Human bone marrow derived mesenchymal stem cells do not undergo transformation after long-term in vitro culture and do not exhibit telomere maintenance mechanisms. Cancer Res. 2007;67:9142-9149.
16. Torsvik A, Rosland GV, Svendsen A, et al. Spontaneous malignant transformation of human mesenchymal stem cells reflects cross-contamination: putting the research field on track - letter. Cancer Res.70:6393-6396.
17. Choumerianou DM, Dimitriou H, Perdikogianni C, et al. Study of oncogenic transformation in ex vivo expanded mesenchymal cells, from paediatric bone marrow. Cell Prolif. 2008;41:909-922.

18. Rodriguez R, Rubio R, Menendez P. Modeling sarcomagenesis using multipotent mesenchymal stem cells. Cell Res.

19. Li N, Yang R, Zhang W, et al. Genetically transforming human mesenchymal stem cells to sarcomas: changes in cellular phenotype and multilineage differentiation potential. Cancer. 2009;115:4795-4806.

20. Serakinci N, Guldberg P, Burns JS, et al. Adult human mesenchymal stem cell as a target for neoplastic transformation. Oncogene. 2004;23:5095-5098.

21. Funes JM, Quintero M, Henderson S, et al. Transformation of human mesenchymal stem cells increases their dependency on oxidative phosphorylation for energy production. Proc Natl Acad Sci U S A. 2007;104:6223-6228.

22. Lutolf MP, Gilbert PM, Blau HM. Designing materials to direct stem-cell fate. Nature. 2009;462:433-441.

23. Discher DE, Mooney DJ, Zandstra PW. Growth factors, matrices, and forces combine and control stem cells. Science. 2009;324:1673-1677.

24. Engler AJ, Sen S, Sweeney HL, et al. Matrix elasticity directs stem cell lineage specification. Cell. 2006;126:677-689.

25. Trappmann B, Gautrot JE, Connelly JT, et al. Extracellular-matrix tethering regulates stem-cell fate. Nat Mater.11:642-649.

26. Wang Y, Lee WC, Manga KK, et al. Fluorinated Graphene for Promoting Neuro-Induction of Stem Cells. Advanced Materials. 2012;24:4285-+.

27. Curran JM, Chen R, Hunt JA. Controlling the phenotype and function of mesenchymal stem cells in vitro by adhesion to silane-modified clean glass surfaces. Biomaterials. 2005;26:7057-7067.

28. Crowder SW, Liang Y, Rath R, et al. Poly(epsilon-caprolactone)-carbon nanotube composite scaffolds for enhanced cardiac differentiation of human mesenchymal stem cells. Nanomedicine (Lond).8:1763-1776.

29. Serena E, Figallo E, Tandon N, et al. Electrical stimulation of human embryonic stem cells: cardiac differentiation and the generation of reactive oxygen species. Exp Cell Res. 2009;315:3611-3619.

30. Tian B, Liu J, Dvir T, et al. Macroporous nanowire nanoelectronic scaffolds for synthetic tissues. Nat Mater.11:986-994.

31. Chu C, Schmidt JJ, Carnes K, et al. Three-dimensional synthetic niche components to control germ cell proliferation. Tissue Eng Part A. 2009;15:255-262.

32. Benoit DS, Schwartz MP, Durney AR, et al. Small functional groups for controlled differentiation of hydrogel-encapsulated human mesenchymal stem cells. Nat Mater. 2008;7:816-823.

33. Kim DH, Provenzano PP, Smith CL, et al. Matrix nanotopography as a regulator of cell function. J Cell Biol.197:351-360.

34. Wang X, Boire TC, Bronikowski C, et al. Decoupling polymer properties to elucidate mechanisms governing cell behavior. Tissue Eng Part B Rev.18:396-404.

35. Levy-Mishali M, Zoldan J, Levenberg S. Effect of scaffold stiffness on myoblast differentiation. Tissue Eng Part A. 2009;15:935-944.

36. Nam J, Johnson J, Lannutti JJ, et al. Modulation of embryonic mesenchymal progenitor cell differentiation via control over pure mechanical modulus in electrospun nanofibers. Acta Biomater. 2011;7:1516-1524.

37. Gupta MK, Walthall JM, Venkataraman R, et al. Combinatorial polymer electrospun matrices promote physiologically-relevant cardiomyogenic stem cell differentiation. PLoS One. 2011;6:e28935.

38. He W, Ma Z, Teo WE, et al. Tubular nanofiber scaffolds for tissue engineered small-diameter vascular grafts. J Biomed Mater Res A. 2009;90:205-216.

39. Zhang K, Wang H, Huang C, et al. Fabrication of silk fibroin blended P(LLA-CL) nanofibrous scaffolds for tissue engineering. J Biomed Mater Res A. 2010;93:984-993.

40. Engelhardt EM, Micol LA, Houis S, et al. A collagen-poly(lactic acid-co-varepsilon-caprolactone) hybrid scaffold for bladder tissue regeneration. Biomaterials. 2011;32:3969-3976.

41. Liu JJ, Wang CY, Wang JG, et al. Peripheral nerve regeneration using composite poly(lactic acid-caprolactone)/nerve growth factor conduits prepared by coaxial electrospinning. J Biomed Mater Res A. 2011;96:13-20.

42. Brocchini S, James K, Tangpasuthadol V, et al. Structure-property correlations in a combinatorial library of degradable biomaterials. J Biomed Mater Res. 1998;42:66-75.

43. Brey DM, Erickson I, Burdick JA. Influence of macromer molecular weight and chemistry on poly($\beta$-amino ester) network properties and initial cell interactions. Journal of Biomedical Materials Research Part A. 2008;85A:731-741.

44. Brey DM, Ifkovits JL, Mozia RI, et al. Controlling poly($\beta$-amino ester) network properties through macromer branching. Acta Biomater. 2008;4:207-217.

45. Metter RB, Ifkovits JL, Hou K, et al. Biodegradable fibrous scaffolds with diverse properties by electrospinning candidates from a combinatorial macromer library. Acta Biomater. 2010;6:1219-1226.

46. JORDAN J. GREEN RL, AND DANIEL G. ANDERSON. A Combinatorial Polymer Library Approach Yields Insight into Nonviral Gene Delivery. Accounts of Chemical Research. 2008;41:749-759.

47. Eltoukhy AA, Siegwart DJ, Alabi CA, et al. Effect of molecular weight of amine end-modified poly($\beta$-amino ester)s on gene delivery efficiency and toxicity. Biomaterials. 2012;33:3594-3603.

48. Cai L, Wang S. Poly($\varepsilon$-caprolactone) acrylates synthesized using a facile method for fabricating networks to achieve controllable physicochemical properties and tunable cell responses. Polymer. 2010;51:164-177.

49. Joy A, Cohen DM, Luk A, et al. Control of Surface Chemistry, Substrate Stiffness, and Cell Function in a Novel Terpolymer Methacrylate Library. Langmuir. 2011;27:1891-1899.

50. Peters A, Brey DM, Burdick JA. High-Throughput and Combinatorial Technologies for Tissue Engineering Applications. Tissue Eng Part B-Re. 2009;15:225-239.

51. Webster D, Meier M. Polymer Libraries: Preparation and Applications Polymer Libraries. In: Meier MAR, Webster DC, eds: Springer Berlin / Heidelberg; 2009:1-15.

52. Sung HJ, Su J, Berglund JD, et al. The use of temperature-composition combinatorial libraries to study the effects of biodegradable polymer blend surfaces on vascular cells. Biomaterials. 2005;26:4557-4567.

53. Anderson DG, Putnam D, Lavik EB, et al. Biomaterial microarrays: rapid, microscale screening of polymer–cell interaction. Biomaterials. 2005;26:4892-4897.

54.  Dolatshahi-Pirouz A, Nikkhah M, Kolind K, et al. Micro- and Nanoengineering Approaches to Control Stem Cell-Biomaterial Interactions. Journal of Functional Biomaterials. 2011;2:88-106.

55.  Spokoyny AM, Kim D, Sumrein A, et al. Infinite coordination polymer nano- and microparticle structures. Chem Soc Rev. 2009;38:1218-1227.

56.  Simon Jr CG, Eidelman N, Kennedy SB, et al. Combinatorial screening of cell proliferation on poly(l-lactic acid)/poly(d,l-lactic acid) blends. Biomaterials. 2005;26:6906-6915.

57.  Chatterjee K, Sun L, Chow LC, et al. Combinatorial screening of osteoblast response to 3D calcium phosphate/poly(ε-caprolactone) scaffolds using gradients and arrays. Biomaterials. 2011;32:1361-1369.

58.  Crowder SW, Horton LW, Lee SH, et al. Passage-dependent cancerous transformation of human mesenchymal stem cells under carcinogenic hypoxia. FASEB J.27:2788-2798.

59.  Das R, Jahr H, van Osch GJ, et al. The role of hypoxia in bone marrow-derived mesenchymal stem cells: considerations for regenerative medicine approaches. Tissue Eng Part B Rev.16:159-168.

60.  Hockel M, Vaupel P. Tumor hypoxia: definitions and current clinical, biologic, and molecular aspects. J Natl Cancer Inst. 2001;93:266-276.

61.  Grayson WL, Zhao F, Bunnell B, et al. Hypoxia enhances proliferation and tissue formation of human mesenchymal stem cells. Biochem Biophys Res Commun. 2007;358:948-953.

62.  Chacko SM, Ahmed S, Selvendiran K, et al. Hypoxic preconditioning induces the expression of prosurvival and proangiogenic markers in mesenchymal stem cells. Am J Physiol Cell Physiol.299:C1562-1570.

63.  Tsai CC, Chen YJ, Yew TL, et al. Hypoxia inhibits senescence and maintains mesenchymal stem cell properties through down-regulation of E2A-p21 by HIF-TWIST. Blood.117:459-469.

64.  Basciano L, Nemos C, Foliguet B, et al. Long term culture of mesenchymal stem cells in hypoxia promotes a genetic program maintaining their undifferentiated and multipotent status. BMC Cell Biol.12:12.

65.  Estrada JC, Albo C, Benguria A, et al. Culture of human mesenchymal stem cells at low oxygen tension improves growth and genetic stability by activating glycolysis. Cell Death Differ.

66.  Semenza GL. Targeting HIF-1 for cancer therapy. Nat Rev Cancer. 2003;3:721-732.

67.  Vogelstein B, Lane D, Levine AJ. Surfing the p53 network. Nature. 2000;408:307-310.

68.  Koumenis C, Alarcon R, Hammond E, et al. Regulation of p53 by hypoxia: dissociation of transcriptional repression and apoptosis from p53-dependent transactivation. Mol Cell Biol. 2001;21:1297-1310.

69.  Achison M, Hupp TR. Hypoxia attenuates the p53 response to cellular damage. Oncogene. 2003;22:3431-3440.

70.  Salnikow K, An WG, Melillo G, et al. Nickel-induced transformation shifts the balance between HIF-1 and p53 transcription factors. Carcinogenesis. 1999;20:1819-1823.

71.  Rani AS, Qu DQ, Sidhu MK, et al. Transformation of immortal, non-tumorigenic osteoblast-like human osteosarcoma cells to the tumorigenic phenotype by nickel sulfate. Carcinogenesis. 1993;14:947-953.

72. Oller AR, Costa M, Oberdorster G. Carcinogenicity assessment of selected nickel compounds. Toxicol Appl Pharmacol. 1997;143:152-166.
73. Garg S, Serruys P. Biodegradable stents and non-biodegradable stents. Minerva Cardioangiol. 2009;57:537-565.
74. Evan GI, Vousden KH. Proliferation, cell cycle and apoptosis in cancer. Nature. 2001;411:342-348.
75. Cameron KS, Buchner V, Tchounwou PB. Exploring the molecular mechanisms of nickel-induced genotoxicity and carcinogenicity: a literature review. Rev Environ Health.26:81-92.
76. Sung HJ, Yee A, Eskin SG, et al. Cyclic strain and motion control produce opposite oxidative responses in two human endothelial cell types. Am J Physiol Cell Physiol. 2007;293:C87-94.
77. Giambernardi TA, Grant GM, Taylor GP, et al. Overview of matrix metalloproteinase expression in cultured human cells. Matrix Biol. 1998;16:483-496.
78. Listenberger LL, Brown DA. Fluorescent detection of lipid droplets and associated proteins. Curr Protoc Cell Biol. 2007;Chapter 24:Unit 24 22.
79. Galis ZS, Muszynski M, Sukhova GK, et al. Cytokine-stimulated human vascular smooth muscle cells synthesize a complement of enzymes required for extracellular matrix digestion. Circ Res. 1994;75:181-189.
80. Valko M, Leibfritz D, Moncol J, et al. Free radicals and antioxidants in normal physiological functions and human disease. Int J Biochem Cell Biol. 2007;39:44-84.
81. Kretlow JD, Jin YQ, Liu W, et al. Donor age and cell passage affects differentiation potential of murine bone marrow-derived stem cells. BMC Cell Biol. 2008;9:60.
82. Crowder SW, Gupta MK, Hofmeister LH, et al. Modular polymer design to regulate phenotype and oxidative response of human coronary artery cells for potential stent coating applications. Acta Biomaterialia. 2012;8:559-569.
83. Zhang LL, Xiong CD, Deng XM. Biodegradable polyester blends for biomedical application. J Appl Pol Sci. 1995;56:103-122.
84. Tang ZG, Black RA, Curran JM, et al. Surface properties and biocompatibility of solvent-cast poly[-caprolactone] films. Biomaterials. 2004;25:4741-4748.
85. Bergstrom K, Holmberg K, Safranj A, et al. Reduction of fibrinogen adsorption on PEG-coated polystyrene surfaces. J Biomed Mater Res. 1992;26:779-790.
86. Deschamps AA, van Apeldoorn AA, Hayen H, et al. In vivo and in vitro degradation of poly(ether ester) block copolymers based on poly(ethylene glycol) and poly(butylene terephthalate). Biomaterials. 2004;25:247-258.
87. Sun G, Zhang XZ, Chu CC. Effect of the molecular weight of polyethylene glycol (PEG) on the properties of chitosan-PEG-poly(N-isopropylacrylamide) hydrogels. J Mater Sci Mater Med. 2008;19:2865-2872.
88. Sung HJ, Chandra P, Treiser MD, et al. Synthetic polymeric substrates as potent pro-oxidant versus anti-oxidant regulators of cytoskeletal remodeling and cell apoptosis. J Cell Physiol. 2009;218:549-557.
89. Sung H-J, Luk A, Murthy S, et al. Poly(ethylene glycol) as a sensitive regulator of cell survival fate on polymeric biomaterials: the interplay of cell adhesion and pro-oxidant signaling mechanisms. Soft Matter. 2010;6:5196-5205.
90. Gimenez S, Ponsart S, Coudane J, et al. Synthesis, properties and in vitro degradation of carboxyl-bearing PCL. Journal of Bioactive and Compatible Polymers. 2001;16:32-46.

91. Crowder SW, Gupta MK, Hofmeister LH, et al. Modular polymer design to regulate phenotype and oxidative response of human coronary artery cells for potential stent coating applications. Acta Biomater. 2012;8:559-569.

92. Dong CM, Qiu KY, Cu ZW, et al. Synthesis of star-shaped poly(epsilon-caprolactone)-b-poly(DL-lactic acid-alt-glycolic acid) with multifunctional initiator and stannous octoate catalyst. Macromolecules. 2001;34:4691-4696.

93. Sosnik A, Cohn D. Poly(ethylene glycol)-poly(epsilon-caprolactone) block oligomers as injectable materials. Polymer. 2003;44:7033-7042.

94. Weber N, Wendel HP, Kohn J. Formation of viscoelastic protein layers on polymeric surfaces relevant to platelet adhesion. J Biomed Mater Res A. 2005;72:420-427.

95. Deskins DL, Bastakoty D, Saraswati S, et al. Human mesenchymal stromal cells: identifying assays to predict potency for therapeutic selection. Stem Cells Transl Med.2:151-158.

96. Sung HJ, Luk A, Murthy NS, et al. Poly(ethylene glycol) as a sensitive regulator of cell survival fate on polymeric biomaterials: the interplay of cell adhesion and pro-oxidant signaling mechanisms. Soft Matter. 2010;6:5196-5205.

97. McMurray RJ, Gadegaard N, Tsimbouri PM, et al. Nanoscale surfaces for the long-term maintenance of mesenchymal stem cell phenotype and multipotency. Nat Mater.10:637-644.

98. Wang K, Zhang T, Dong Q, et al. Redox homeostasis: the linchpin in stem cell self-renewal and differentiation. Cell Death Dis.4:e537.

99. Crisan M, Yap S, Casteilla L, et al. A perivascular origin for mesenchymal stem cells in multiple human organs. Cell Stem Cell. 2008;3:301-313.

100. Caplan AI. All MSCs are pericytes? Cell Stem Cell. 2008;3:229-230.

101. Armulik A, Genove G, Betsholtz C. Pericytes: developmental, physiological, and pathological perspectives, problems, and promises. Dev Cell.21:193-215.

102. Armulik A, Abramsson A, Betsholtz C. Endothelial/pericyte interactions. Circ Res. 2005;97:512-523.

103. Ribatti D, Nico B, Crivellato E. The role of pericytes in angiogenesis. Int J Dev Biol.55:261-268.

104. Stratman AN, Davis GE. Endothelial cell-pericyte interactions stimulate basement membrane matrix assembly: influence on vascular tube remodeling, maturation, and stabilization. Microsc Microanal.18:68-80.

105. Stratman AN, Malotte KM, Mahan RD, et al. Pericyte recruitment during vasculogenic tube assembly stimulates endothelial basement membrane matrix formation. Blood. 2009;114:5091-5101.

106. Corselli M, Chin CJ, Parekh C, et al. Perivascular support of human hematopoietic stem/progenitor cells. Blood.121:2891-2901.

107. Bailey AS, Willenbring H, Jiang S, et al. Myeloid lineage progenitors give rise to vascular endothelium. Proc Natl Acad Sci U S A. 2006;103:13156-13161.

108. Kim SJ, Kim JS, Papadopoulos J, et al. Circulating monocytes expressing CD31: implications for acute and chronic angiogenesis. Am J Pathol. 2009;174:1972-1980.

109. Davis S, Aldrich TH, Jones PF, et al. Isolation of angiopoietin-1, a ligand for the TIE2 receptor, by secretion-trap expression cloning. Cell. 1996;87:1161-1169.

110. Abdel-Malak NA, Srikant CB, Kristof AS, et al. Angiopoietin-1 promotes endothelial cell proliferation and migration through AP-1-dependent autocrine production of interleukin-8. Blood. 2008;111:4145-4154.

111. Shyu KG, Manor O, Magner M, et al. Direct intramuscular injection of plasmid DNA encoding angiopoietin-1 but not angiopoietin-2 augments revascularization in the rabbit ischemic hindlimb. Circulation. 1998;98:2081-2087.

112. Abdel-Malak NA, Harfouche R, Hussain SN. Transcriptome of angiopoietin 1-activated human umbilical vein endothelial cells. Endothelium. 2007;14:285-302.

113. Kobayashi H, DeBusk LM, Babichev YO, et al. Hepatocyte growth factor mediates angiopoietin-induced smooth muscle cell recruitment. Blood. 2006;108:1260-1266.

114. Iivanainen E, Nelimarkka L, Elenius V, et al. Angiopoietin-regulated recruitment of vascular smooth muscle cells by endothelial-derived heparin binding EGF-like growth factor. FASEB J. 2003;17:1609-1621.

115. Maisonpierre PC, Suri C, Jones PF, et al. Angiopoietin-2, a natural antagonist for Tie2 that disrupts in vivo angiogenesis. Science. 1997;277:55-60.

116. Gale NW, Thurston G, Hackett SF, et al. Angiopoietin-2 is required for postnatal angiogenesis and lymphatic patterning, and only the latter role is rescued by Angiopoietin-1. Dev Cell. 2002;3:411-423.

117. Fiedler U, Scharpfenecker M, Koidl S, et al. The Tie-2 ligand angiopoietin-2 is stored in and rapidly released upon stimulation from endothelial cell Weibel-Palade bodies. Blood. 2004;103:4150-4156.

118. Saharinen P, Alitalo K. The yin, the yang, and the angiopoietin-1. J Clin Invest.121:2157-2159.

119. Mendes LF, Pirraco RP, Szymczyk W, et al. Perivascular-like cells contribute to the stability of the vascular network of osteogenic tissue formed from cell sheet-based constructs. PLoS One.7:e41051.

120. He W, Nieponice A, Soletti L, et al. Pericyte-based human tissue engineered vascular grafts. Biomaterials.31:8235-8244.

121. Riha GM, Lin PH, Lumsden AB, et al. Review: application of stem cells for vascular tissue engineering. Tissue Eng. 2005;11:1535-1552.

122. Doorn J, Fernandes HA, Le BQ, et al. A small molecule approach to engineering vascularized tissue. Biomaterials.34:3053-3063.

123. O'Cearbhaill ED, Murphy M, Barry F, et al. Behavior of human mesenchymal stem cells in fibrin-based vascular tissue engineering constructs. Ann Biomed Eng.38:649-657.

124. Dong JD, Gu YQ, Li CM, et al. Response of mesenchymal stem cells to shear stress in tissue-engineered vascular grafts. Acta Pharmacol Sin. 2009;30:530-536.

125. Krawiec JT, Vorp DA. Adult stem cell-based tissue engineered blood vessels: a review. Biomaterials.33:3388-3400.

126. Ball SG, Shuttleworth CA, Kielty CM. Mesenchymal stem cells and neovascularization: role of platelet-derived growth factor receptors. J Cell Mol Med. 2007;11:1012-1030.

127. Au P, Tam J, Fukumura D, et al. Bone marrow-derived mesenchymal stem cells facilitate engineering of long-lasting functional vasculature. Blood. 2008;111:4551-4558.

128. Zouani OF, Lei Y, Durrieu MC. Pericytes, stem-cell-like cells, but not mesenchymal stem cells are recruited to support microvascular tube stabilization. Small.9:3070-3075.

129.  Blocki A, Wang Y, Koch M, et al. Not all MSCs can act as pericytes: functional in vitro assays to distinguish pericytes from other mesenchymal stem cells in angiogenesis. Stem Cells Dev.22:2347-2355.

130.  Salasznyk RM, Williams WA, Boskey A, et al. Adhesion to Vitronectin and Collagen I Promotes Osteogenic Differentiation of Human Mesenchymal Stem Cells. J Biomed Biotechnol. 2004;2004:24-34.

131.  Boland GM, Perkins G, Hall DJ, et al. Wnt 3a promotes proliferation and suppresses osteogenic differentiation of adult human mesenchymal stem cells. J Cell Biochem. 2004;93:1210-1230.

132.  Luu HH, Song WX, Luo X, et al. Distinct roles of bone morphogenetic proteins in osteogenic differentiation of mesenchymal stem cells. J Orthop Res. 2007;25:665-677.

133.  Jaiswal RK, Jaiswal N, Bruder SP, et al. Adult human mesenchymal stem cell differentiation to the osteogenic or adipogenic lineage is regulated by mitogen-activated protein kinase. J Biol Chem. 2000;275:9645-9652.

134.  Dalby MJ, Gadegaard N, Tare R, et al. The control of human mesenchymal cell differentiation using nanoscale symmetry and disorder. Nat Mater. 2007;6:997-1003.

135.  Solchaga LA, Penick KJ, Welter JF. Chondrogenic differentiation of bone marrow-derived mesenchymal stem cells: tips and tricks. Methods Mol Biol.698:253-278.

136.  Barry F, Boynton RE, Liu B, et al. Chondrogenic differentiation of mesenchymal stem cells from bone marrow: differentiation-dependent gene expression of matrix components. Exp Cell Res. 2001;268:189-200.

137.  Bosnakovski D, Mizuno M, Kim G, et al. Chondrogenic differentiation of bovine bone marrow mesenchymal stem cells (MSCs) in different hydrogels: influence of collagen type II extracellular matrix on MSC chondrogenesis. Biotechnol Bioeng. 2006;93:1152-1163.

138.  Cho JH, Kim SH, Park KD, et al. Chondrogenic differentiation of human mesenchymal stem cells using a thermosensitive poly(N-isopropylacrylamide) and water-soluble chitosan copolymer. Biomaterials. 2004;25:5743-5751.

139.  Scott MA, Nguyen VT, Levi B, et al. Current methods of adipogenic differentiation of mesenchymal stem cells. Stem Cells Dev.20:1793-1804.

140.  Kolf CM, Cho E, Tuan RS. Mesenchymal stromal cells. Biology of adult mesenchymal stem cells: regulation of niche, self-renewal and differentiation. Arthritis Res Ther. 2007;9:204.

141.  Mirmalek-Sani SH, Tare RS, Morgan SM, et al. Characterization and multipotentiality of human fetal femur-derived cells: implications for skeletal tissue regeneration. Stem Cells. 2006;24:1042-1053.

142.  Gronthos S, Graves SE, Ohta S, et al. The STRO-1+ fraction of adult human bone marrow contains the osteogenic precursors. Blood. 1994;84:4164-4173.

143.  Simmons PJ, Torok-Storb B. Identification of stromal cell precursors in human bone marrow by a novel monoclonal antibody, STRO-1. Blood. 1991;78:55-62.

144.  Gronthos S, Zannettino AC, Hay SJ, et al. Molecular and cellular characterisation of highly purified stromal stem cells derived from human bone marrow. J Cell Sci. 2003;116:1827-1835.

145.  Niehage C, Steenblock C, Pursche T, et al. The cell surface proteome of human mesenchymal stromal cells. PLoS One.6:e20399.

146. Bruder SP, Ricalton NS, Boynton RE, et al. Mesenchymal stem cell surface antigen SB-10 corresponds to activated leukocyte cell adhesion molecule and is involved in osteogenic differentiation. J Bone Miner Res. 1998;13:655-663.

147. Nichols J, Zevnik B, Anastassiadis K, et al. Formation of pluripotent stem cells in the mammalian embryo depends on the POU transcription factor Oct4. Cell. 1998;95:379-391.

148. Yu KR, Yang SR, Jung JW, et al. CD49f enhances multipotency and maintains stemness through the direct regulation of OCT4 and SOX2. Stem Cells.30:876-887.

149. Tsai CC, Su PF, Huang YF, et al. Oct4 and Nanog directly regulate Dnmt1 to maintain self-renewal and undifferentiated state in mesenchymal stem cells. Mol Cell.47:169-182.

150. Zhang D, Kilian KA. The effect of mesenchymal stem cell shape on the maintenance of multipotency. Biomaterials.34:3962-3969.

151. Huang GS, Dai LG, Yen BL, et al. Spheroid formation of mesenchymal stem cells on chitosan and chitosan-hyaluronan membranes. Biomaterials.32:6929-6945.

152. Rustad KC, Wong VW, Sorkin M, et al. Enhancement of mesenchymal stem cell angiogenic capacity and stemness by a biomimetic hydrogel scaffold. Biomaterials.33:80-90.

153. Candiano G, Bruschi M, Musante L, et al. Blue silver: a very sensitive colloidal Coomassie G-250 staining for proteome analysis. Electrophoresis. 2004;25:1327-1333.

154. Yates JR, 3rd, Eng JK, McCormack AL, et al. Method to correlate tandem mass spectra of modified peptides to amino acid sequences in the protein database. Anal Chem. 1995;67:1426-1436.

155. Poole KM, Tucker-Schwartz JM, Sit WW, et al. Quantitative optical imaging of vascular response in vivo in a model of peripheral arterial disease. Am J Physiol Heart Circ Physiol.305:H1168-1180.

156. Frangi AF, Niessen WJ, Vincken KL, et al. Multiscale vessel enhancement filtering. Medical Image Computing and Computer-Assisted Intervention - Miccai'98. 1998;1496:130-137.

157. Canny J. A Computational Approach to Edge-Detection. Ieee Transactions on Pattern Analysis and Machine Intelligence. 1986;8:679-698.

158. Woodfin A, Voisin MB, Nourshargh S. PECAM-1: a multi-functional molecule in inflammation and vascular biology. Arterioscler Thromb Vasc Biol. 2007;27:2514-2523.

159. San Antonio JD, Zoeller JJ, Habursky K, et al. A key role for the integrin alpha2beta1 in experimental and developmental angiogenesis. Am J Pathol. 2009;175:1338-1347.

160. Senger DR, Perruzzi CA, Streit M, et al. The alpha(1)beta(1) and alpha(2)beta(1) integrins provide critical support for vascular endothelial growth factor signaling, endothelial cell migration, and tumor angiogenesis. Am J Pathol. 2002;160:195-204.

161. Whyte JL, Ball SG, Shuttleworth CA, et al. Density of human bone marrow stromal cells regulates commitment to vascular lineages. Stem Cell Res.6:238-250.

162. Janeczek Portalska K, Leferink A, Groen N, et al. Endothelial differentiation of mesenchymal stromal cells. PLoS One.7:e46842.

163. Vodyanik MA, Yu J, Zhang X, et al. A mesoderm-derived precursor for mesenchymal stem and endothelial cells. Cell Stem Cell.7:718-729.

164. Gory-Faure S, Prandini MH, Pointu H, et al. Role of vascular endothelial-cadherin in vascular morphogenesis. Development. 1999;126:2093-2102.

165.  Zachman AL, Crowder SW, Ortiz O, et al. Pro-angiogenic and anti-inflammatory regulation by functional peptides loaded in polymeric implants for soft tissue regeneration. Tissue Eng Part A.19:437-447.

166.  Brindle NP, Saharinen P, Alitalo K. Signaling and functions of angiopoietin-1 in vascular protection. Circ Res. 2006;98:1014-1023.

167.  Davis GE, Camarillo CW. An alpha 2 beta 1 integrin-dependent pinocytic mechanism involving intracellular vacuole formation and coalescence regulates capillary lumen and tube formation in three-dimensional collagen matrix. Exp Cell Res. 1996;224:39-51.

168.  Pochampally RR, Smith JR, Ylostalo J, et al. Serum deprivation of human marrow stromal cells (hMSCs) selects for a subpopulation of early progenitor cells with enhanced expression of OCT-4 and other embryonic genes. Blood. 2004;103:1647-1652.

169.  Oskowitz A, McFerrin H, Gutschow M, et al. Serum-deprived human multipotent mesenchymal stromal cells (MSCs) are highly angiogenic. Stem Cell Res.6:215-225.

170.  Sanchez C, Oskowitz A, Pochampally RR. Epigenetic reprogramming of IGF1 and leptin genes by serum deprivation in multipotential mesenchymal stromal cells. Stem Cells. 2009;27:375-382.

171.  Demetriou M, Binkert C, Sukhu B, et al. Fetuin/alpha2-HS glycoprotein is a transforming growth factor-beta type II receptor mimic and cytokine antagonist. J Biol Chem. 1996;271:12755-12761.

172.  Szweras M, Liu D, Partridge EA, et al. alpha 2-HS glycoprotein/fetuin, a transforming growth factor-beta/bone morphogenetic protein antagonist, regulates postnatal bone growth and remodeling. J Biol Chem. 2002;277:19991-19997.

173.  Guo X, Wang XF. Signaling cross-talk between TGF-beta/BMP and other pathways. Cell Res. 2009;19:71-88.

174.  Kutz SM, Hordines J, McKeown-Longo PJ, et al. TGF-beta1-induced PAI-1 gene expression requires MEK activity and cell-to-substrate adhesion. J Cell Sci. 2001;114:3905-3914.

175.  Hollnagel A, Oehlmann V, Heymer J, et al. Id genes are direct targets of bone morphogenetic protein induction in embryonic stem cells. J Biol Chem. 1999;274:19838-19845.

176.  Chen C, Uludag H, Wang Z, et al. Noggin suppression decreases BMP-2-induced osteogenesis of human bone marrow-derived mesenchymal stem cells in vitro. J Cell Biochem.113:3672-3680.

177.  Roelen BA, Dijke P. Controlling mesenchymal stem cell differentiation by TGFBeta family members. J Orthop Sci. 2003;8:740-748.

178.  Walenda G, Abnaof K, Joussen S, et al. TGF-beta1 does not induce senescence of multipotent mesenchymal stromal cells and has similar effects in early and late passages. PLoS One.8:e77656.

179.  Diefenderfer DL, Osyczka AM, Reilly GC, et al. BMP responsiveness in human mesenchymal stem cells. Connect Tissue Res. 2003;44 Suppl 1:305-311.